Insights into the function and pharmacology of the TRPML3 cation channel

DISSERTATION

zur Erlangung des akademischen Grades des

Doktors der Naturwissenschaften

(Dr. rer. nat.)

eingereicht

im Fachbereich Biologie, Chemie, Pharmazie

der Freien Universität Berlin

vorgelegt von

SIMONE JÖRS

Berlin 2011

1. Gutachter: Prof. Dr. Constance Scharff
Freie Universität Berlin
Verhaltensbiologie, Institut für Biologie,
Takustrasse 6
14195 Berlin, Germany

2. Gutachter: Prof. Dr. Stefan Heller
Stanford University, Medical School
Department of Otolaryngology, Head & Neck Surgery
300 Pasteur Drive
Stanford, 94305, CA, USA

Tag der Disputation: 6.7.2011

Acknowledgement

First, I would like to thank Prof. Stefan Heller for giving me the opportunity to work in his research group. I am very grateful for his continuous support and advice, and especially the freedom he offered me for designing and conducting the project.

Furthermore, I would like to thank Prof. Constance Scharff for agreeing to be my first advisor and for offering me her support for my PhD project.

Special thanks also to Dr. Christian Grimm for excellent collaboration on the TRPML3 projects, for the moral and professional support throughout my PhD years as well the constructive discussions and comments on my PhD thesis.

Many thanks to Dr. Lars Becker for his enthusiastic support and collaboration on the *Trpml3* knockout project.

I thank Dr. Gerald Popelka (Department of Otolaryngology, Stanford University) for the assistance during the set-up and establishment of the ABR technique in the Heller laboratory and for expert advice on my ABR measurements.

Furthermore, I thank Dr. Hong Zeng (Stanford Transgenic Research facility) for the supervision and technical support throughout the process of generating the conditional *Trpml3* inactivation in mice.

I would like to thank Dr. Hansjörg Lehnherr for providing valuable comments on the manuscript and all members of Prof. Stefan Heller's research group, not only for their stimulating discussions about science, but also for making my time there very enjoyable.

The work presented in this thesis was funded by grants from the National Institutes of Health (DC004563, MH083077, and P30 DC010363).

Table of contents

List of Figures

List of Tables

Abbreviations

aa	amino acid
ABR	auditory brainstem response
asn	antisense
BAPTA	1,2-bis(2-aminophenoxy)ethane-N,N,N',N'-tetraacetic acid
BM	basal membrane
bp	base pairs
BSA	bovine serum albumin
°C	degree Celsius
$[Ca^{2+}]_i$	intracellular calcium concentration
CaM	Calmodulin binding domains
cc	coiled-coil domain
CFP	cyan fluorescent protein
cDNA	complementary deoxyribonucleic acid
C(N)-terminal	carboxy(amino)-terminal
Cre	causes recombination
Dfw	deaf-waddler
DMEM	Dulbecco's modified Eagle medium
DMSO	dimethyl sulfoxide
DNA	deoxyribonucleic acid
DNase	deoxyribonuclease
DTA	Diphtheria toxin A
dNTPs	deoxyribonucleotides
DPOAE	distortion product otoacoustic emission
DRG	dorsal root ganglia
DTA	Diphtheria toxin A
Dyn	dynamin
E	embryonic stage (in days post-coitus)
EC_{50}	median effective concentration
E.coli	*Escherichia coli*
EDTA	ethylenediaminetetraacetic acid
EGTA	ethylene glycol-bis(ß-aminoethylether)-N,N,N',N'-tetraacetic acid
EP	endocochlear potential
ER	estrogen receptor

ES	embryonic stem
EtOH	ethanol
exc	excision
$F_{340\ (380)}$	fura-2 fluorescence at 340 (380) nm excitation
FITC	fluorescein isothiocyanate
FRET	fluorescence resonance energy transfer
FRT	Flp recognition target
Fura-2-AM	fura-2-acetoxymethyl ester
GAPDH	glyceraldehyde-3-phosphate dehydrogenase
HA	hemagglutinin
HC	hair cell
HEK293	human embryonic kidney 293 cells
HEM	human epidermal melanocytes
HEPES	N-2-hydroxyethylpiperazine-N'-(2-ethanesulphonic acid)
HL	hearing level
ICM	inner cell mass
IHC	inner hair cell
IP_3R	Inositol-triphosphate receptor binding site
kb	kilo base
LA	left arm
loxP	locus of cross-over (*x*) in P1
LTS	lysosomal targeting site
MCS	multiple cloning site
MET	Mechanoelectrical transduction channel
MLIV	Mucolipidosis IV
MOPS	3-(N-morpholino)propanesulfonic acid
mRNA	messenger ribonucleic acid
neo^R	neomycin phosphotransferase-encoding gene
NT	non-transfected
OHC	outer hair cell
P	pore
P10	postnatal day 10
PBS	phosphate buffered saline
PGK	Phosphoglycerine kinase

PKA	protein kinase A
PKC	protein kinase C
PMCA	plasma membrane calcium ATPase
PMFS	Phenylmethanesulfonyl fluoride
RA	right arm
RNA	ribonucleic acid
RNase	ribonuclease
rpm	rounds per minute
RT-PCR	reverse transcription polymerase chain reaction
SC	supporting cell
SD	standard deviation
SEM	standard error of the mean
seq	sequencing
SF	scaffolds
shRNA	small hairpin RNA
sn	sense
SN	singleton
TM	transmembrane domain
Tris	Tris-(hydroxymethyl)aminomethane
TRITC	tetramethylrhodamine isothiocyanate
TRP	transient receptor potential
UTR	untranslated region
Va	varitint
YFP	yellow fluorescent protein

1. Introduction

1.1. TRP cation channels

The TRP (*transient receptor potential*) ion channels are permeable to cations, including sodium, potassium, calcium and magnesium. The mammalian TRP family comprises 28 cation channel genes, some of which are widely expressed in many tissues and cell types, whereas others are expressed in a more cell type specific fashion. TRP channels use a wide variety of regulatory themes and carry out functions as diverse as thermosensation, pheromone perception, taste, touch and pain sensation, mechanosensation or osmoregulation. As a relatively recently discovered group of ion channels, TRP channels have generated much interest in discovery and as targets for therapeutic strategies (for reviews, see Voets et al., 2005; Nilius et al., 2006; Patapoutian et al., 2009). In my thesis I am focusing on the third member of the TRPML (mucolipin) subfamily of TRP channels, TRPML3, which is one of the most recently discovered TRP channels (Di Palma et al., 2002).

The general topology of TRP channels includes cytoplasmatic amino and carboxyl termini of variable length and six transmembrane domains (TM1-TM6) with a pore-forming loop (P) between TM5 and TM6 (Fig. 1). A functional unit of TRP channel requires tetrameric assembly of either homomeric or heteromeric TRP polypeptides (for a review, see Schaefer, 2005). Heteromeric assembly may give rise to additional diversity in regulatory and biophysical properties. The TRP family can be divided in seven subfamilies that are further classified into two groups (for a review, see Ramsey et al., 2006, Venkatachalam and Montell, 2007; Owsianik et al., 2006). This classification is based on sequence and topological homology. The five group 1 subfamilies: TRPC (for canonical), TRPV (for vanilloid), TRPM (for melastatin), TRPA (for ankyrin), and TRPN (for NOMP or “no mechanoreceptor potential”) share substantial sequence identity in their TMs and several other common sequence elements and domains. TRPC, TRPM, TRPV, and TRPN channels contain a TRP box, a highly conserved structure located in the C-terminus close to TM6. In TRPC channels, the TRP box is fully conserved and characterized by the specific amino acid sequence, EWKFAR. In TRPV, TRPM, and TRPN channels the conservation of the TRP box is very low (for reviews, see Owsianik et al., 2006; Venkatachalam and Montell, 2007). With the exception of TRPM channels, the group 1 channels have the presence of multiple N-terminal ankyrin repeats in common, which have

been hypothesized to mediate specific protein-protein interactions (Mohler et al., 2002), linking members of the TRPC and TRPV family to the cytoskeleton, or allowing multimerization of channel complexes (Erler et al., 2004). TRPCs and TRPVs typically contain three or four ankyrin repeats, compared to 14 in TRPA1 and 29 in TRPN1. Some TRPM channels, on the other hand, have an enzymatic domain in the C-terminus. TRPM2 has an ADP-ribose pyrophosphatase domain and TRPM6 and TRPM7 have kinase domains (for reviews, see Pedersen et al., 2005; Venkatachalam and Montell, 2007). The group 2 subfamilies, TRPP (for polycystin) and TRPML (for mucolipin), have lower overall amino acid sequence similarity to group 1. Their most conspicuous feature is the long extracellular loop between TM1 and TM2. The TRPP family is very inhomogeneous and can be divided in TRPP1 and TRPP2 channels. Mutation in TRPP1 and TRPP2 cause autosomal dominant polycystic kidney disease (Sutters and Germino, 2003). TRPP1 proteins differ from other TRP channels in that these proteins contain 11 TMs and a very long extracellular domain (~3000 aa). TRPP2 proteins, on the other hand, have the TRP channel-typical 6 TM configuration and are believed to be the pore-forming subunit of TRPPs (Hanaoka et al., 2000). The TRPML subfamily will be discussed in more detail below. Additional domains and motifs have been identified and illustrated in Figure 1.

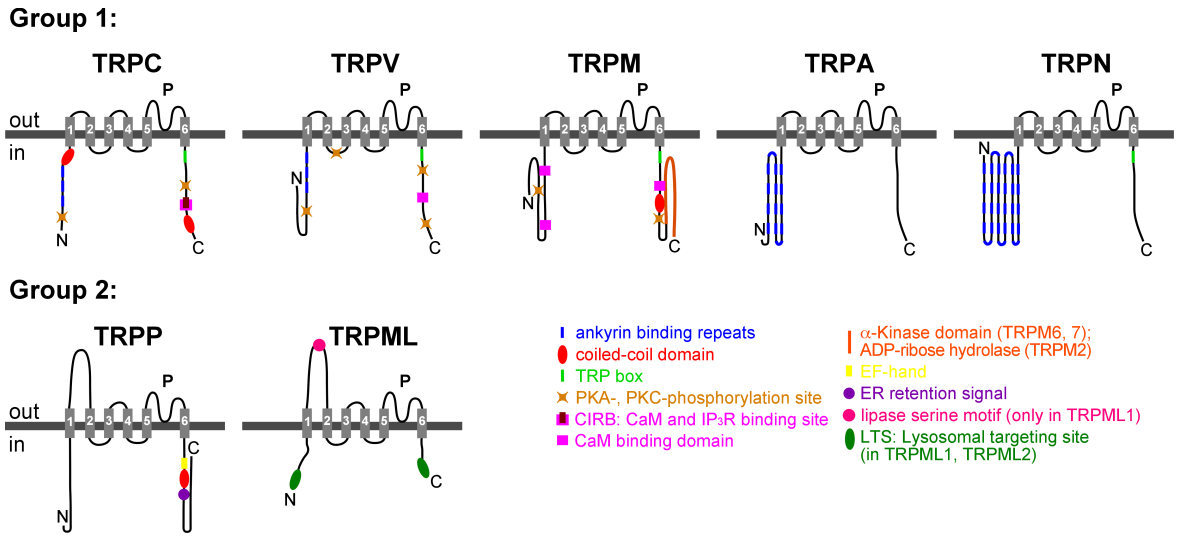

Figure 1: Schematic drawing of the TRP superfamily. Shown are both groups of TRP cation channels. The 6 transmembrane domains (TM) are illustrated in grey with the pore region (P) between TM5 and TM6. The intracellular termini are marked with N and C. The different domains are indicated in color: coiled-coil domain, ankyrin binding repeats, TRP box, protein kinase A phosphorylation site (PKA), protein kinase C phosphorylation site (PKC), Calmodulin binding domains (CaM), Inositol-triphosphate receptor binding site (IP_3R), enzymatic domains (α-kinase domain and ADP-ribose hydrolase), EF-hand motif, endoplasmatic reticulum retention signal (ER), lipase serine motif, and lysosomal targeting signals (LTS). (Adapted from Pedersen et al., 2005 and Venkatachalam and Montell, 2007.)

1.2 Hearing and TRP channels

1.2.1. Hearing and the architecture of the ear

The ear transforms mechanical energy into electrochemical energy. In mammals, the auditory portion of the inner ear is a coiled structure, called the cochlea, which is divided into three compartments, also known as *scalae* (Fig. 2A). These compartments are filled with fluids of distinct ionic composition: *scala vestibuli* and *scala tympani* contain perilymph, and *scala media* contains endolymph. Endolymph has an unusual composition for an extracellular fluid. It has a high K^+ concentration (~150 mM), but is low in Na^+ (~2 mM). In contrast to endolymph, perilymph is a more typical extracellular-like fluid with high Na^+ and low K^+. The potential between the endolymph and the perilymph, which is called endocochlear potential, is roughly +85 mV (Steel and Barkway, 1989; Yamasaki et al., 2000). The stria vascularis, a multilayered epithelium, generates the endocochlear potential and maintains the ionic composition of the endolymph, the fluid, which provides the driving force of sensory transduction (reviewed in Lang et al., 2007) (Fig. 2B). The border between the two fluids, endolymph and perilymph, is enforced with tight-junctions between the luminal cells. Maintenance of this barrier is essential for function of the inner ear.

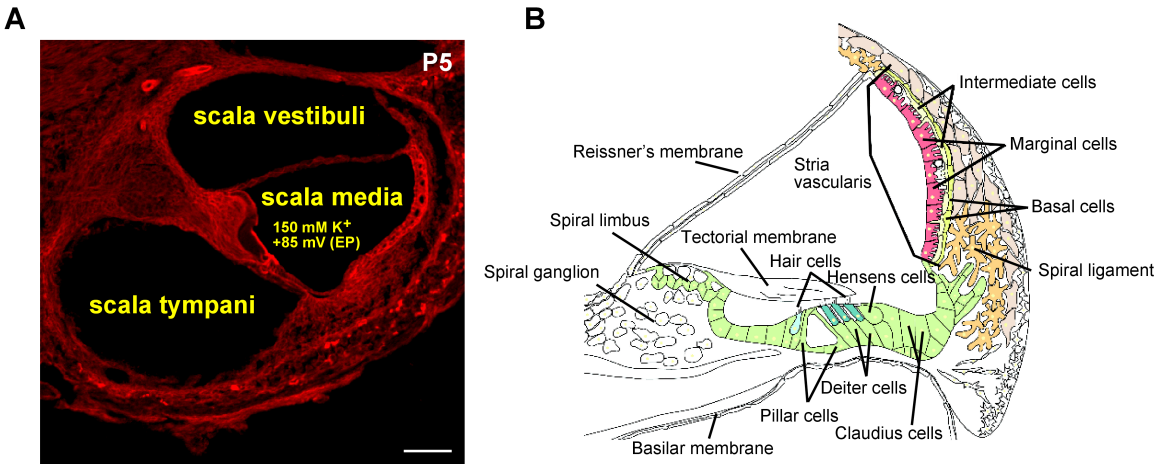

Figure 2: The mammalian cochlea. A: Shown are the three compartments: *scala vestibuli*, *scala media*, and *scala tympani* from a cross section of postnatal day 5 (P5) murine cochlea, which was labeled with FITC-conjugated phalloidin (F-actin). Phalloidin binds to filamentous actin. Scale bar = 100 µm. **B:** Schematic drawing of a cross section of the scala media with the surrounding structures such as the organ of Corti and the stria vascularis. Individual cell types are labeled. (Adapted from Cuajungco et al., 2007.)

Inside the cochlear duct is the organ of Corti. The organ of Corti contains the sensory hair cells with one row of inner hair cells (IHC) and three rows of outer hair cells (OHC), supporting cells and terminations of auditory nerve fibers. It sits on the top of the basilar membrane and is covered by the tectorial membrane (Fig. 2B, 3A). Incoming sound waves cause displacement of the basilar membrane, which excites the hair cells of the organ of Corti by deflecting their hair bundles to activate the mechanoelectrical transduction channels. The cochlea is tonotopically organized, which means that higher frequencies are being transduced at the base, whereas lower frequencies are transduced at the apex (for a review, see Fettiplace and Hackney, 2006).

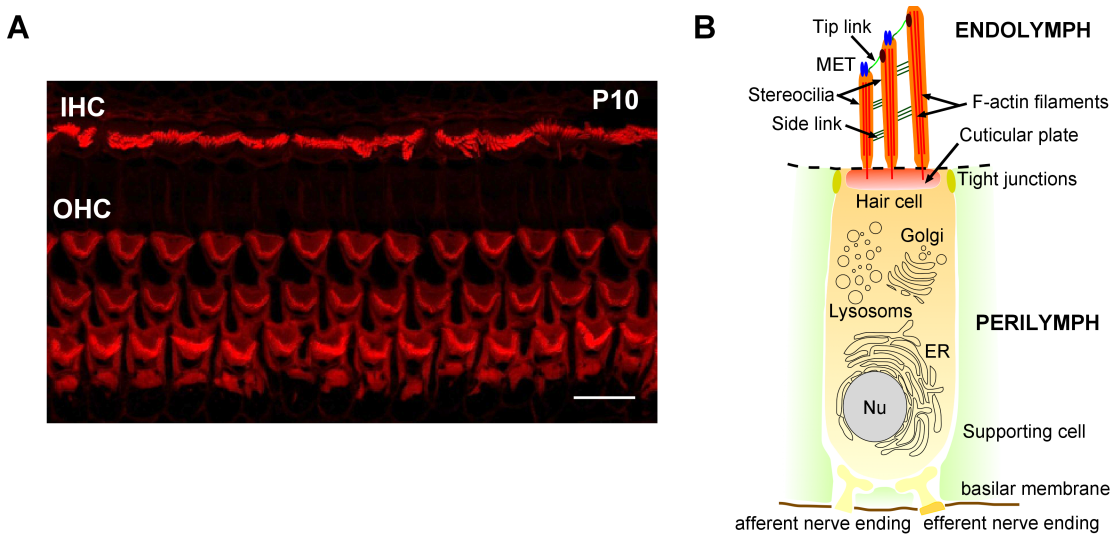

Figure 3: Hair cells. A: Shown is a view of the apical surface of the organ of Corti of a 10-day-old mouse (P10). The stereocilia of hair cells (one row of IHCs and three rows of OHCs) are visualized with FITC-conjugated phalloidin, which labels F-actin. Scale bar = 10 µm. **B:** Schematic model of a hair cell. The black broken line indicates the border between endolymph and perilymph, which is also referred to as reticular lamina (Raphael and Altschuler, 1991, for a review, see Raphael, 2002). MET = Mechanoelectrical transduction channel.

Hair bundles protrude into endolymph, and in the case of cochlear hair cells, they are typically organized into three rows of stereocilia, which are arranged like a staircase in ranks of increasing height. Extracellular filaments interconnect stereocilia within a hair bundle. Adjacent stereocilia are cross-linked along their shaft by side links, whereas tip links extend from the vertex of each stereocilium to the side of its taller neighbour (Fig. 3B). The shaft links, and a beveling of stereocilia at their base, make it possible that stereocilia pivot together as a unit, ensuring uniform excitation of the mechanoelectrical transduction channels (Kozlov et al., 2007). Mechanical deflection of the bundle towards the tallest stereocilia leads to shearing motions between adjacent stereocilia. The

consequential increase of mechanical tension in the transduction apparatus increases the open probability of mechanically gated ion channels (reviewed in Hudspeth, 2002).
The longest stereocilia of outer hair cells are in direct contact with the tectorial membrane. Upward displacement of the basal membrane stimulates the outer hair cells by pivoting their stereocilia against the tectorial membrane, which runs parallel to the basal membrane. Inner hair cell stereocilia may contact and be deflected by Hensen's stripe, a ridge running along the middle of the underside of the tectorial membrane just outside the position of the inner hair cell stereocilia (Edge et al., 1998, Forge and Wright, 2002). Opening of the mechanoelectrical transduction channels cause influx of cations from the endolymph into hair cells, which rapidly depolarize the cells. Recently, high-speed imaging of cochlear hair cells demonstrated that Ca^{2+} only enters the shorter stereocilium of a tip link connected pair, suggesting that transduction channels are only located at the base of the tip link (Beurg et al., 2008; and for a review, see Gillespie and Müller, 2009). The depolarization, in turn, leads to an influx of Ca^{2+} through voltage-gated L-type calcium channels located at or near the ribbon-type synapses at the base of the hair cells. Ca^{2+} influx triggers the fusion of synaptic vesicles leading to release of neurotransmitters (glutamate or a glutamate-like substance). This elicits the formation of action potentials in the afferent auditory nerve fibers that connect with the auditory brainstem in the central nervous system (for reviews, see Moser et al., 2006; Zanazzi and Matthews, 2009). The inner hair cells relay the afferent signal to the auditory neurons. The outer hair cells enhance the sensitivity and selectivity and have very little afferent innervations. Instead, they are efferently innervated by feedback loops that bring signals from the central nervous system to the outer hair cells, which assist in sharpening and amplifying the signals.

1.2.2. The hair cell transduction channel

Despite all efforts and more than 30 years of intense research, the molecular nature of the mechanosensitive ion channel carrying the receptor current into inner ear hair cells has not been identified. Nevertheless, several candidate proteins have been proposed, including members of the TRP superfamily such as **TRPN1, TRPV4, TRPA1,** and **TRPML3**.

Studies in invertebrates are providing a link between TRP channels and hearing (reviewed in Cuajungco et al., 2007). In *Drosophila melanogaster*, hearing is mediated by the Johnston's organ, a mechanosensory chordotonal organ in the pedicel of the antenna. The Johnston organ is consisting of more than 150 scolopidia, the multicellular

mechanoreceptor units. Each scolopedia contains a mechanosensory chordotonal neuron (Göpfert and Robert, 2002; for a review, see Eberl and Boekhoff-Falk, 2007). The Johnston's organ detects and funnels sound wave-evoked vibrations of the antenna to the cilia of the chordotonal mechanosensory neurons. The chordotonal organs are evolutionarily and functionally related to vertebrate cochlea (Boekhoff-Falk, 2005). The mechanosensitive protrusion of the chordotonal organs is bathed in high K^+ and low Ca^{2+} extracellular fluid, which is similar to the ionic composition of the endolymph surrounding the stereocilia of vertebrate hair cells. Mutations in the invertebrate TRP genes *NompC* (*Trpn1*), *Inactive*, and *Nanchung* have been shown to affect transduction in bristle and chordotonal mechanoreceptors of *Drosophila melanogaster* (Walker et al., 2000; Kim et al., 2003; Gong et al., 2004). TRPN1 and TRPV4 (closely related to *NompC*, *Inactive*, and *Nanchung*) have been considered for the mechanoelectrical transduction channel candidates of vertebrate hair cells. Based on expression in sensory hair cells, TRPML3 and TRPA1 have also been considered as candidates. In the following section, I will review each of these channels.

1.2.2.1. TRPN1

Although *Trpn1* was initially thought to be restricted to invertebrate animals, orthologs were found in zebrafish (*Danio rerio*) (Sidi et al., 2003) and African clawed frog (*Xenopus laevis*) (Shin et al., 2005). Knockdown studies with morpholino antisense oligonucleotides in fish showed that TRPN1-deficient animals displayed abnormal acoustic startle response and atypical swimming behavior. These phenotypes are characteristic for auditory and vestibular impairment. However, the exact function of TRPN1 in the mechanotransduction process remains unclear. A positive immunolabelling of TRPN1 was only observed in the kinocilium, but not in the stereocilia of hair cells, where the transduction channels are located (Shin et al., 2005). The *Trpn1* gene cannot be detected in the published genomic sequence of mammals and birds, which is a molecular phylogenetic conundrum (reviewed in Cuajungco et al., 2007).

1.2.2.2. TRPV4

It has been shown that *Inactive* and *Nanchung* are essential genes for mechanotransduction in *Drosophila melanogaster* (Kim et al., 2002; Gong et al., 2004). These two genes are most closely related to the vertebrate *Trpv4* cation channel gene. Originally, TRPV4 has been identified as an osmotically activated channel (Liedtke et al., 2000; Strotmann et al., 2000). However, it is also activated by mechanical stress (Liedtke et al., 2003), heat (Güler at al., 2002; Watanabe et al., 2002a), phorbol esters (Gao et al., 2003) and epoxyeicosatrienoic acid, a metabolite of arachidonic acid (Watanabe et al., 2003). TRPV4 is widely expressed, inclusive most cells lining the endolymphatic duct of the mouse ear, in cochlear hair cells and marginal cells of the stria vascularis (Liedtke et al., 2000; Shen et al., 2006). This expression pattern led to the hypothesis that TRPV4 might be involved in mechanoelectrical transduction or formation of the endolymph (Liedtke et al., 2000). Nevertheless, analysis of mice with an inactivation of the murine *Trpv4* gene revealed no overt hearing and balance defects (Heller and Liedtke, unpublished observations). It was later shown that the disruption of *Trpv4* causes delayed onset hearing loss in 6-months-old mice, and that the *Trpv4*$^{-/-}$ cochlea displays higher vulnerability to acoustic injury, suggesting that TRPV4 plays a role in the mature cochlea, but unlikely in hair cell mechanotransduction (Tabuchi et al., 2005).

1.2.2.3. TRPA1

TRPA1 was a prime candidate for a component of the hair cell's transduction machinery (Corey et al., 2004). TRPA1 mRNA is first detectable in the sensory epithelium of the mouse utricle at embryonic day 17 (E17), the developmental time when vestibular hair cells display functional transduction (Geleoc and Holt, 2003). Furthermore, TRPA1 protein was detected at or near the tips of the stereocilia of bullfrog and mouse hair cells, the place where the mechanotransduction machinery is localized. It has been shown that after disruption of the tip links, TRPA1 immunoreactivity was reduced. Finally, the knockdown of TRPA1 in zebrafish inner ear with morpholino oligonucleotides reduced the inner ear microphonic potential produced by vibration, and the inhibition of protein expression in mouse utricle hair cells with adenoviruses encoding siRNAs targeting TRPA1 impeded hair cell transduction (Corey et al., 2004). However, two independently generated knockout mouse lines revealed that TRPA1 is not essential for hair cell function (Kwan et al., 2006; Bautista et al., 2006). The knockout mice showed normal startle reflex, a normal sense of balance, normal auditory brainstem response (ABR), normal distortion

product otoacoustic emissions (DPOAE), and normal transduction currents. What went wrong? One explanation given was compensation. The absence of TRPA1 throughout hair cell development causes the upregulation of another channel to compensate. Compensation is a common problem in knockout mice (Dymecki, 2000). However, there is no other related channel gene that could compensate. TRPA1 has no close homolog, and is the only member of the TRPA subfamily. Alternatively, the TRPA1 supporting experiments might have been interpreted too optimistically leading the authors to draw the wrong conclusions from their data. One limitation of their study was that they did not contuct very stringent controls for the most crucial experiments knocking down TRPA1 in zebrafish and mouse. Morpholinos could disrupt development non-specifically, which could have misled the authors who did not probe hair cell function directly. siRNA, which was used in mice could have off-target effects and controls did not include expression of a control siRNA (Corey, 2006).

1.2.2.4. TRPML3

A mutant isoform of the murine *Trpml3* gene has been identified in a positional cloning approach as the cause of the murine varitint-waddler (*Va*) phenotype that is manifested in profound hearing loss, vestibular defects (circling behavior, imbalance, head-bobbing, waddling), pigmentation abnormalities, sterility, and embryonic lethality in homozygous animals (Cable and Steel, 1998; Kim et al., 2002; Di Palma et al., 2002). The *Trpml3* (*Va*) allele contains a single alanine to proline substitution at amino acid position 419 (A419P) in the fifth predicted TM of TRPML3 (Fig. 4). A second *Trpml3* variant (Va^J) has been identified, which arose in *cis* from the *Va* allele and shows a less severe phenotype, particularly in heterozygous mice. In addition to the A419P mutation, this variant carries a threonine for isoleucine at position 362 (I362T) in the second predicted extracellular loop (Di Palma et al., 2002) (Fig. 4).

Ultrastructural studies of *Va* and Va^J mouse cochleae demonstrated that the hearing loss is a result of progressive degeneration of sensory hair cells and intermediate cells in the stria vascularis. Stereocilia of hair cells were often fused together and reduced in number, or even completely absent. The hair cells showed swollen apical surfaces, rounded shapes, and reduced lengths, respectively (Cable and Steel, 1998; Di Palma et al., 2002; Atiba-Davies and Noben-Trauth, 2007). Intermediate cells are the only neural crest-derived cell type of the inner ear and contain melanin (Hilding and Ginzberg, 1977). They form a layer between marginal and basal cells in the stria vascularis (Fig. 2B), and play an important

role in maintaining the endochochlear potential at approximately +85 mV in the endolymph. As previously described, the endocochlear potential is necessary for cochlear hair cell function. In *Va*^{J} mice, it was shown that the endocochlear potential either was reduced or absent (Cable and Steel, 1998). This phenotype is due to degeneration or absence of strial intermediate cells.

Noben-Trauth and colleagues have been developed TRPML3-specific antibodies, which labeled inner and outer hair cells throughout the cell bodies in mouse and rat (Di Palma et al., 2002). TRPML3 was also detected at the base of neonatal mouse cochlear hair cell stereocilia between P2 and P6. Between P6 and P10, the protein is downregulated and after P10, TRPML3 is no longer detectable in stereocilia (van Aken et al., 2008). Based on these immunolocalization data and the discovery of *Trpml3* mutations that confer the *Va* phenotype, TRPML3 is one of the putative ion channel candidates of hearing transduction.

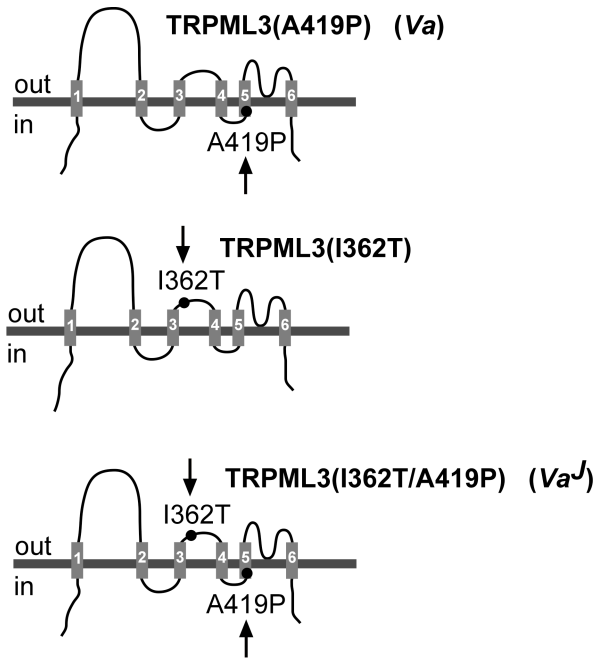

Figure 4: Schematic drawing of TRPML3 mutant variants. The illustrations are showing the position of A419P in TM5 and I362T in the second extracellular loop between TM3 and TM4. (From Grimm et al., 2007)

To date, the identity of the vertebrate hair cell mechanoelectrical transduction channel remains a mystery. PCR-based expression analyses show that many TRP channels are expressed in the mammalian organ of Corti (Cuajungco et al., 2007; Asai et al., 2009). Several TRP channels have been presented as hair cell transduction channel candidates. Yet, targeted gene deletion of single TRP genes has not revealed deficits in hair cell mechanotransduction (e.g. TRPA1 and TRPV4). However, since TRP channels may form

heteromers, the hair cell transduction channel might be composed of more than one type of TRP subunit. The subunits that remain may compensate for the absent subunits affected by the knockouts. Alternatively, the hair cell transduction channel could be composed of ion channels that do not belong to the TRP family. Despite the lack of evidence supporting a role for TRP channels in hair cell transduction, it is clear that mutations in certain TRP genes affect auditory function. Particularly TRPML3 shows a clear link between TRP and inner ear disorders. So far, it is not known whether loss of function of TRPML3, as in a knockout, affects hearing and pigmentation. In my thesis I am focusing on molecular and functional aspects of TRPML3, including the generation of a conditional *Trpml3* knockout mouse.

1.3. TRPML3 channel activity and regulation

1.3.1. The TRPML subfamily and its expression

The mammalian TRPML gene family consists of three members (TRPML1, TRPML2, and TRPML3). Loss-of function mutations in human TRPML1 cause the lysosomal storage disease Mucolipidosis Type IV (MLIV). MLIV is an autosomal recessive disease characterized by severe mental retardation and retinal degeneration (Bargal et al., 2000; Sun et al., 2000; reviewed in Bach, 2001). The murine *Trpml2* gene was discovered together with the *Trpml3* gene by positional cloning (Di Palma et al., 2002). Whereas TRPML1 is ubiquitously expressed, the expression of TRPML2 and TRPML3 is more restricted (Grimm et al., 2010). TRPML2 mRNA is highly expressed in thymus, heart, liver, kidney, spleen, pancreas, and skeletal muscle (Samie et al., 2009; Curcio-Morelli et al. 2009; Grimm et al., 2010). TRPML3 mRNA is detectable at low levels in most tissues, but is more abundant in kidney, thymus, eye, lung, skin, olfactory bulb, and inner ear (see Fig. 6 below, and Grimm et al., 2010). Subcellular localization studies of heterologously expressed murine or human TRPML channels revealed that TRPML1 and TRPML2 are expressed in late endosomes and lysosomes (Treusch et al., 2004; Venkatachalam et al., 2006) and that TRPML3 is localized to late endosomes and lysosomes, early endosomes, as well as the plasma membrane (Kim et al., 2009). As explanation for this distribution, it was postulated that TRPML3 shuttles between multiple intracellular compartments and the plasma membrane (Kim et al., 2009). The localization of all three TRPML proteins to intracellular compartments and the interaction with a variety of vesicular proteins has led to the hypothesis that the TRPMLs may play roles in the endocytic and exocytic signaling

pathways. They seem to be involved in the recycling of cellular membrane components and uptake of extracellular materials (reviewed by Cheng et al., 2010 and Puertollano and Kiselyov, 2009). My work confirms the subcellular localization of the three TRPML proteins (Figure 5). TRPML1 appears to be localized in intracellular vesicles, whereas TRPML2 and TRPML3 were found in intracellular compartments as well as near or at the plasma membrane, suggesting that TRPML2 also could play roles as plasma membrane channel protein.

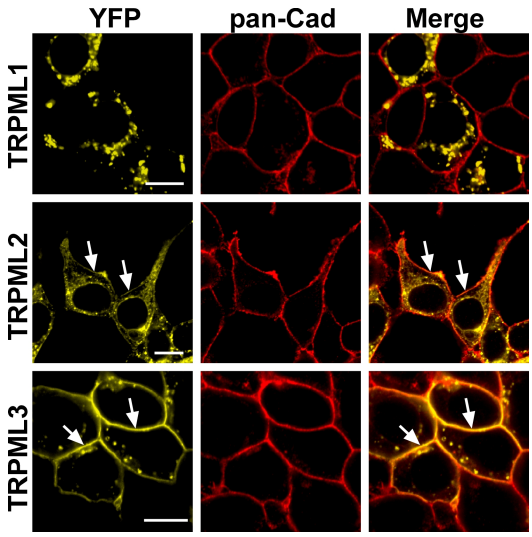

Figure 5. Expression of TRPML channel members in HEK293 cells. Shown are representative confocal micrographs of HEK293 cells overexpressing C-terminal YFP fusion constructs of TRPML1, TRPML2, and TRPML3 (yellow). Significant amounts of TRPML2 and TRPML3 were associated with the plasma membrane (white arrows), which is visualized with pan-Cadherin-Cy5 antibodies (red). Scale bar = 10 µm.

Heteromerization is an effective way of modulating channel function, subcellular localization, and biophysical properties of interacting TRP channels (Schaefer, 2005). Heteromerization of TRPML family members was detected by FRET (Fluorescence Resonance Energy Transfer) analysis in cells heterologously expressing TRPMLs (Venkatachalam et al., 2006; Grimm et al., 2010; for a review, see Puertollano and Kiselyov, 2009). Co-immunoprecipitation studies confirmed that TRPML1 forms heteromultimers with TRPML2 and TRPML3 (Curcio-Morelli et al., 2009). To investigate individual properties of TRPML homo- and heteromers, Curcio-Morelli and colleagues were using a lipid-bilayer reconstruction system, which is excluding other channels and/or regulatory proteins. The heteromeric channels retained channel activity and showed clear differences in channel activity from their respective homomers, a fact that supports the idea that multimerization could play an important role in TRPML channel function, and

that the interaction between TRPML proteins modifies channel function, i.e. generates channels with novel characteristics. Therefore, the combinatorial assembly of TRPML proteins, which are differently expressed in target tissues, might result in distinct tissue specific channels (Curcio-Morelli et al., 2009).

1.3.2. Varitint-waddler mutations render TRPML3 constitutively active

The varitint-waddler mouse model was providing us with a tool to study functional aspects of TRPML3 *in vitro* and *in vivo*. The varitint-waddler mutations A419P and I362T/A419P of TRPML3 lead to a constitutively open channel, resulting in highly elevated $[Ca^{2+}]_i$ causing apoptotic cell death (Grimm et al., 2007; Kim et al., 2007; Xu et al., 2007; Nagata et al., 2008, Grimm et al., 2009). Interestingly, the single I362T mutation does not affect $[Ca^{2+}]_i$ (behaving like wild-type TRPML3), demonstrating that only the A419P mutation is responsible for the phenotype (Grimm et al., 2007; Kim et al., 2007). In addition, the I362T mutation has no effect on the subcellular localization of TRPML3, but its presence reduces the surface expression of TRPML3(I362T/A419P) relatively to that of TRPML3(A419P). According to this, the milder phenotype of TRPML3(I362T/A419P) compared to TRPML3(A419P) is probably due to less channel transcripts in the plasma membrane (Grimm et al., 2007; Kim et al., 2007). Electrophysiological studies revealed an inwardly rectifying current in both TRPML3(A419P) or TRPML3(I362T/A419P)-expressing cells (Grimm et al., 2007; Kim et al., 2007; Xu et al., 2007; Nagata et al., 2008, Grimm et al., 2009). Similar currents were measured in outer hair cells of homozygous *Va*^{J} mice, showing that cochlear varitint-waddler hair cells experience cation influx through the mutated TRPML3 cation channel (Grimm et al., 2007).

How does the A419P mutation cause this gain-of function? It was postulated that proline introduces a α-helix-breaking kink, resulting in the destabilization of TM5, and converting TRPML3 in a constitutively open channel (Grimm et al., 2007; Kim et al., 2007). This was enforced by the fact that other TRP channels (TRPML1, TRPML2, TRPV5, and TRPV6) mutated at positions in TM5 equivalent to TRPML3 A419 to proline, also evoked elevated $[Ca^{2+}]_i$ when compared to the respective wild-type isoforms (Grimm et al., 2007).

It is remarkable that sensory hair cells survive for several postnatal weeks, whereas other cells, such as cochlear intermediate cells or normal skin melanocytes, die before birth. It was shown that HEK293 cells expressing the *Va* isoforms died already after 10 hours after transfection, which is due to the massive overexpression in this heterologous expression system (Grimm et al., 2007, Grimm et al., 2009).

One of the aims of my study (Aim 1, see below) was to investigate whether the survival of varitint-waddler hair cells is linked to their ability to deal with Ca^{2+} loads due to the abundance of endogenous plasma membrane calcium ATPases (PMCA2). This work has been published in *The Journal of Biological Chemistry* (Grimm*, Jörs* et al., 2009) and will be presented and discussed in the *Results* part 3.1.

* Contributed equally

1.3.3. TRPML3 is regulated by sodium and pH

Previous studies have implicated that the wild-type TRPML3 channel is a non-selective Ca^{2+}-permeable channel that is regulated by extracytosolic Na^+ and H^+ (Kim et al., 2007; Kim et al., 2008; Grimm et al., 2010).

Kim et al. reported that TRPML3 heterologously expressing cells bathing in Na^+-free solution showed activation after exposure to high Na^+ (140 mM), followed by a spontaneous current inactivation. Our group has confirmed that low extracellular Na^+ concentration increases the open probability of TRPML3 (Grimm et al., 2010). The regulation by Na^+ is an interesting feature of wild-type TRPML3, because the transient expression of TRPML3 in the base of sensory hair cell stereocilia in the mouse cochlea (van Aken et al., 2008) coincides with changes of ionic composition of the cochlear endolymph. Between P0 and P5, when TRPML3 expression reaches its highest level in the apical membrane of sensory hair cells, the endolymphatic Na^+ drops from 36 mM to 4.1 mM, and K^+ increases from 104 mM to 134 mM. At P7, all ions reach adult endolymphatic concentration (low Na^+ 2.8 mM and high K^+ 202 mM) (Yamasaki et al., 2000), when TRPML3 immunoreactivity is starting to disappear in stereocilia (Di Palma et al., 2002; van Aken et al., 2008).

Native and heterologously expressed TRPML3 is not only present in the plasma membrane, but also in endosomes and lysosoms, which are acidic (Grimm et al., 2007; Kim et al., 2007; Kim et al., 2009, Xu et al., 2007; Nagata et al., 2008; Di Palma et al., 2002, van Aken et al., 2008, for reviews, see Cheng et al., 2010 and Puertollano and Kiselyov, 2009). TRPML3 activity is almost completely suppressed at pH 6.0 (Kim et al., 2008). The inactivation by acidity is in agreement with the primary localization of TRPML3 within the less acidic endocytic pathway. TRPML3 may provide the Ca^{2+} that is required for the fusion or fission reactions in endocytosis (Kim et al., 2009). A mutagenesis screening of histidines in extracellular domains of TRPML3 revealed that the regulation of TRPML3 by H^+ is mediated by three histidines (H252, H273, and H283) in

the large extracellular loop between TM1 and TM2. The inhibition is mainly controlled by H283, whereas H252 and H273 are believed to tunnel the H^+ to H283 (Kim et al., 2008).

In summary, TRPML3 is an inwardly rectifying cation channel that is permeable to Ca^{2+} and regulated by extracytosolic Na^+ and H^+. Although there was a lot of progress in characterization of heterologously expressed TRPML3 and its isoforms, the physiological role of wild-type TRPML3 remains unclear. The identification of natural and artificial activators and inhibitors could be an important step toward a better understanding of ion channel characteristics and its *in vivo* functionality. For many TRPC, TRPV, and TRPM family members specific activators have been identified, including synthetic compounds and natural products like capsaicin (TRPV1), 2-aminoethoxydiphenyl borate (TRPV1-TRPV3), or icilin (TRPM8 and TRPA1), endogenous lipids or products of lipid metabolism like diacylglycerols (TRPC3, 6, and 7), eicosanoids (TRPV4) or anandamide (TRPV1). In contrast to the increasing number of ligands, activators, and antagonists for most of the today known TRP channels (for reviews, see Ramsey et al., 2006; Clapham, 2007; Patapoutian et al., 2009), there were neither activators nor selective inhibitors known so far for members of the TRPML subfamily. This lack of specific activators was one of the major limitations towards a better understanding of the characteristics and the functionality of TRPML channels. The identification of first small molecule TRPML3 activators will be described in *Results* part 3.2. This work has recently been published in *Chemistry & Biology* (Grimm*, Jörs* et al., 2010).

* Contributed equally

1.4. TRP knockout mice and the need of a *Trpml3* knockout mouse model

A very important step toward elucidating the physiological role of TRPML3 *in vivo* is the generation of a conditional *Trpml3* knockout mouse. So far, knockout mice of TRP channels of all subfamilies have been generated. The phenotypes of these mice comprise impaired endothelium-dependent vasorelaxation (TRPC4), defective vasomotor control (TRPC6), defective calcium reabsorption (TRPV5), failure in detection of sweet, bitter, or umani flavors (TRPM5), defects in thymocyte development (TRPM7), suppression of inflammatory thermal hyperalgesia (TRPV1), defective thermosensation (TRPV3), impaired osmoregulation (TRPV4), and recessive neurodegenerative lysosomal storage disorder (TRPML1) (for reviews, see Desai and Clapham, 2005; Clapham, 2007; Wu et al., 2010). TRPML3, on the one hand, has clearly been proven to be expressed in cells of the inner ear and the varitint-waddler mutations of the channel lead to hair cell degeneration and deafness. On the other hand, hair cell death-mediated deafness (due to a constitutive active ion channel) is not sufficient to justify a function in the hearing process itself. To elucidate a hearing relevant function in hair cells, a potential function in hearing development, or in hair cell mechanotransduction, it is essential to study TRPML3 in a knockout model. The possibility that TRPML3 functions as the highly elusive mechanotransduction channel in the inner ear, or as a component of a heteromeric channel complex cannot be ruled out based on our current knowledge about TRPML3. This is of special importance since the most promising candidates, TRPA1 (Bautista et al., 2006, Kwan et al., 2006) and TRPV4 (Tabuchi et al., 2005) could not be confirmed as the mechanotransduction channel (see 1.2.2.2 and 1.2.2.3.). The widespread expression profile of TRPML3 in mouse (Fig. 6) and human (Grimm et al., 2010), however, suggests that this protein has additional functional roles in a variety of tissues and organs, and that its function is most likely not restricted to melanocytes, intermediate cells, and hair cells of the inner ear.

Recently, it has been shown that TRPML3 mRNA is upregulated in animal models of neuropathic pain (Staaf et al., 2009). Neuropathic pain is resulting from disease, damage, or dysfunction of the peripheral or central nervous system (Scadding, 2003; Basic-Kes et al., 2009). Approximately 7 to 8% of the population is affected by chronic pain and in 5%, the situation is severe to disabling (Torrance et al., 2006; Bouhassira et al., 2007). The occurrence of TRPML3 in dorsal root ganglia (DRG) sensory neurons is an important piece of information in this regard, which suggests that TRPML3-deficient mice might have a phenotype in chronic pain sensation; likewise, this hypothesis also implies that the

varitint-waddler mouse model might display sensory deficits that have not been discovered.

The analysis of the hearing and vestibular phenotype in mice with conditionally inactivated *Trpml3* has recently been published in *PLoS ONE* (Jörs*, Grimm* et al., 2010) and will be presented and discussed in the *Results* part 3.3.

* Contributed equally

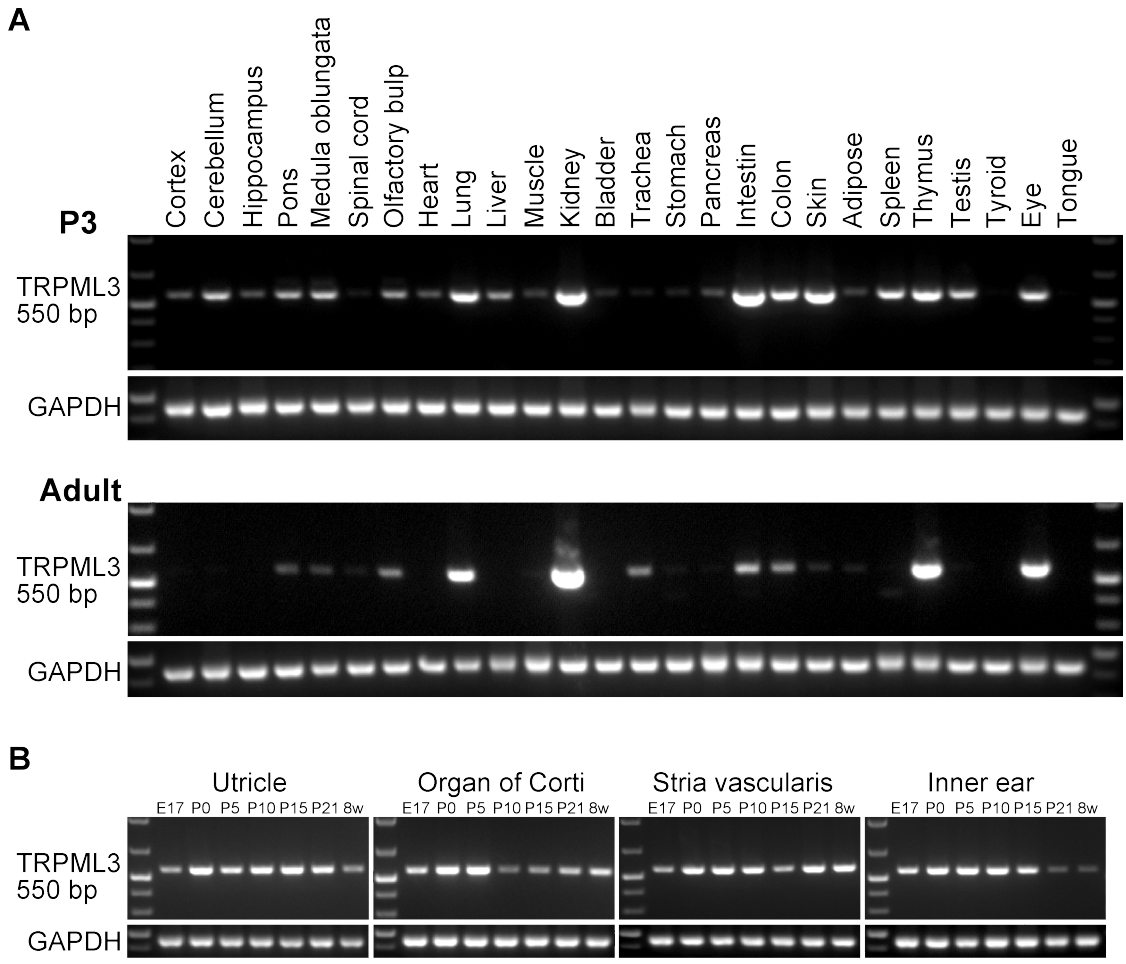

Figure 6: RT-PCR analysis of TRPML3 channel expression in various murine organs and tissues. Shown is amplified cDNA representing murine TRPML3 (550 bp) and GAPDH (442 bp). Inbred FVB/NJ wild-type mice were used. **A:** Organs and tissue were taken from P3 and 8-week-old mice. **B:** TRPML3 channel expression in murine inner ear at different ages is shown, starting with E17 and ending with 8 weeks. Inner ear = whole otic capsule. TRPML3 expression in the murine inner ear was published as supplemental Figure S5 in Grimm et al. 2010.

1.5. Specific Aims

My goal was to broaden our understanding of the physiological role and particularly the *in vivo* function of the TRPML3 protein, a member of the transient receptor potential family of non-selective cation channels. Toward this goal, I proposed the following specific aims:

My first aim was:

to investigate the mechanism by which sensory hair cells are able to deal with severe Ca^{2+} overloads caused by constitutive activity of the TRPML3 channel in varitint-waddler mice. I hypothesized that this ability to deal with Ca^{2+} loads is linked to the abundance of plasma membrane calcium ATPases (PMCA2) in hair cells. *In vitro* experiments were showing that HEK293 cells expressing TRPML3(A419P) or TRPML3(I362T/A419P) undergo rapid apoptosis. This apoptosis is suppressed by coexpression of PMCA2.
To test the hypothesis *in vivo*, I proposed to cross varitint-waddler mice with PMCA2 mutant mice (deaf-waddler) and with control mice, respectively. The deaf-waddler PMCA2 isoform is operating at 30% efficacy when compared to the wild-type protein. My expectation was that the reduction in the Ca^{2+} extrusion ability of hair cells would increase the severity of the varitint-waddler phenotype. I expected that the combination of both alleles would aggravate the hair bundle defects and hair cell loss. To study hair cell morphology, I investigated whole-mount preparations (organ of Corti and utricle) of P10 and P21 mice carrying single varitint-waddler and deaf-waddler alleles as well as double mutants. Furthermore, I was performing auditory brainstem response measurements to evaluate hearing thresholds of P21 mice carrying the different combinations of varitint-waddler and deaf-waddler alleles.

My second aim was:

to identify small compound activators of the TRPML3 cation channel. The identification of natural or artificial activators is an important step toward a better understanding of TRPML3's ion channel characteristics and its *in vivo* functionality. Furthermore, there are no activators known for members of the TRPML subfamily, which makes the characterization of channel properties difficult.
I hypothesized that identified activators could be used as tools to activate TRPML3 in native cell types, such as sensory hair cells and primary epidermal melanocytes. The screen was done by using a stable HEK293 cell line that expresses human TRPML3 in

conjunction with a high-throughput compound screen, using FLIPR-based calcium imaging technology.

My third aim was:

to generate a floxed allele of the mouse *Trpml3* gene (*Trpml3*$^{loxP\text{-}exon11\text{-}loxP}$).
It has been shown that naturally occurring murine *Trpml3* mutations (*Va* and *Va*^{J}) lead to deafness. However, only a knockout mouse model can clearly reveal whether TRPML3 plays an important role in hearing processes itself or in the development of hearing. To elucidate the physiological role of TRPML3 in the inner ear, I successfully generated a genetic conditional *Trpml3* inactivation in mice. I was initially investigating the conditional inactivation of *Trpml3* in the mouse inner ear using a Tamoxifen-inducible sensory hair cell-specific allele of the Cre recombinase, *Math1-CreER*^{TM}. In a second approach, I was creating a general inactivation by crossing the *Trpml3*$^{loxP/}$ mice with the *Hprt*^{Cre} transgenic mouse line expressing Cre recombinase ubiquitously. The result was an excised *Trpml3* exon 11 in all tissues. In both models, I was directly investigating the effects of the absence of TRPML3 on hearing and balance.

2. Materials and Methods

2.1. Materials

2.1.1. Manufacturers

(1) Astro-Med, West Warwick, RI, USA
(2) Asinex Ltd., Moscow, Russia
(3) ATCC, Manassas, VA, USA
(4) BD-Bioscience, San Jose, CA, USA
(5) Bio-Rad Laboratories, Hercules, CA, USA
(6) ChemBridge, San Diego, CA, USA
(7) ChemDiv, San Diego, CA, USA
(8) Chemicon, Temecula, CA, USA
(9) Clontech, Mountain View, CA, USA
(10) Dako, Carpinteria, CA, USA
(11) EMD Chemicals Inc., Darmstadt, Germany
(12) Enamine, Kiev, Ukraine
(13) Fermentas Inc., Glen Burnie, MD, USA
(14) FINNZYMES OY, Espoo, Finland
(15) Fisher Scientific Inc., Pittsburgh, PA, USA
(16) IDT – Integrated DNA Technologies, San Diego, CA, USA
(17) Intelligent Hearing System, Miami, FL, USA
(18) Invitrogen, Carlsbad, CA, USA
(19) Jackson Research Laboratories Inc., West Grove, PA, USA
(20) Key Organics, Camelford, Cornwall, UK
(21) Lab scientific, New Jersey, NJ, USA
(22) LI-COR Biosciences, Lincoln, NE, USA
(23) Lonza Walkersville, Inc., Walkersville, MD, USA
(24) Maybridge, Cambridge, UK
(25) Mediatech, Inc, Cellgro, Manassas, VA, USA
(26) New England BioLabs, Ipswich, MA, USA
(27) Omega scientific, Inc, Tarzana, CA, USA
(28) Osenses, Flagstaff Hill, Australia
(29) QIAGEN, Valencia, CA, USA

(30) Promega, Madison, WI, USA
(31) Roche, Mannheim, Germany
(32) Rockland Immunochemicals, Gilbertsville, PA, USA
(33) Santa Cruz Biotechnology, Inc., Santa Cruz, CA, USA
(34) Sigma-Aldrich, St. Louis, MO, USA
(35) Specs, Delft, Holland
(36) Stanford University, Environmental Health & Safety, CA, USA; veterinary supplier
(37) Stanford University, Department of Comparative Medicine, CA, USA
(38) Stratagene, La Jolla, CA, USA
(39) The Jackson Laboratory, Bar Harbor, ME, USA
(40) Thermoscience, Rockford, IL, USA
(41) USB, Cleveland, OH, USA
(42) Viagen Biotech Inc., Los Angeles, CA, USA
(43) VWR International Inc., West Chester, PA

2.1.2. Chemicals

Fura-2-AM (18)
PMFS (Phenylmethanesulfonyl fluoride) (34)
Pluronic F-127 (34)
Protease Inhibitor Cocktail Tablets (34)
SF-11 3-(4-chlorophenyl)-5-methyl-4-[2-(4-methylphenyl)sulfonylpyrazol-3-yl]-1,2-oxazole (24)
SF-21 4-chloro-N-(2-morpholin-4-ylcyclohexyl)benzenesulfonamide (2)
SF-22 5-chloro-N-(2-piperidin-1-ylphenyl)thiophene-2-sulfonamide (12)
SF-23 5-chloro-N-(2-morpholin-4-ylphenyl)thiophene-2-sulfonamide (12)
SF-24 4-methyl-N-(2-phenylphenyl)benzenesulfonamide (6)
SF-31 1-(4-ethoxynaphthalen-1-yl)sulfonylazepane (2)
SF-32 1-(4-ethoxy-2,3-dimethylphenyl)sulfonylpiperidine (6)
SF-33 5-chloro-N,N-diethyl-4-methyl-2-propoxybenzenesulfonamide (35)
SF-41 1-(2,4-dimethylphenyl)-4-piperidin-1-ylsulfonylpiperazine (2)
SF-51 2-[2-oxo-2-(2,2,4-trimethylquinolin-1-yl)ethyl]isoindole-1,3-dione (6)
SF-61 4-(2-methoxyphenyl)spiro[3,4-dihydropyrazole-5,8'-6,7-dihydro-5H-benzo [7]annulene]-9'-one (35)

SF-71 [2-tert-butyl-5-methyl-4-(4-methylphenyl)sulfonylpyrazol-3-yl] butanoate (7), (20)

SF-81 4,6-dimethyl-3-(2-methylphenyl)sulfonyl-1-propan-2-ylpyridin-2-one (6), (19)

SN-1 N-tert-butyl-3-(3-tert-butyl-1-methyl-7-oxo-4H-pyrazolo[4,3-d]pyrimidin-5-yl)-4-ethoxybenzenesulfonamide (2)

SN-2 5-mesityl-3-oxa-4-azatricyclo[5.2.1.0~2,6~]dec-4-ene (35)

Sodium orthovanadate (34)

Tamoxifen (34)

All substances were dissolved according to manufacturers' instructions. Other chemicals for preparation of buffers, media, and solutions were obtained from Sigma (34), Fisher Scientific (15), Bio-Rad (5), USB (41), EMD (11), Invitrogen (18), and VWR, respectively (43).

2.1.3. Materials for molecular methods and cell culture

Amaxa - NHEM-Neo Nucleofector Kit (23)

DirectPCR DNA extraction reagent (42)

DNeasy Blood & Tissue Kit (29)

EndoFree Plasmid Maxi Kit (29)

Genejammer (38)

GeneJet™ Plasmid Miniprep Kit (13)

HighSpeed Plasmid Maxi Kit (29)

Pierce BCA Protein Assay Kit (40)

QIAGEN Gel extraction kit (29)

QuikChange Site-Directed Mutagenesis Kit (38)

RNeasy Mini-Kit (29)

1kb DNA Ladder and Orange DNA Loading Dye (13)

2.1.4. Enzymes

Alkaline Phosphatase Calf Intestine (CIP) (26)

Go-Taq Master-Mix (30)

Cloned *Pfu* DNA polymerase (38)

PfuTurbo DNA polymerase for QuikChange Site-Directed Mutagenesis (38)

Phusion DNA polymerase (14)

Recombinant DNaseI (RNase-free) (31)

Restriction endonucleases (26)

SuperScript™ III Reverse Transcriptase (18)

T4 DNA Ligase (30)

Trypsin-EDTA (25)

2.1.5. Bacterial strains

Escherichia coli:

DH5α: *fhuA2Δ(argF-lacZ)U169 phoA glnV44 Φ80 Δ(lacZ)M15 gyrA96 recA1 relA1 endA1 thi-1 hsdR17* (25)

XL1-Blue: *recA1 endA1 gyr96 thi-1 hsdR17 supE44 relA1 lac [F' proAB lacI^{q}ZDM15 Tn10 (Tet^r)]* (37)

TOP10: F- *mcrA Δ(mrr-hsdRMS-mcrBC) ϕ80lacZΔM15 ΔlacC74 recA1 araD139Δ(ara-leu)7697 galU galK rpsL (Str^R) endA1 nupG*

2.1.6. Plasmids

Genes encoding for wild-type and mutant TRP channels (hTRPML1, mTRPML2, human and murine TRPML3, hTRPM2, mTRPV2, mTRPV5, hTRPC3, drTRPN1, and hTRPA1) were C-terminally fused to either yellow fluorescent protein (YFP) or HA-tag. Expression vectors were based on pcDNA3.1 (18). The *Trpml3* knockout construct was assembled into pBlueskript II SK (+) vector (38). Table 1 shows the synthetic oligonucleotides and cloning strategies of TRPML1, TRPML2, TRPML3, and conditional *Trpml3* knockout targeting construct, respectively. HTRPML1 and mTRPML2 cDNAs were subcloned into pcDNA3.1 and then C-terminally fused to YFP using restriction endonuclease *Xho*I. Human and murine TRPML3 cDNAs were directly ligated via *Bam*HI and *Eco*RI into pcDNA3.1-YFP. The N-terminal lysosomal targeting site (LTS) in TRPML1 (TRPML1(N)) was deleted by using a sense oligonucleotide complementary to a sequence downstream of the N-terminal LTS, simultaneously introducing an alternative start codon (ATG). TRPML1(C) and TRPML1(NC) were obtained by mutagenesis using either wild-type TRPML1 or TRPML1(N) as a template (see 2.2.1.2.). The rat PMCA2z/a cDNA plasmid was provided by Dr. Peter G. Gillespie (Oregon Hearing Research Center, Portland, OR, USA). Wild-type dynamin and dynamin K44A mutant cDNA was provided by Dr. Shmuel Muallem (UT Southwestern, Dallas, TX, USA). Dr. Math. P. Cuajungco (California State University Fullerton, CA, USA) kindly provided human TRPML1-

shRNA 1208 expression vector U6 RNA Pol III. All plasmid cDNAs were verified by sequencing both strands entirely. Samples were sent to the sequencing service Genewiz, Inc., South Plainfield, NJ, USA.

2.1.6.1. pcDNA3.1 (+/-)

pcDNA3.1 is a 5.4 kb vector designed for high-level stable and transient expression in mammalian hosts (18). Only pcDNA3.1 (+) was used for cloning. The vector contains the following elements (Fig. 7):

- Human cytomegalovirus immediate-early promoter (P_{CMV}) for high-level expression in mammalian cells
- Multiple cloning site (MCS) in forward (+) and reverse (-) orientation to facilitate cloning
- Neomycin resistance gene for selection of stable cell lines
- Amplicillin resistance gene (ß-lactamase) for selection of the vector in *E.coli*
- F1 origin allows rescue of single-stranded DNA
- SV40 early promoter and origin allows high-level expression of the neomycin resistance gene and episomal replication in cells expressing SV40 large T antigen
- SV40 early polyadenylation signal (SV40 pA) for efficient transcription termination and polyadenylation of mRNA
- pUC origin allows high-copy number replication and growth in *E.coli*

The insert must contain a Kozak translation initiation sequence and an ATG start codon for proper initiation of translation. The used Kozak consensus sequence was CACCATGG, the ATG initiation codon is shown underlined.

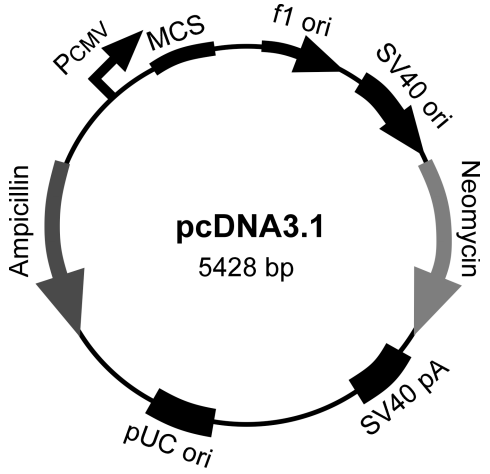

Figure 7: pcDNA3.1. The map summarizes the features of pcDNA3.1 (+) and (-).

2.1.6.2. pBluescript II SK (+/-)

pBluescript is a 3.0 kb phagemid (plasmids with a phage origin) and is designed for commonly used cloning and sequencing procedures. The conditional *Trpml3* knockout construct was assembled into pBlueskript II SK (+) vector (38), which contains the following elements (Fig. 8):

- Multiple cloning site (MCS) to make cloning easier
- Amplicillin resistance gene (ß-lactamase) for selection of the vector in *E.coli*
- F1 origin (in forward and reverse orientation available) allowing rescue of single-stranded DNA
- pUC origin allows replication and growth in *E.coli*
- *LacZ*' gene (ß-galactosidase) driven by a lac promoter (P_{lac}) and interrupted by the MCS

pBluescript II phagmids having no inserts in the MCS will produce blue colonies in the appropriate strains of bacteria. pBluescript II phagemids that have inserts will produce white colonies using the same strain, because the inserts disrupt the coding region of the *lacZ*' gene fragment.

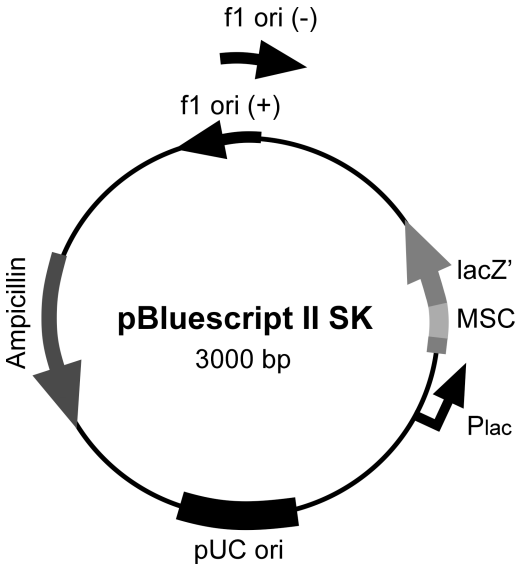

Figure 8: Bluescript II SK (+/-). The map summarizes the features of pBluescript II SK (+/-).

2.1.7. Antibiotics - resistance and concentration

Antibiotic:	**Solvent:**	**Final concentration:**
Ampicillin (Amp)	*A. bidest.*	100 µg/ml
Kanamycin (Km)	*A. bidest.*	50 µg/ml
Geneticin (G418)	*A. bidest.*	0.8 mg/ml

2.1.8. Oligonucleotides

All oligonucleotides were purchased from IDT – Integrated DNA Technologies, San Diego, CA, USA (16). The oligonucleotides were delivered as lyophilisates, which were dissolved to a final concentration of 100 pmol/µl in sterile nuclease free water and stored at -20ºC (Table 1-4).

Table 1: Synthetic oligonucleotides used for cloning. Restriction endonucleases are indicated in bold, HA-tag and *loxP* site were highlighted in grey. Abbreviations: sn = sense, asn = antisense, LA = left arm, RA= right arm, neo^R = neomycin resistance, DTA = Diphtheria toxin A.

Oligonucleotides	Gene	Strategy
5'-**CTCGAG**CACCATGACAGCCCCGGCGGGT-3'	hTRPML1 sn	*Xho*I
5'-ATTCACCAGCAGCGAATGCTCCTCCGAG-3'	hTRPML1 asn	w/o stop ; TOPO cloning pcDNA3.1 (Grimm et al., 2007)
5'- CACCATGACAGCCCCGGCGGGTCCGCGCGGCT C-3'	hTRPML1-HA sn	
5'-TTAAAGAGCGTAGTCTGGGACTGCATATGGAT AATTCACCAGCAGCGAATGCTCCTCC-3'	hTRPML1-HA asn	w/o stop in frame with HA-tag; TOPO cloning pcDNA3.1 (18)
5'-GAGA**AAGCTT**ACCATGCCCAACCCCGGTATG GGACCCA-3'	hTRPML1(N)-YFP sn	*Hin*dIII; insertion of an alternate ATG; template hTRPML1-YFP
5'-TCTC**CTCGAG**CGGCCGCCACTGTGCTGG-3'	hTRPML1(N)-YFP asn	*Xho*I
5'-**CTCGAG**CACCATGGCGTCTCCGATTCTGAGGT GAG-3'	mTRPML2 sn	*Xho*I
5'-GTCAATGAGAATCAAGTGGTCATTGCTTCTT C-3'	mTRPML2 asn	w/o stop ; TOPO cloning pcDNA3.1 (Grimm et al., 2007)
5'-CACCATGGCGTCTCTCGATTCTGAGGTGAG-3'	mTRPML2-HA sn	
5'-TTAAAGAGCGTAGTCTGGGACGTCATATGGAT AGTCAATGAGAATCAAGTGGTCATTGC-3'	mTRPML2-HA asn	w/o stop in frame with HA-tag; TOPO cloning pcDNA3.1 (18)
5'-GGA**GGATCC**ACCATGGCAGATCCTGAGGTAG TTGTG-3'	hTRPML3-YFP sn	*Bam*HI
5'-CCT**GAATTC**CCCTTTTTACAACAGCAGAATAA AGATACT-3'	hTRPML3-YFP asn	*Eco*RI w/o stop in frame with YFP (Grimm et al., 2007)
5'-CACCATGGCAGATCCTGAGGTAGTT-3'	hTRPML3-HA sn	
5'-TTAAAGAGCGTAGTCTGGGACGTCATATGGAT ACTTTTTACAACAGCAGAATAAAGATACT-3'	hTRPML3-HA asn	w/o stop in frame with HA-tag; TOPO cloning pcDNA3.1 (18)
5'-GGA**GGATCC**ACCATGGCAAATCCCGAGGTGC TGGTT-3'	mTRPML3-YFP sn	*Bam*HI
5'-CCTGAATTCCCCTTTTTGCAGCAGCAGAGTAA AGAACCC-3'	mTRPML3-YFP asn	*Eco*RI w/o stop in frame with YFP (Grimm et al., 2007)

5’-CACCATGGCAAATCCCGAGGTGCTGGTT-3’	mTRPML3-HA sn	
5’-TTAAAGAGCGTAGTCTGGGACGTCATATGGATACTTTTTGCAGCAGCAGAGTAAAGAACCC-3’	mTRPML3-HA asn	w/o stop in frame with HA-tag; TOPO cloning pcDNA3.1
5’-GAGA**AAGCTT**ATGGGTGATATGACCAACAGCGACTT-3’	rPMCA2 sn	*Hin*dIII
5’-**GCGGCCGC**CAAAGCGACGTCTCCAGGCTGTGGATGG-3’	rPMCA2 asn	*Not*I into pcYFP
5’-G**ACTAGT**CAGTGTGGTTTTCAAGAGGAAGC-3’	*Trpml3* knockout DTA sn	*Spe*I
5’-G**GAGCTCgcggccgc**GGGGGGCCGGTACCAGATCTA-3’	*Trpml3* knockout DTA asn	*Sac*I / *Not*I
5’-CCC**AAGCTT**AGTACTAGAACGAAGTTCCTATACT-3’	*Trpml3* knockout neo^R sn	*Hin*dIII
5’-C**AAGCTT**CCCTTAATATAACTTCGTATAATGTA-3’	*Trpml3* knockout neo^R asn	*Hin*dIII
5’-ACGC**GTCGACgcggccgc**ATACTGTGGATGATTTAGGCTGCTG-3’	*Trpml3* knockout LA 5’ arm sn	*Sal*I / *Not*I
5’-ACGC**GTCGAC**AAACAGACTGAACAACTTCACTGGTGG-3’	*Trpml3* knockout LA 5’ arm asn	*Sal*I
5’-TCCcccgggATGGGGTTATAGGCAGCCTAGGAGTA-3’	*Trpml3* knockout RA 3’ arm sn	*Sma*I
5’-TCC**CCCGGG**TTGATGTCAAGAGTCTTCCACAATTGCTCTCCACTTAAT-3’	*Trpml3* knockout RA 3’ arm asn	*Sma*I
5’-GAGA**GAATTC**ACTCAAACACATCTGTAAAACTGT-3’	*Trpml3* knockout exon 11 sn	*Eco*RI
5’-**GAATTC**ataacttcgtataatgtatgctatacgaagttatCCAGCCAATGTGAAGGAAGTTCCTTGG-3’	*Trpml3* knockout intron- exon 11-loxP asn	*Eco*RI

Table 2: Sequences of synthetic oligonucleotides used for QuikChange reactions. Nucleobases, which introduce point mutations and insertions are written in bold. Oligonucleotides used for the generation of a deletion were marked by a two color code; sequence following the deletion is shown in grey, sn = sense, asn = antisense.

***Trpml3* knockout construct - troubleshooting**	
5'-GAACTTCCTTCACATTGGCTGGGAATTCCTGCAGCCCGGGATGG-3'	*loxP* deletion step1 sn
5'-CCATCCCGGGCTGCAGGAATTCCCAGCCAATGTGAAGGAAGTTC-3'	*loxP* deletion step1 asn
5'-CCTTCACATTGGCTGGGAATTCATGGGGTTATAGGCAGCCTAG-3'	vector deletion step2 sn
5'-CTAGGCTGCCTATAACCCCATGAATTCCCAGCCAATGTGAAGG-3'	vector deletion step2 asn
5'-GACACATACGAAACAATTAAGGTAGGCTTGTCAGAAGCCGG **ataacttcgtatagcatacattatacgaagttat**TTAATTAAAGGCTCTGCCTATCTAGA ACCGTGTGTGGCGGCACAGCTTGG-3'	*loxP-Pac*I insertion step3 sn
5'CCAAGCTGTGCCGCCACACACGGTTCTAGATAGGCAGAGCCTTT AATTAA**ataacttcgtataatgtatgctatacgaagttat**CCGGCTTCTGACAAGCCTAC CTTAATTGTTTCGTATGTGTC-3'	*loxP-Pac*I insertion step3 asn
5'-GCCAGTACTAGTGAACCTCTTCGAGGGACCTAATTAAGGGTTCC GGATCTCGAGCCCCAGCTGG-3'	*loxP-neo* deletion step4 sn
5'-CCAGCTGGGGCTCGAGATCCGGAACCCTTAATTAGGTCCCTCGA AGAGGTTCACTAGTACTGGC-3'	*loxP-neo* deletion step4 asn
RNA Interference (RNAi) experiments: C1218T > silent mutation	
5'-GATCCGCTACCTGAC**T**TTCTTCCACAACTAC-3'	hTRPML1 sn
5'GTAGTTGTGGAAGAA**A**GTCAGGTAGCGGATC-3'	hTRPML1 asn
Dominant negative variant D458K of hTRPML3	
5'-TCTCTGATAAATGGA**AA**G**G**ATATGTTTGCCAC-3'	hTRPML3 sn
5'-GTGGCAAACATATC**C**T**T**TCCATTTATCAGAGA-3'	hTRPML3 asn
C-terminal LTS deletion of hTRPML1	
5'-CGGAAGGGACCCCTCGGTGAATAAGGGCAATTC-3'	hTRPML1 sn
5'-GAATTGCCCTTATTCACCGAGGGGTCCCTTCCG-3'	hTRPML1 asn
Deaf-waddler mutation G283S	
5'-GGTGTCAACTCTCAAACT**A**GCATCATATTTACCCTGC-3'	rPMCA2 sn
5'-GCAGGGTAAATATGATGC**T**AGTTTGAGAGTTGACACC-3'	rPMCA2 asn
Varitint-waddler mutation A419P	
5'-GGTTCTGTTGCTGCC**C**TGCTATGATCTATC-3'	mTRPML3 sn
5'-GATAGATCATAGCA**G**GGCAGCAACAGAACC-3'	mTRPML3 asn
Varitint-waddler mutation I362T	
5'-GTTCTGAAAATGGAAA**C**CCAAGCCAAGAGTC-3'	mTRPML3 sn
5'-GACTCTTGGCTTGG**G**TTTCCATTTTCAGAAC-3'	mTRPML3 asn

Table 3: Sequences of synthetic oligonucleotides used for RT-PCR. Abbreviations: sn = sense, asn = antisense.

Murine culture cells, tissues or organs		
5'-CAGAGCCTCATCAACAATGAG -3'	mTRPML1 sn	
5'-GTCAGGTAGCGAATGACACCG -3'	mTRPML1 asn	470 bp
5'-CAGAATACGATTACCTTCGAC-3'	mTRPML2 sn	
5'-GAGCACGTTGTACGTCTGAAAG-3'	mTRPML2 asn	500 bp
5'-CAAGGCTCACAGTGGAAGAATCAA-3'	mTRPML3 sn	
5'-CAGCGCAGCAACAGAACCTCAT-3'	mTRPML3 asn	550 bp
5'-AACGGGAAGCCCATCACCATCTT-3'	mGAPDH sn	
5'-CAGCCTTGGCAGCACCAGTGG-3'	mGAPDH asn	442 bp
Human culture cells, tissues or organs		
5'-TCCTCTGCGCCCGCTCACTCC-3'	hTRPML1 sn	
5'-CATGGCGGCGAACGTCACAAACA-3'	hTRPML1 asn	500 bp
5'-AAGCTCACAGTGGCAAAATCAAAATC-3'	hTRPML2 sn	
5'-CAACCCAAACCAAGAGCGTAGAG-3'	hTRPML2 asn	411 bp
5'-GCTCGTGTGGCTTGGAGTCATC-3'	hTRPML3 sn	
5'-TGGAGGGTCATCTTCTAATCTGTAT-3'	hTRPML3 asn	487 bp
5'-AATGGAAATCCCATCACC-3'	hGAPDH sn	
5'-CACAGCCTTGGCAGCGCCAG-3'	hGAPDH asn	444 bp
conditional *Trpml3* knockout analysis		
5'-CGTTCCCTGAACAGGGTCTCCGAG-3'	RT-1 sn	
5'-ATTGTTTCGTATGTGTCTGTGATG-3'	RT-1 asn	200 bp
5'-CAAGGCTCACAGTGGAAGAATCAA-3'	RT-2 sn	
5'-CAGCGCAGCAACAGAACCTCAT-3'	RT-2 asn	512 bp
5'-ACTACCAGCAAGATGGCTTCCCAG-3'	RT-3 sn	
5'-TCAGCCACACACTGTATTTTCCTC-3'	RT-3 asn	181 bp
5'-ATGAGGTTCTGTTGCTGCGCTG-3'	RT-4 sn	
5'-TCAGCCACACACTGTATTTTCCTC-3'	RT-4 asn	473 / 266 bp

Table 4: Sequences of synthetic oligonucleotides used for genotyping. Abbreviations: sn = sense, asn = antisense, LA = left arm, RA= right arm, exc = excision, *neoR* = neomycin resistance, E11 = exon 11 and intron, Dfw = deaf-waddler, *Va* = varitint-waddler, seq = sequencing.

ES cell screening after neomycin selection		
5'-CACCTCACTTCCTGTTTCATAG-3'	LA sn	
5'-GCTGGGGATGCGGTGGGCTCTATGGCT-3'	LA asn	3280 bp
5'-ACTTCGTTCTAGTGAACCTCTTCGAGG-3'	RA sn	
5'-GCATGTGCACATGTGTAGAG-3'	RA asn	3298 bp
ES cell screening after Flp recombination, Chimera, Founder & knockin		
5'-GAACACACTGACTACCCCCAA-3'	lox sn	
5'-TACAGTTTTACAGATGTGTTTGAGT-3'	lox asn	471 / 309 bp
5'-GAACACACTGACTACCCCCAA-3'	neo sn	
5'-AGAGGTTCACTAGAACGAAGTTCCTATTCC-3'	neo asn	2116 / 374 bp
5'-CACCTCACTTCCTGTTTCATAG-3'	LA sn	
5'-TTCACTAGAACGAAGTTCCTATTCC-3'	LA (2) asn	3176 bp
5'-ACTTCGTTCTAGTGAACCTCTTCGAGG-3'	RA sn	
5'-GCATGTGCACATGTGTAGAG-3'	RA asn	3298 bp
genetic *Trpml3* inactivation after Cre recombination		

5’-GAACACACTGACTACCCCCAA-3’	exc sn	
5’-ACTCCTAGGCTGCCTATAACCC-3’	exc asn	1952 / 993 bp
5’-ACTTCGTTCTAGTGAACCTCTTCGAGG-3’	RA sn	
5’-GCATGTGCACATGTGTAGAG-3’	RA asn	2340 bp
***Cre* locus**		
5'-AGGCTAAGTGCCTTCTCTACAC-3'	Cre1 sn	
5'-ACCAGGTTCGTTCACGCATGG-3'	Cre1 asn	210 bp
5'-AGCGATCGCTGCCAGGAT-3'	Cre2 sn	
5'-ACCAGCGTTTTCGTTCTGCC-3'	Cre2 asn	158 bp
***Trpml3* ES cells, knockin & knockout sequencing**		
5’-GAACACACTGACTACCCCCAA-3’	seq sn 1 (LA)	
5’-GATGAGCTTCAAGGTGAGATGAG-3’	seq sn 2 (E11)	
5’-TATGTAGCTTGAAAAGGC-3’	seq sn 3 (RA)	
5’-CACCTCACTTCCTGTTTCATAG-3’	seq sn 4 (5’genome)	
5'-GAACACACTGACTACCCCCAA-3’	seq sn 5 (LA)	
5’-TGAAGCGTGCAGAATGCCGG-3’	seq sn 6 (*neo*^{R})	
5’-CTGGCACGTGTGAGGCAATC-3’	seq sn 7 (E11)	
5’-GCAGAAGAGTTACCTGGTGTG-3’	seq sn 8 (E11)	
5'-TATCCTATAAACTGGAGCAGA-3’	seq asn 1 (LA)	
5’-CTCATCTCACCTTGAACTCATC-3’	seq asn 2 (E11)	
5’-GATTGCCTCACACGTGCCAG-3’	seq asn 3 (E11)	
5’-GCTGGGGATGCGGTGGGCTCTATGGCT-3’	seq asn 4 (*neo*^{R})	
5’-ACTCCTAGGCTGCCTATAACCCCAT-3’	seq asn 5 (RA)	
5’-GCATGTGCACACATGTGTAGAG-3’	seq asn 6 (3’genome)	
Deaf-waddler mice		
5’-GTAACCGGGTTATACCTTCCTCAG-3’	Dfw sn	
5’-AAATGTGTGTGTGTAGGAGGCTTA-3’	Dfw asn	180 bp
5’-ACCCATGTGATGGAGGGCTCAGGA-3’	Dfw seq sn	
Varitint-waddler mice		
5’-TCTCACAAGCTATGATGTCTGCAG-3’	*Va* sn	
5’-CTGAAACTGTGAGCCAGCCCCAGT-3’	*Va* asn	400 bp
5’-GATACCTGGGTTTCTTTGCGAAGT-3’	*Va* seq sn	

2.1.9. Cell lines and primary culture

Human embryonic kidney 293 cells (HEK293 cells) and NIH 3T3 cells were purchased from ATCC (3). Primary normal neonatal human epidermal melanocytes (NHEM) were kindly provided by Dr. Paul Khavari (Stanford University, School of Medicine, Department of Dermatology, Stanford, CA, USA).

2.1.10. Mouse lines

FVB/NJ wild-type mice (stock number 001800), homozygous deaf-waddler mice C3H/HeJ-Atp2b2^{dfw}/J (stock number 001276), CH3/HeJ wild-type mice (stock number 000659), and heterozygous varitint-waddler (*Va*) mice (RSV/LeJ, stock number 000268) were obtained from The Jackson Laboratory (39). C57BL/6J wild-type mice were purchased from Stanford University, Department of Comparative Medicine (In-house breeding colony). Heterozygous *Foxg1*^{Cre} mice were kindly provided by Dr. Susan K. McConnell (Stanford University, School of Medicine, Department of Biology, Stanford, CA, USA), homozygous *Math1-CreER*^{TM} by Dr. Suzanne J. Baker (Developmental Neurobiology, St. Jude Children's Research Hospital, Memphis, TN, USA), and heterozygous *Hprt*^{Cre} by Dr. Mark Krasnow (Stanford University, School of Medicine, Department of Biochemistry, Stanford, CA, USA). Animal studies were conducted in accordance with protocols approved by the Administrative Panel on Laboratory Animal Care at Stanford University. The protocol number is #11961.

2.1.11. Antibodies and dilutions

Table 5: List of antibodies used.

Name	Antigen	Resources	Host	Concentration	Vendor
JL-8	GFP variants	monoclonal	mouse	1:1000	Clontech
HA	HA-tag	monoclonal	rabbit	1:1000	Sigma
PV3	Parvalbumin 3	polyclonal	rabbit	1:3000	Heller Laboratory
Calret	Calretinin	polyclonal	rabbit	1:1000	Chemicon
Mcoln3	TRPML3	polyclonal	rabbit	1:300 - 1:3000	Osenses
Mcoln3	TRPML3 C-terminal	polyclonal	rabbit	1:200 - 1:1000	Sigma
Mcoln3	TRPML3 N-terminal	polyclonal	rabbit	1:200 - 1:1000	Sigma
9E10	c-Myc-tag	polyclonal	mouse	1:50 - 1:500	Santa Cruz
CH-19	pan-Cadherin	monoclonal	mouse	1:500	abcam

For immunohistochemistry TRITC-conjugated goat anti-rabbit antibody (32), TRITC-conjugated goat anti-mouse IgG1 antibody (32), and FITC-conjugated phalloidin (34) were used as secondary antibodies. Proteins in Western blot experiments were visualized with IRDdye 680- and IRDdye 680-conjugated secondary antibodies (32).

2.2. Methods

2.2.1. Biomolecular methods

2.2.1.1. Polymerase Chain Reaction (PCR)

The polymerase chain reaction is a widely used method to amplify DNA regions of known sequence. The reaction mixture contains target DNA, two oligonucleotides (sense [sn] and antisense [asn]), deoxyribonucleotides (dNTPs), and heat-stable polymerase. The PCR consists of a series of 25-35 repeated temperature changes called cycles and each cycle consists of three discrete temperature steps. The first step involves the denaturation of the double-stranded DNA at 95°C for 30 sec. The reaction temperature is lowered for 30 sec allowing the DNA oligonucleotides to hybridize to complementary sequence in the two DNA strands. The annealing temperature (T_A) chosen for the PCR depends on the length and composition of oligonucleotides. The following rule was complied: 4x(GC)+2x(AT) - 10 = T_A. In the next step, the DNA polymerase binds and adds dNTPs that are complementary to the template in 5' to 3' direction at the free 3'OH end of each primer. The temperature of the elongation step depends on the used DNA polymerase. The Taq DNA polymerase has its optimum at 72°C. The DNA polymerase will polymerize 1000 bases per minute. A final elongation step is performed at 72°C for 10 min to ensure that any remaining single-stranded DNA is fully extended. For different approaches, specific enzymes were used. *Pfu* DNA polymerase (38) was used for high fidelity, otherwise Go-Taq Master-Mix provided by Promega (30), containing Taq polymerase without proofreading (30) was used. Phusion DNA polymerase (14) was used for DNA fragments longer than 3000 bp.

Reaction components:

Target DNA	10 ng/50 µl reaction or 50-250 ng/50 µl genomic DNA
Buffer	variable
Oligonucleotides A/B	0.1-1 µM each
dNTPs	200 µM each
DMSO	10-20% if GC rich template
Enzyme	1.25 U/50 µl reaction
Nuclease free water	to a final volume

2.2.1.2. Mutagenesis

In vitro site-directed mutagenesis is a technique in which a mutation (point mutation, deletion, or insertion) is created at a defined site in the DNA molecule with the aim to introduce a change in the DNA sequence and, as a consequence, in the protein structure and function. The QuikChange site-directed mutagenesis kit was used (38). The method utilizes double-stranded plasmid DNA with an insert of interest and the two complementary oligonucleotides containing the desired mutation, which is flanked by at least 10 unmodified bases of sequence in both directions. Sequences of synthetic oligonucleotides used for introducing the mutations are summarized in Table 2. In a temperature cycling, *PfuTurbo* DNA polymerase, a high fidelity enzyme, replicates both plasmid strands and incorporates the mutagenic oligonucleotides, resulting in nicked circular strands. For a single reaction 50 ng DNA template, 5 µl of reaction buffer, 125 ng of oligonucleotide each, 1 µl dNTP mix, 1 µl *PfuTurbo* DNA polymerase (2.5 U/µl), and sterile, nuclease free water to 50 µl were combined. Following cycling parameter for the mutagenesis methods was used:

step 1	95°C	1 min
step 2*	95°C	30 sec
	52°C	1 min
	68°C	1 min/kb of plasmid length

* 12 to 18 cycles, depending on type of desired mutation (12: point mutation, 16: single amino acid changes, 18: multiple amino acid deletion or insertion)

In the next step, the product was treated with the *Dpn*I endonuclease at 37°C for 1 h. *Dpn*I recognizes methylated and hemimethylated DNA (target sequence: 5'-Gm^{6}ATC-3'). Plasmid DNA isolated from almost all *E.coli* strains is methylated. Therefore, *Dpn*I was used to digest the nonmutated parental DNA template and to select for mutation-containing synthesized DNA. 1 µl of the *Dpn*I-treated DNA was transformed into 50 µl XL1-Blue supercompetent cells. The procedure of transformation is described in chapter 2.2.1.8. Mutants were verified by sequencing both strands entirely.

2.2.1.3. RNA isolation and Reverse Transcriptase PCR (RT-PCR)

Reverse transcription polymerase chain reaction (RT-PCR) is a sensitive technique for mRNA detection.

2.2.1.3.1. RNA isolation

Collected tissues or cells were transferred into RNase free tubes and either immediately frozen in liquid nitrogen and stored at -80°C or further processed to RNA. Total RNA was isolated from collected animal tissues or cultivated cells with the RNeasy Mini-Kit (29). The RNA isolation was performed according to manufacturers' instructions. RNA was either stored at -80°C or immediately used for RT-PCR.

2.2.1.3.2. RT-PCR principles and procedure

No RNA isolation method consistently produces RNA free of residual genomic DNA. To remove genomic DNA prior RT-PCR, recombinant DNaseI (RNase-free) (31) was added to approximately 5 µg RNA and incubated at 37°C for 30 min, followed by a heat-inactivation step at 72°C for 20 min. RT-PCR includes several steps. First, the RNA strand is reverse transcribed into its complementary DNA (cDNA) using a reverse transcriptase (SuperScript™ III Reverse Transcriptase (18)). For a single reaction 500 ng RNA, 1 µl of Oligo(dT)$_{18}$ (13), 1 µl 10 mM dNTP mix (10 mM each dATP, dGTP, dCTP, and dTTP) (13) and sterile, distilled water to 13 µl were combined. The mixture was incubated for 5 min at 65°C and cooled down to room temperature (approximately 5 min) to allow oligonucleotides to anneal. After adding buffer, DTT (dithiothreitol), RNase inhibitor (18), and reverse transcriptase, the reaction was incubated at 25°C for 5 min, then at 42°C for 60 min, and at 55°C for 50 min. Thereafter the enzyme was inactivated at 70°C for 15 min. Controls (no reverse transcriptase) were always prepared to detect genomic DNA contamination. In a final step, the polymerase chain reaction is used to amplify the genes of interest. GAPDH (glyceraldehyde-3-phosphate dehydrogenase), a housekeeping gene (either murine or human) was used as internal control. The respective procedure was described above (2.2.1.1.). Oligonucleotides specific for cDNA were designed in two ways. First, oligonucleotides were spanning the exon-exon junction. One-half of its sequence will hybridize to the 3' end of one exon and the other half to the 5' end of the adjacent exon. This oligonucleotide will preferentially anneal to cDNA synthesized from spliced mRNA, but is not likely to anneal with genomic DNA. Second, RT-PCR

oligonucleotides were designed to flank a region that contains at least one intron. The amplified products from cDNA (no introns) will be smaller than those amplified from genomic DNA (containing introns). The size difference in products is used to detect the presence of contaminating DNA. The oligonucleotides used for RT-PCR are summarized in Table 3.

2.2.1.4. Genotyping and isolation of genomic DNA

2.2.1.4.1. Preparation of genomic DNA from Embryonic Stem (ES) cells grown on 96-well tissue culture dishes

ES cells were lysed with 50 µl lysis buffer per well containing 10 mM Tris pH 7.5, 10 mM EDTA, 10 mM NaCl, and 0.5% Sarkosyl (w/v). Proteinase K (42) was always freshly added. The plates were incubated at 55°C over night in a humid chamber. To precipitate DNA 100 µl out of a mixture of 100 µl absolute ice-cold EtOH and 1.5 µl NaCl was added and incubated for 30 min at room temperature. After centrifugation for 10 min at 4°C at 2000 rpm, the DNA pellets were washed three times with 100 µl 70% EtOH. The DNA was centrifuged for 5 min at 4°C at 2000 rpm between each washing step. After the last wash, the DNA was air dried and resuspended with 30 µl TE buffer in the CO_2 incubator at least 24 hours. Two µl of genomic DNA was used for the PCR reaction.

2.2.1.4.2. Isolation of genomic DNA from mouse tails

A small sample of tissue was collected for transgenic detection. These samples are the source of preparing DNA, which is used in PCR. Great care was taken when cleaning tools between samples to avoid risk of carryover contamination. Generally, the tail excision was performed on mice between P0 and P14 of age, because younger mice heal faster and bleed less. If genomic DNA with high quality and purity was needed, e.g. to cycle large PCR fragments (>3000 bp), the DNeasy Blood & Tissue Kit (29) was used for isolation of genomic DNA. Otherwise, DirectPCR DNA extraction reagent (42) was used. Both isolation methods were processed according to manufacturers' instructions.

2.2.1.4.3. PCR of genomic DNA fragments

After the DNA template was prepared, a standard PCR was performed (see 2.2.1.1.). Go-Taq Master-Mix (30) was used for amplification of PCR fragments <3000 bp, whereas high-fidelity Phusion DNA polymerase (14) was used for PCR fragments >3000 bp. The

sequences of synthetic oligonucleotides used for PCR reactions are summarized in Table 4. Varitint-waddler and deaf-waddler mutant mice were genotyped by sequence analysis. Genomic DNA fragments of *Trpml3* (varitint-waddler) and *Atp2b2* (deaf-waddler) were amplified, gel-purified and sequenced. DNA sequence changes take place at position 1255 (G → C) of *Trpml3* and at position 847 (G → A) of *Atp2b2*. Genomic DNA of *Trpml3* knockin ES cells and mice, and *Trpml3* inactivation in mice were sequenced to ensure the presence of FRT and *loxP* recombination sites, and to ensure the right integration into the mouse genome. The oligonucleotides used for PCR of genomic DNA fragments are summarized in Table 4.

2.2.1.5. Induction of Cre activity with tamoxifen in mice

Tamoxifen (34) was dissolved in prewarmed sterile corn oil (34) at a concentration of 1 mg/ml or 3 mg/ml. To get tamoxifen in solution, the mix was sonicated for 10 min. Tamoxifen was always freshly prepared. Tamoxifen is sensitive to ultraviolet light; therefore, it was prepared and stored in the dark. A 26-gauge needle insulin syringe was used for intraperitoneal injections in pups between P0 and P3. The dose administration varied from 3 to 4 mg/40 g body weight. Three injections in the same mouse were separated by 24 hours.

2.2.1.6. Manipulation of nucleic acids

2.2.1.6.1. DNA Restriction

An important tool for cloning is the restriction of DNA. Restriction endonucleases are enzymes that cut DNA at specific recognition nucleotide sequences known as restriction sites. All restriction endonucleases were purchased from New England Biolabs (26). The following components were combined and incubated for 1-3 hours at the recommended temperature:

DNA	0.1-4 µg
10x digest buffer	2 µl in 20 µl reaction volume
Enzyme	1-5 U/µg DNA (The maximum volume an enzyme can be used is 1/10 of the total reaction volume.)

2.2.1.6.2. Dephosphorylation

Alkaline Phosphatase, Calf Intestinal (CIP) (26) catalyzes the removal of 5'-phosphate groups from DNA, RNA, ribo- and deoxyribonucleoside triphosphates. Since CIP-treated fragments lack the 5'-phosphoryl termini required by ligases, they cannot self-ligate. This property was used to decrease the vector background in cloning strategies. For a single reaction 0.5-1 µg DNA, 1x buffer, 2.5 U/µg CIP, and nuclease free water to 20 µl were combined and incubated for 30 min at 37°C. Afterwards, the DNA was gel purified (see 2.2.1.7.3.).

2.2.1.6.3. DNA Ligation

The enzyme used to ligate DNA fragments is T4 DNA ligase (30), which originates from the T4 bacteriophage. This enzyme joins the 5'-phosphate and the 3'-hydroxyl groups of double stranded DNA molecules. For a successful reaction, insertion DNA was used in excess of vector DNA (3:1). Together with buffer and 1 µl of T4 DNA ligase (3U), the reaction was incubated at room temperature for 2 hours (sticky ends) or at 16°C over night (blunt ends).

2.2.1.7. Analysis of nucleic acids

2.2.1.7.1. Quantification and purity of nucleic acids

Absorbance measurements were made on the Thermo Scientific NanoDrop™ 1000 Spectrophotometer to determine the concentration and purity of nucleic acids in solution. The sample (RNA or DNA) is exposed to ultraviolet light at 260 nm. The more light is absorbed by the sample, the higher the nucleic acid concentration. The ratio of absorbance at 260 nm and 280 nm was used to assess the purity of DNA and RNA. A ratio of 1.8 was accepted as "pure" for DNA, and a ratio of 2.0 was accepted as "pure" for RNA. If the ratio was lower in either case, it indicated the presence of protein or other contaminants that absorb strongly at or near 280 nm. In these cases, an ethanol precipitation is recommended to purify the sample.

2.2.1.7.2. Agarose Gelelectrophoresis

Agarose gelelectrophoresis is a method to separate DNA or RNA molecules by size in an electrical field. Shorter molecules move faster and migrate farther than longer ones. Depending on the size of the DNA fragments, 0.8-2% horizontal agarose gels were used.

Non-toxic SYBR Safe DNA stain (18) was added to the agarose to visualize the DNA or RNA. It fluoresces under UV light when intercalated into DNA or RNA. Since the stained DNA is not visible in natural light, DNA was mixed with Orange DNA Loading Dye (13). This solution contains two dyes, orange G (migrates with ~50 bp DNA fragments) and xylene cyanol FF (which migrates with ~4000 bp DNA fragments) for visual tracking of DNA migration during electrophoresis. For sizing of DNA fragments a 1 kb DNA Ladder (13) was always loaded next to the samples. The agarose gel was placed into a horizontal electrophoresis chamber filled with 1x TBE buffer (89 mM Tris base, 89 mM Boric acid, 2 mM EDTA, pH 8). The gels were running at constant 120 V, then analyzed, and captured under UV light using a Kodak Gel Logic 2200 Imaging system.

2.2.1.7.3. Isolation of DNA fragments from agarose gels

The QIAGEN Gel extraction kits (29) were used to extract and purify DNA of 70 bp to 10000 bp from agarose gels. The isolation of DNA fragments from the agarose gel was performed according to manufacturers' instructions.

2.2.1.7.4. DNA sequencing

DNA sequencing is the determination of the precise sequence of nucleotides in a sample of DNA. DNA samples were sent to the dye-terminator sequencing service Genewiz, Inc., South Plainfield, NJ, USA. The pre-mix was containing 25 pmol of sequence specific oligonucleotides (5 µl) and DNA template (10 µl). The total mass of DNA template was depending on the DNA type, plasmid or purified PCR product and DNA length:

DNA type:	**DNA template length:**	**DNA template total mass:**
Plasmids:	<6 kb	500 ng
	6-10 kb	800 ng
	>10 kb	1000 ng
Purified PCR products:	<0.5 kb	10 ng
	0.5-1 kb	20 ng
	1-2 kb	40 ng
	2-4 kb	60 ng

The analysis of traces was done with Lasergene 8 software (DNAstar Inc).

2.2.1.8. Transformation of Plasmid DNA

Transformation of plasmid DNA into bacteria (DH5α strain of *E. coli*) using the heat shock protocol is a basic technique of molecular biology. To 50 µl competent cells usually 5-10 µl of a standard ligation or approximately 10 ng of plasmid DNA was added and incubated for 10 min on ice. The uptake of DNA into bacteria occurred by heat shock for 1-2 min at 42°C. Afterwards the mix was placed back on ice for couple of minutes. Then 250 to 550 µl non-selective liquid LB media was added and incubated in a 37°C shaker incubator (200 rpm) for 1 hour. 100 µl and the rest of the bacteria culture was plated onto LB agar plates with appropriate selection antibiotic and resistant clones (colonies) were grown in a 37°C incubator overnight.

2.2.1.9. DNA Plasmid preparation

For isolation of plasmid DNA the following kits were used:
GeneJet™ Plasmid Miniprep Kit (13)
HighSpeed Plasmid Maxi Kit (29)
EndoFree Plasmid Maxi Kit (29)
The DNA isolation was performed according to manufacturers' instructions.

2.2.2. Mammalian cell culture

2.2.2.1. Cell culture and cell transfection

All cultured cells were grown and maintained in a standard humidified 37°C incubator, with 95% air and 5% CO_2. HEK293 and NIH 3T3 cells were maintained in DMEM (25), supplemented with 10% fetal bovine serum (27), and 100 µg/ml penicillin and streptomycin (25). Medium change was done every other day until cells were confluent. The cell growth was monitored every day with a phase-contrast microscope. After the cells reached 95-100% confluence, they were passaged, which was initiated by washing them with PBS and enzymatically treatment with 0.25% Trypsin-EDTA solution (25). Primary cells were treated with 0.05% Trypsin-EDTA solution (25). The cells were placed at 37°C to facilitate the enzymatic reaction (usually 3-5 min). Trypsin activity was blocked by adding media containing serum and the cells were separated by mild trituration using a 10 ml plastic pipette. After the cells were collected by centrifugation for 3 min at room temperature at 800 rpm, the cell pellet was resuspended in culture medium. An appropriate aliquot of the cell suspension was added to new culture vessels and to dishes prepared for

experiments (1×10^3 to 1×10^6 cells/cm^2). For calcium imaging, electrophysiological experiments, immunocytochemistry, or Western blotting, all plasmid constructs were transiently expressed in cells with the use of Genejammer (38) and analyzed 1 to 2 days after transfection. In general, for one gene transfection (e.g. for one 10 cm culture dish) 1 µg plasmid DNA was used and mixed with 10 µl Genejammer solution and combined with culture medium to 100 µl. Expression vectors were based on pcDNA3.1 (18) (see 2.1.6.1.). Transfected cells were analyzed 24 hours after transfection. Neonatal human epidermal melanocytes were cultured in medium 254 supplemented with HMGS (18). Using the Amaxa Nucleofector (NHEM-Neo Nucleofector Kit (23), program U-016), 5×10^5 cells were transfected with 5 µg of endotoxin free plasmid DNA. After 2 or 3 days after nucleofection, the cells were used for experiments.

2.2.2.2. Generation of stable HEK293 cell lines

The pcDNA3.1 vectors contain the neomycin resistance gene for selection of stable cell lines conferring resistance to geneticin (G418) (21). For more pcDNA3.1 features please see 2.1.6.1. HEK293 cells expressing human or mouse TRPML3 and *danio rerio* TRPN1 (as YFP-fusion proteins) were selected using G418 at a final concentration of 0.8 mg/ml. This amount of G418, which was determined in dose-response pilot experiments, was required to kill cells not expressing the construct TRPML3 or TRPN1 (coexpressing the selection gene). The cells were grown in selective medium, which was renewed every 2 days until geneticin-resistant foci were identified. Colonies were picked and expanded in 96-well plates. The cell clones were subcloned twice to ensure the stable expression of TRPN1 or TRPML3, which was confirmed by fluorescence microscopy and Western blotting. Cell lines with abnormal morphology, expression level (too weak or too strong), and stability were eliminated. The generated stable cell lines were expanded and frozen in aliquots of about 50 to ensure identical and early passage numbers.

2.2.3. Biochemical methods

2.2.3.1. Immunofluorescence

2.2.3.1.1. Whole-mount immunohistochemistry

Organs of Corti and utricles were fixed with fresh 4% paraformaldehyde in PBS (137 mM NaCl, 2.7 mM KCl, 10 mM Na_2HPO_4, and 2 mM KH_2PO_4) for 1 hour. If animals were older than P21 and the whole length of the organ of Corti was needed, the otic capsule was decalcified with Ethylenediaminetetraacetic acid (EDTA) (0.5 M, pH 8.0) over night at 4°C before dissection. Then the tissue was permeabilized and blocked for 1 hour in PBT-1 (0.1% Triton X-100, 1% BSA (w/v), 5% heat-inactivated goat serum (w/v) in PBS). All steps were performed at room temperature unless otherwise indicated. After incubation overnight at 4ºC with diluted antibodies (see 2.1.4.), samples were washed three times with PBT-1 and twice with PBT-2 (0.1% TritonX-100, 0.01% BSA (w/v)). Secondary antibodies (see 2.1.4.) were diluted in PBT-2 and incubated for 1 hour. After washing three times with PBT-2 and twice with PBS, the samples were mounted in PBS/Glycerol (1:1) and imaged either in epifluorescence or in confocal mode (LSM Pascal, Zeiss, Jena, Germany).

2.2.3.1.2. Immunocytochemistry on cultured cells

The cells were washed for 5 min with PBS buffer (137 mM NaCl, 2.7 mM KCl, 10 mM Na_2HPO_4, and 2 mM KH_2PO_4) and fixed for 15 min with 4% paraformaldehyde in PBS or with ice-cold Methanol for 3 min. After two washing steps with PBS, the cells were permeabilized and blocked for 20 min with PBT-1 (0.1% Triton X-100, 1% BSA, 5% heat-inactivated goat serum in PBS). The antibodies diluted in PBT-1 were incubated on cells either over night at 4°C or 1 hour at room temperature. The antibodies and dilutions used are summarized in Table 5 (2.1.11). Cells were incubated with secondary antibody diluted in PBT-2 for 1 hour. After washing once with PBT-2 and three times with PBS, the samples were mounted in PBS/Glycerol (1:1) and imaged with a confocal microscope (LSM Pascal, Zeiss, Jena, Germany).

2.2.3.1.3. Annexin V staining

One of the earliest indications of apoptosis is the translocation of the membrane phospholipid phosphatidylserine from the inner to the outer leaflet of the plasma membrane, the binding site for annexin V (Tait and Gibson, 1992; Meers and Mealy,

1993). HEK293 cells were directly grown on glass coverslips and transfected with plasmid DNA encoding wild-type or mutant channels. After 10, 15, 20, and 25 hours, the cells were briefly washed once with PBS (137 mM NaCl, 2.7 mM KCl, 10 mM Na_2HPO_4, and 2 mM KH_2PO_4) and then exposed to Cy5-conjugated annexin V binding buffer (4), incubated at room temperature for 5 min in the dark, washed with PBS for 5 min, and analyzed using confocal microscopy.

2.2.3.2. Preparation of proteins and Western blot analysis

Transfected HEK293 (growing in 10 cm culture dishes) cells were analyzed 24 hours after transfection. The cells were washed with ice-cold PBS (137 mM NaCl, 2.7 mM KCl, 10 mM Na_2HPO_4, and 2 mM KH_2PO_4) containing 1 mM PMFS (34) and protease inhibitor mix (34). Cells were scraped off and centrifuged at 800 rpm for 3 min at 4ºC. After centrifugation, the pellet was solubilized in 700 µl ice-cold lysis buffer containing 50 mM Tris/HCl pH 7.5, 1 mM EDTA, 150 mM NaCl, 1% Triton X-100, 1 mM PMFS, and protease inhibitor mix and incubated for 1.5 hours at 4ºC in an overhead rotor. Additional, the lysis was enhanced by triturating the cell suspension through a 26-gauge needle. After centrifugation at full speed for 60 min at 4ºC a sample of the supernatant, containing soluble proteins and other molecules, was taken for quantification of total protein using the Pierce BCA (bicinchoninic acid) Protein Assay Kit (40). All samples were then processed for Western blot analysis by adding NuPAGE LDS sample buffer (40% glycerol, 4% lithium dodecyl sulfate (LDS), 0.8 M triethanolamine-Cl pH 7.6, 4% Ficoll-400, 0.025% phenol red, 0.025% coomassie G250, and 2 mM EDTA disodium) and reducing agent Dirhiothreitol (DTT) (18) and boiling for 10 min. After a short centrifugation at full speed, the samples were loaded onto 4-12% Bis-Tris gel (18) with MOPS SDS running buffer (2.5 mM MOPS, 2.5 mM Tris base, 0.005% SDS, and 0.05 mM EDTA, pH 7.7). The gels were running at constant 180 V. Proteins were transferred from gel to Nitrocellulose membrane by semi-dry electrophoresis (5) (Protein Transfer Buffer: 1.25 mM Bicine, 1.25 mM Bis Tris (free base), 0.05 mM EDTA, pH 7.2, and 20% Methanol). Western blots were then incubated for 1 hour at room temperature in 2.5% Liquid Block (32) in PBS. The blots were then incubated over night at 4ºC with antiserum diluted in 2.5% Liquid Block and 0.1% Tween 20 in PBS (PBS-T). Antiserum dilutions were used as described in 2.1.11. The blots were washed 3 times for 5 min each at room temperature with PBS-T. Detection was performed with IRDye 680- and IRDye 800-conjugated secondary antibodies (32) diluted in 2.5% Liquid Block and PBS-T

(1:5000 dilution) for 1 hour at room temperature. Then the blots were washed 3 times for 5 min each at room temperature with PBS-T and scanned with the Odyssey infrared imaging system (22).

2.2.4. Calcium imaging

2.2.4.1. Basic principles

The most commonly used structure for calcium specific binding is 1,2-bis(2-aminophenoxy)ethane-N,N,N',N'-tetraacetic acid (BAPTA). The multiple anionic carboxyl groups bind the divalent calcium ion in a similar fashion as the calcium specific chelator, EGTA (ethylene glycol-bis(ß-aminoethylether)-N,N,N',N'-tetraacetic acid). The calcium ion sensitive fura-2 dye (18) is derived from EGTA, which was used in our experiments (Grynkiewicz et al., 1985). The cell-permeable form of fura-2 has five carboxylate groups, which have been derivatized as acetoxymethyl esters (= fura-2-AM). Once inside the cell, these molecules are hydrolyzed by intracellular esterase, whereat formaldehyde and acetate are being formed as byproducts leading to a cell-impermeant indicator. Because the AMs have low aqueous solubility, some dispersing agent such as Pluronic F-127 (34) was used to facilitate cell loading. One of the most important problems in the use of fura-2-AM is compartmentalization. Fura-2 is known to accumulate in mitochondria of endothelial cells, and lysosomes of fibroblasts. The degree of compartmentalization is dependent on numerous factors (e.g. cell type, loading concentration, or incubation time). The concentration of the indicator dye has to be kept as low as possible (approximately 4 μM for fura-2-AM). A high concentration leads to an oversaturation of cytosolic esterase, which allows the indicator to cross organelle membranes into the intracellular compartments with the consequence of inhomogeneous dispersal (Takahashi et al., 1999). Optimal incubation time varies depending on cell type and has to be experimentally determined. HEK293 cells were incubated for 50 min, whereas NIH 3T3 and NHEM for only 30 min at 37°C.

The application of fura-2 to measure $[Ca^{2+}]_i$ is based on fluorescence excitation maximum shifts from 363 nm for Ca^{2+}-free chelator to about 335 nm for the Ca^{2+}-bound, while the fluorescence emission maximum is relatively unchanged at 510 nm. The largest dynamic range for Ca^{2+}-dependent fluorescence signals is obtained by using excitation at 340 nm and 380 nm (Takahashi et al., 1999). The fluorescence emission during excitation at 380 nm (F_{380}) decreases upon binding of Ca^{2+} whereas the fluorescence emitted during excitation at 340 nm (F_{340}) increases. Thus, the ratio F_{340}/F_{380} obtained by dividing the

fluorescence emitted during excitation at 340 nm by that emitted during excitation at 380 nm changes in the same direction as $[Ca^{2+}]_i$. The quotient F_{340}/F_{380} is independent of dye concentration in the cell, cell thickness, intensity of excitation, dye leakage, photobleaching, and alignment of the measurement system (Grynkiewicz et al., 1985). This principle is also called ratiometric measurement.

2.2.4.2. Measuring equipment

Measurements of $[Ca^{2+}]_i$ with the fluorescent indicator fura-2-AM were performed using a monochromatic-based imaging system (iMIC platform and Polychrome V monochromator, TILL Photonics GmbH).

2.2.4.3. Measurement conditions for calcium imaging experiments

HEK293, NIH 3T3, and NHEM cells were loaded with approximately 4 µM fura-2-AM (18) (dissolved in DMSO and 0.005% Pluronic F-127 (34)) in a standard bath solution (SBS) containing 138 mM NaCl, 6 mM KCl, 2 mM $MgCl_2$, 2 mM $CaCl_2$, 10 mM HEPES, and 5.5 mM D-glucose (300 mOsmol/kg and adjusted to pH 7.4 with NaOH). The incubation time was dependent on cell type. HEK293 cells were incubated for 50 min, whereas NIH 3T3 and NHEM cells for 30 min at 37°C, followed by 10 to 20 min washing step in SBS. Cells were plated onto 25 mm glass coverslips for measurements, which fit in a custom-built chamber with a volume of 0.5 ml.

Measurements of $[Ca^{2+}]_i$ were performed using monochromatic-based imaging system (iMIC platform and Polychrome V monochromator, TILL Photonics GmbH). Illumination was generated by a monochromator, which contained a xenon lamp. The excitation wavelength was alternated between 340 nm and 380 nm, and the fluorescence emission of selected areas (cells) was filtered and recorded with a CCD camera. Monochromator settings and data acquisition were controlled by a PC running VisION software (TILL Photonics GmbH). The protocol is part of the document called workspace into which all the experimental data including image files, ratios, and kinetics are stored. Following protocol parameters were used: camera settings: 4x4 binning (20x objective); repeat settings: 500 or 1000 msec cycle time; and acquisition settings: 340 nm and 380 nm excitation wavelength and 20 or 30 msec exposure time to obtain satisfactory signal to noise without inducing photobleaching. The background fluorescence at 340 nm and 380 nm was determined after completion of the measurement by washing cells away (average of the last three reading points) and subtracted from each data point. All

experiments were performed at room temperature in the dark.

2.2.4.4. High-throughput screen (HTS)

As part of the Molecular Libraries Probe Production Network (MLPCN, http://mli.nih.gov/mli/) initiative, the high-throughput screening campaign was executed on the automated Kalypsys robotic platform located at the Scripps Research Institute Molecular Screening Center (SRIMSC; Jupiter, FL). Screening results for the TRPML3 (PubChem AID 1448) and TRPN1 (PubChem AID 1424) agonist primary screens, and all subsequent assays within the screening campaign have been deposited into PubChem. Both primary assays were screened against the full MLPCN screening library, which consisted of 217,969 compounds.

The NIH Molecular Libraries Small Molecule Repository (MLSMR, USA) provided compound collections for the primary and initial confirmation assays (dissolved at concentrations up to 10 mM in DMSO). Reference and ordering information for all compounds can be obtained from the PubChem website (http://pubchem.ncbi.nlm.nih.gov/) by conducting queries with the PubChem substance identifier (SID). For follow-up studies, compound SF-11 was obtained from Maybridge (24). Compounds SF-21, SF-31, SF-41, and SN-1 were obtained from Asinex Ltd. (2). Compounds SF-22 and SF-23 were purchased from Enamine (12), compounds SF-24, SF-32 and SF-51 from ChemBridge (6), and compounds SF-33, SF-61, and SN-2 from Specs (35). Compounds SF-71 and SF-81 were purchased from ChemDiv (7) and Key Organics (20) respectively. All commercially obtained compounds were verified by liquid chromatography-mass spectrometry. Stock solutions of the compounds of 10 mM in DMSO were stored in small aliquots at -80°C.

2.2.4.4.1. High-throughput screen procedure

The following procedure was done by the Scripps Research Institute Molecular Screening Center (SRIMSC; Jupiter, FL).The assay protocols for both TRPML3 and TRPN1 were identically matched. Cells were diluted in growth medium and dispensed into 1536-well black-wall, clear-bottom plates at 1500 cells/well, and allowed to attach for 23 hours at 37°C. Screen Quest™ Fluo-8 No Wash Calcium mix (ABD Bioquest), prepared according to manufacturer instructions, was dispensed into each well. After incubating for 1 hour at 37°C, and 30 min at room temperature, an initial basal fluorescent measurement for 5 sec was performed (470-495 nm excitation and 515-575 nm emission) using the FLIPR^{TETRA}

fluorescence reader (Molecular Devices, USA). Test compounds (2.99 µM final concentration), DMSO alone (carrier control) or Carbachol (87 µM final concentration, as positive control to elicit calcium influx) was added to sample or appropriate control wells, respectively. Then a real time fluorescence measurement was immediately performed for the remaining 120 sec of the assay. The data from each campaign were normalized with basal fluorescence by dividing the maximum fluorescence over the entire real time reading by the initial basal fluorescence. The percent activation for each compound was determined using calculated ratios on a per-plate basis as follows: % ACTIVATION = 100 x (TEST_COMPOUND – LOW_CONTROL) / (HIGH_CONTROL – LOW_CONTROL). Test Compound indicates the ratio of fluorescence of wells containing test compound. Low Control indicates the median average ratio of fluorescence of wells containing DMSO. High Control indicates the median average ratio of fluorescence of wells containing carbachol. To determine agonistic compounds in each primary screen, two values were calculated: First, the average percent activation of all compounds tested and second three times their standard deviation (Hodder et al, 2003). The sum of these two values was used as a cutoff parameter. Any compound that exhibited greater % activation than the cutoff value was considered active.

2.2.4.4.2. Confirmation, counterscreening, and dose-response assays

The procedure was performed by the Scripps Research Institute Molecular Screening Center (SRIMSC; Jupiter, FL). Test compounds active in the primary screening campaign were subsequently confirmed using the same assay protocol and hit cutoff value as used in the primary campaign, except that compounds were tested in triplicate. All confirmation and counterscreen assay data has been uploaded to the PubChem website (AID 1526: TRPML3 hit confirmation; AID 1525: TRPN1 counterscreen).

The potency of compounds that passed confirmation and counterscreening was determined using dose-response assays and EC_{50} values were calculated from the resulting data. A 10-point dose-response curve with a 1:3 dilution series from 29.9 µM to 1.5 nM was used, with compounds being tested in triplicate. Compounds exhibiting an EC_{50} value less than 10 µM were considered active. Dose-response assays were also performed against TRPN1 to confirm that compounds identified as TRPML3 agonists were selective (PubChem AID 1562: TRPML3 dose-response determinations; AID 1682: TRPN1 dose-response determinations). Data were analyzed using a MDL Assay Explorer (version 3.1, Symyx Solutions, Sunnyvale CA, USA). Curve fitting was performed with a four-parameter

equation describing a sigmoidal dose-response curve with adjustable baseline. EC_{50} values were generated from fitted curves by solving for the X-intercept at the 50% inhibition level of the Y-intercept.

2.2.5. Auditory brainstem response measurements - Physiological method

2.2.5.1. Definition

The auditory brainstem response (ABR) is an evoked potential response of auditory activity in the auditory nerve, subsequent fiber tracts and nuclei within the auditory brainstem pathway (for a review, see Stanley, 2009). The measurement of ABR has become a useful procedure for the determination of hearing levels, especially in animals and newborns that cannot respond to behavioral testing. Traditionally, an ABR signal is recorded in the time domain and consists of up to seven vertical positive waves. The clinically relevant ABR waveforms I-V are shown in Figure 9, and were obtained with clicks, a broadband stimulus, starting at fairly high intensity levels. Waves appear differently when clicks are presented lower intensities and eventually disappear when the stimulus was below threshold (Fig. 9A). A given wave's absolute latency is the time delay from 0 msec, where the stimulus is presented, until its peak occurs (Fig. 9B). The time interval between two peaks is called an interwave latency or relative latency. Interwave latencies are usually measured between V-I, III,-I, and V-III. A click stimulus generates a response from the basilar region of the cochlea. However, click stimulation distributes the energy frequency spectrum and provides no frequency specific information. For a pure tone stimulus, the traveling wave reaches its maximum at a specific part of the cochlear duct and then decays. The precise localization of its maximum depends on the frequency of the stimulus. The base of the cochlea is tuned for frequencies as high as 20 kHz and at its apex the organ is sensitive to frequencies as low as 10 Hz in humans. Whereas the frequency range for mice is 5 - 60 kHz. The tonotopic gradient is anatomically manifested in a gradient from base to apex, which includes increasing width of the basilar membrane, and size of outer hair cells, and length of stereocilia. The frequency map is logarithmic so that each decade occupies an equivalent distance on the basilar membrane.

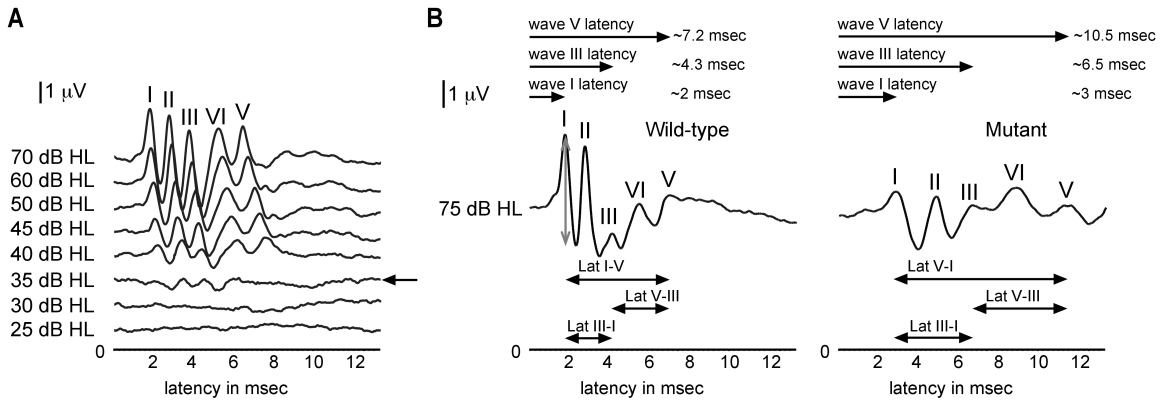

Figure 9: Auditory brainstem response. A: The graph shows representative ABRs of 3-week-old wild-type mice to a click stimulus. ABRs were recorded at sound stimulation intensities (25 to 70 dB HL), HL = hearing level. ABR waves I-V are indicated above the peaks. Threshold can be determined by reducing the stimulus intensity in 5 dB steps. The arrow highlights the hearing threshold at 35 dB HL in this representative example. **B:** Shown are ABRs of 2-week-old wild-type and mutant mice to a click stimulus with an intensity of 75 dB HL. Grey vertical arrow indicates the amplitude, horizontal arrows indicate the wave I, III, and V absolute latencies, and the interwave latencies (Lat) between wave I and V, I and III, and III and V. The mutant mouse displays increased latencies and interwave latencies compared to the wild-type littermate.

2.2.5.2. Waveform components

The signal travels along the auditory pathway from the cochlear nuclear complex proximally to the inferior colliculus (Fig. 10). Waves I-V are consistent, whereas waves VI and VII are more variable. Wave I and II arise from the auditory nerve, wave I from the distal portion of the nerve in the cochlea and wave II from the proximal portion of the auditory nerve as it enters the brain. Subsequent waves are generated at lower levels of the brainstem. Wave III arises from the neuron activity in or near the cochlear nucleus. The ABR wave IV is thought to arise from neurons located in the superior olivary complex. Wave V is generated by the rostal portion of the lateral limniscus as it terminates in the contralateral inferior colliculus. The wave VI and VII are believed to originate in the inferior colliculus (reviewed in Moller, 2007).

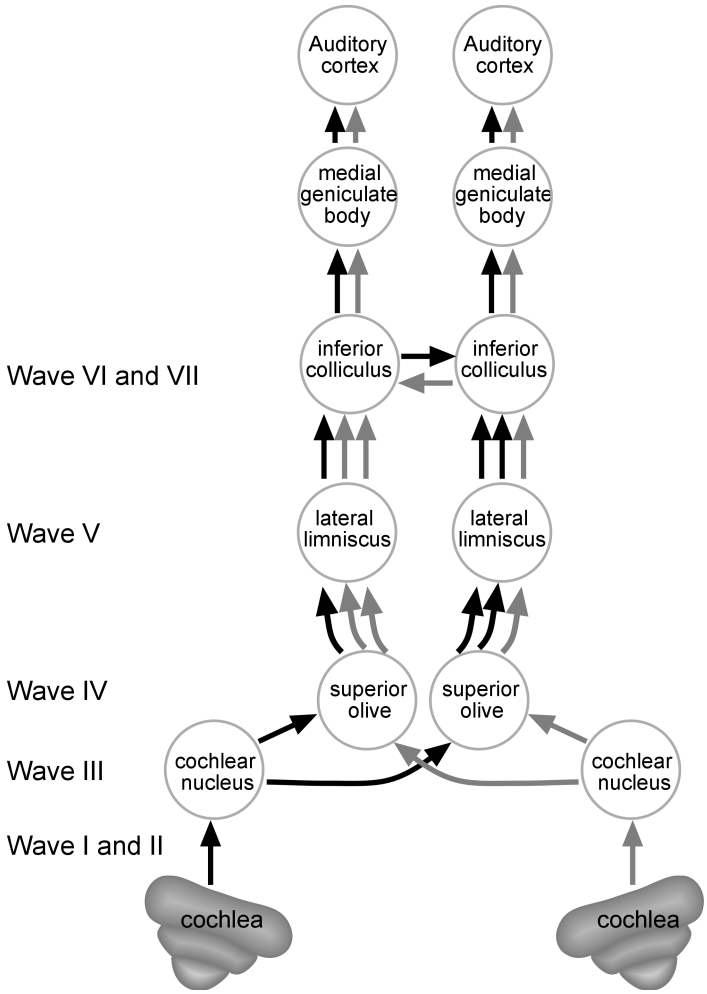

Figure 10: The auditory pathway. The diagram is illustrating the bilateralcentral auditory pathway. The main pathways and nuclei for both cochleae are shown. Wave I and II = auditory nerve, wave III = cochlear nucleus, wave IV = superior olivary complex, wave V = lateral limniscus, wave VI and VII = inferior colliculus. The medial geniculate body (thalamus) and the auditory cortex make up later waves (after 10 msec).The primary connections from two cochlear nuclei are to the opposite hemisphere, indicated by blue and red arrows.

2.2.5.3. High frequency transducer calibration in animal ears using 10B+ probe microphone

The calibration values provided by the manufacture Intelligent Hearing Systems do not accurately reflect the values necessary to correct for an animal cavity. The actual correction value needed will vary from one type of animal to the next, due to the different size cavities. In order to create the calibration table for experiments in mice, recordings from a few sets of ears were needed. The company recommended at least a dozen ears. For the calibration 1 month old FVB/NJ wild-type mice were used. This strain does not display any hearing impairment, which also includes no age-related hearing loss (Zheng et al., 1999). In the SmartEP menu the calibration module was found under

“System>Calibration”. Following the protocol provided by manufacture, click and frequency range from 2 kHz to 32 kHz were tested for every ear. Corrections were applied to representative stimuli: click (-30 dB), 8 kHz (-30 dB), 16 kHz (-15 dB), and 32 kHz (-15 dB). Then, FVB/NJ wild-type mice were measured to determine thresholds, which were compared with the literature (The Jackson Laboratory; Zheng et al., 1999).

2.2.5.4. ABR testing procedure

For stimulus generation, presentation, and ABR acquisition, the Intelligent Hearing System and Smart-EP software (17) were used. Mice were anaesthetized intraperitoneally with 100 mg kg^{-1} ketamine (36) and 20 mg kg^{-1} xylazine (37). The body temperature was maintained at 37°C by placing the mice on an isothermal pad during testing and recovery from anesthesia. Positive, negative and ground platinum subdermal needle electrodes (Model F-E2) (1) were inserted subcutaneously at the vertex, mastoid, and back, respectively (Fig. 11). High Frequency Transducers were used to generate specific acoustic stimuli, routinely starting with the click stimulus, then proceeding through 8 kHz, 16 kHz, and 32 kHz tone bursts. Sound was transmitted through an insert earphone. Alternating click stimuli of 0.1 msec duration and tone bursts with 3 msec were presented to both ears of the animals. All measurements were conducted at a presentation rate of 19.3/sec with 1024 sweeps. ABRs were band-pass filtered below 100 Hz and above 3000 Hz, amplified, and averaged.

2.2.5.5. ABR data analysis

The threshold, amplitude, and latency analysis of the ABR provides information on the hearing status and the integrity of brainstem pathways. The ABR threshold was obtained for each animal by reducing the stimulus intensity in 5 dB steps to identify the lowest intensity at which the first ABR wave was detectable. The absolute threshold is therefore the smallest value of a stimulus that can be detected. This analysis was done online by eye. The latency was determined by detection of all peaks in click ABR waveforms I-V at 75 dB HL. Figure 10B shows an example of a mutant mouse model displaying increased latencies compared to wild-type littermates. The amplitude of ABR waves can be affected by many factors such as body temperature, electrode impedance, and location, levels of physiological noise, and recording procedures, therefore the amplitude may not be a good indicator of hearing level (Zhou et al., 2006). The data obtained from mice under different stimulus conditions were compared statistically using one-way analysis of variance

(ANOVA) or a Student's *t* test (unpaired). Data obtained from female and male mice did not reveal any significant difference. Therefore, all data from both genders were combined in the experiments.

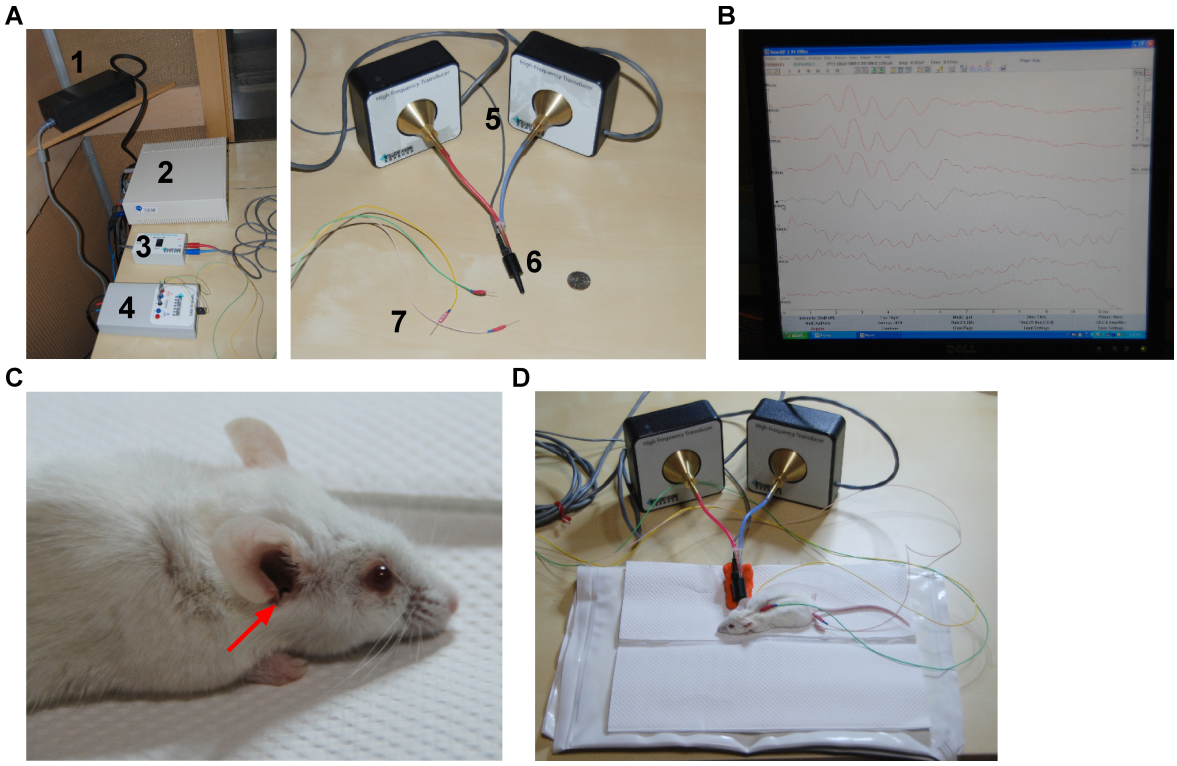

Figure 11: Intelligent Hearing System ABR set up. A: Shown are ABR accessories, 1 = fan; 2 = Universal Smart Box (USB); 3 = sound source (Sound Output Booster Box) with manual switch between high pass filter (high frequencies) and direct (low frequencies); 4 = amplifier (OptiAmp USB) allows to collect electrical activity information for external averaging or monitoring; 5 = High Frequency Transducers (left and right); 6 = earphone with integrated microphone; and 7 = positive, negative and ground platinum subdermal needle electrodes. **B:** Online SmartEP screen (displaying ABR waves). **C:** FVB/NJ wild-type mouse; red arrow indicates the cut in the earlobe, which is necessary to access the ear canal. **D:** Mouse lying on a heating pad, positive (green), negative (yellow), and ground (brown) electrodes are inserted subcutaneously at the vertex (high forehead), mastoid (testing ear), and back, respectively, and earphone inserted into the testing ear.

2.2.6. Statistical analysis

The Synergy KaleidaGraph software was used for statistical analysis of quantitative data. Data are presented as mean values ±SEM. Mean values are the result of at least three independent experiments each (n). Statistical comparisons of means were made using Student's unpaired *t* test or one-way ANOVA followed by Tukey's post test. The tests used are indicated in particular figure legends. Differences were considered as significant at $p<0.01$ (*), and highly significant at $p<0.0001$ (***).

3. Results

3.1. Hair cell death in varitint-waddler and deaf-waddler mice

Sensory hair cells of varitint-waddler mice survive for several postnatal weeks, whereas other cells, such as cochlear intermediate cells or skin melanocytes, die before birth. The first aim of my work was to study whether the survival of varitint-waddler hair cells is linked to their ability to deal with Ca^{2+} loads due to the abundance of plasma membrane calcium ATPases (PMCAs). In collaboration with Dr. Christian Grimm, this work has been published in *The Journal of Biological Chemistry* (Grimm*, Jörs*, et al., 2009).
* Contributed equally

3.1.1. TRPML3(A419P)-mediated cell death is reduced by coexpression of PMCA2 *in vitro*

PMCAs are Ca^{2+} pumps. The majority of the Ca^{2+} that enters hair cells via the stereociliary mechanoelectrical transduction channels is extruded by PMCAs (Lumpkin and Hudspeth, 1998). All four PMCA isoforms are expressed in the mammalian cochlea. Isoform PMCA2 is mainly expressed in hair bundles of outer hair cells and vestibular hair cells and also occurs in inner hair cell bundles, where PMCA1 appears to be the predominant pump (Dumont et al., 2001).

In support of my hypothesis, HEK293 cells expressing TRPML3(A419P) or TRPML3(I362T/A419P) undergo rapid apoptosis. The cells that expressed the mutant channel, but not the control cells that expressed wild-type TRPML3, had a rounded shape and detached from the substrate only 10 hours after transfection. 25-35% of TRPML3(A419P) and TRPML3(I362T/A419P)-expressing HEK293 cells translocated phosphatidylserine from the cytoplasmic leaflet of the plasma membrane to the cell surface, which is an early diagnostic sign of apoptotic cell death that can be revealed by labeling with fluorescent annexin V (Fig. 12A,B). Within the next 15 hours, the number of annexin V-labeled cells increased to 70%. Assuming that Ca^{2+} influx via TRPML3(A419P) and TRPML3(I362T/A419P) was the principle cause of apoptosis, it was expected that coexpression of the plasma membrane calcium pump PMCA2 would lead to a reduction of annexin V-positive cells by directly counteracting the increase of $[Ca^{2+}]_i$. Indeed, the number of apoptotic cells was significantly suppressed by coexpression of PMCA2 (Fig. 12A,B). Wild-type TRPML3-expressing control cells were not positive

for annexin V staining over the examined time period, neither in the absence nor in the presence of PMCA2 (Fig. 12A).

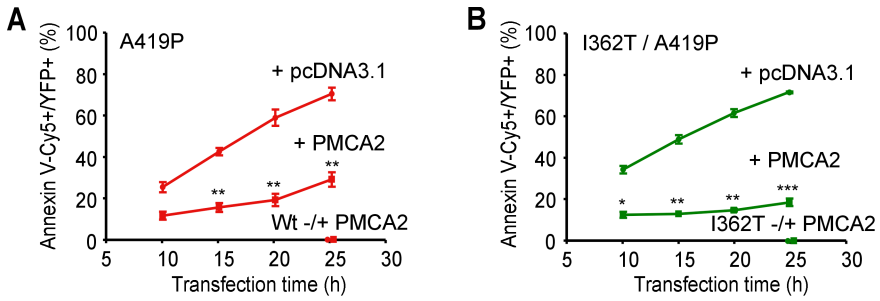

Figure 12: Survival of HEK293 cells expressing varitint-waddler mutant isoforms of TRPML3 with or without PMCA2. A, **B**: Percentage of annexin V-positive cells at various time points (10, 15, 20, and 25 hours) after cotransfection of varitint-waddler mutant isoforms of TRPML3(A419P, I362T/A419P) (C-terminally fused to YFP) with rat PMCA2 or empty vector (pcDNA3.1), respectively. Coexpression of wild-type TRPML3 with PMCA2 or I362T mutant isoform of TRPML3 with PMCA2 did not show any positive annexin V staining after 25 hours. ***p<0.0001, **p<0.001, *p<0.01, Student's *t* test, unpaired.

Calcium imaging experiments revealed that coexpression of PMCA2 with varitint-waddler mutant isoforms TRPML3(A419P) and TRPML3(I362T/A419P) indeed significantly reduces steady-state $[Ca^{2+}]_i$ *in vitro* (Fig. 13A,B). HEK293 cells expressing wild-type TRPML3 or the control mutant isoform TRPML3(I362T) also showed a significant decrease in base-line $[Ca^{2+}]_i$ in the presence of PMCA2 compared to cells cotransfected with wild-type TRPML3 or TRPML3(I362T) and empty vector pcDNA3.1 (Fig. 13A,B). Coexpression of either TRPML3(A419P) or TRPML3(I362T/A419P) with the deaf-waddler isoform PMCA2(G283S) operating at 30% efficacy, resulted in significantly diminished effects on $[Ca^{2+}]_i$ when compared with coexpression of wild-type PMCA2 (Fig. 13A,B). Blocking wild-type PMCA2 with 1 mM sodium vanadate (Yamoah et al., 1998) 4 hours prior to calcium imaging measurements caused a significant increase in $[Ca^{2+}]_i$ in cells coexpressing either TRPML3(A419P) or TRPML3(I362T/A419P) with PMCA2 when compared with non-treated control cells (Fig. 13C). In summary, these experiments show that the ameliorating effect of PMCA2 on cell death is likely due to the decrease in $[Ca^{2+}]_i$ in cells coexpressing both PMCA2 and TRPML3(A419P) or PMCA2 and TRPML3(I362T/A419P) when compared to controls. They also reveal that the deaf-waddler PMCA2(G293S) isoform, which only operates at 30% efficacy, is somewhat effective in ameliorating the increase in $[Ca^{2+}]_i$ in cells expressing mutant TRPML3, but that this amelioration is also significantly worse when compared to cells expressing wild-type PMCA2.

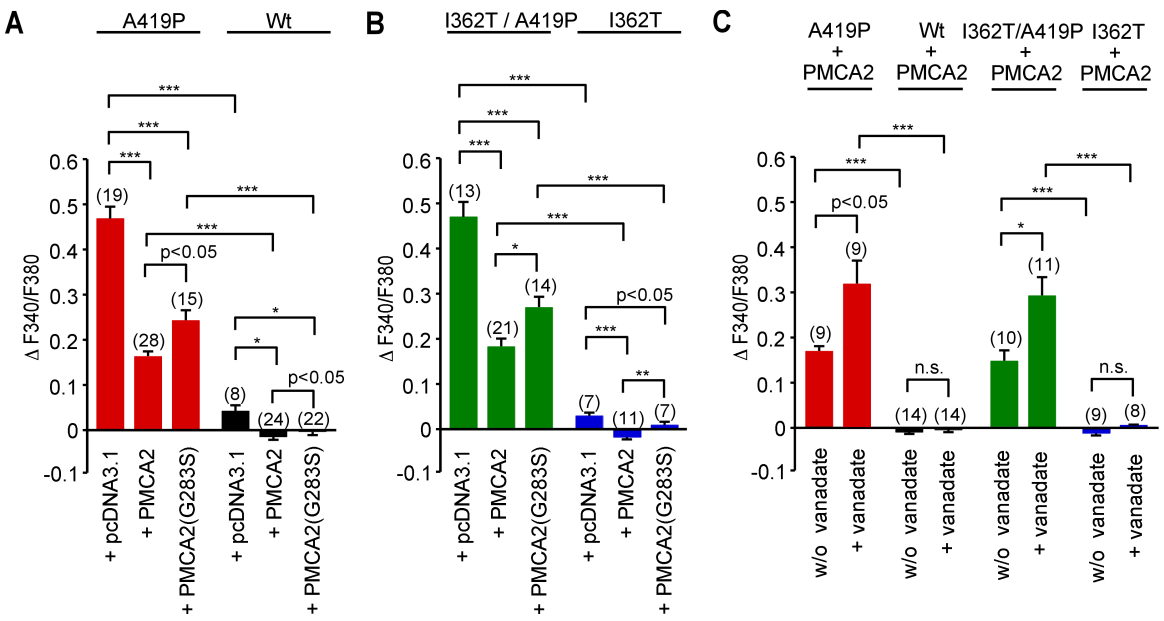

Figure 13: Calcium imaging of HEK293 cells expressing varitint-waddler mutant isoforms of TRPML3 with or without PMCA2. A, **B**: Calcium imaging results showing relative $[Ca^{2+}]_i$ of HEK293 cells coexpressing wild-type TRPML3, TRPML3(I362T) mutant isoform, or varitint-waddler mutant isoforms (A419P and I362T/A419P) in combination with either PMCA2, PMCA2 deaf-waddler mutant isoform (G283S), or empty vector (pcDNA3.1). All expression vectors were cotransfected 1:1. Shown are mean values ±SEM, n = parenthesized. All measurements were performed 15 hours after transfection. **C**: Calcium imaging experiments as described in A and B using 1 mM sodium vanadate to block the PMCA2 effect. Cultured cells were pre-incubated with 1 mM sodium vanadate for 4 hours before measuring. Control cells (w/o vanadate were treated with vesicle solution instead). ***p<0.0001, **p<0.001, *p<0.01, n.s. not significant, Student's *t* test, unpaired. Mean values are the result of n independent measurements with 10-20 cells, each. All mean values were corrected for the values of non-transfected control cells in each measurement. (Data were acquired in collaboration with Dr. Christian Grimm.)

3.1.2. Deaf-waddler PMCA2 worsens degeneration of varitint-waddler cochlear hair cells

In varitint-waddler mice, the sensory hair cells survive for weeks after birth. The survival might be linked to their ability to deal with Ca^{2+} loads due to the abundance of PMCA isoforms. I decided to use deaf-waddler mice that carry a mutation (G283S) in the *Atp2b2* gene to test this hypothesis. Mice homozygous for PMCA2(G283S) (*Atp2b2*$^{dfw/dfw}$) are deaf and exhibit balance disorders (Street et al., 1998). However, compared with *Atp2b2* knockout mice, deaf-waddler mice display a milder phenotype because PMCA2(G283S) retains 30% of its biological activity compared with the wild-type isoform (Penheiter et al., 2001). I hypothesized that the slight reduction in the Ca^{2+} extrusion ability of hair cells increases the severity of the varitint-waddler phenotype. Specifically, I expected double mutants to show more severe hair bundle defects and more extensive hair cell loss than the respective single mutants.

To investigate the PMCA2 deaf-waddler mutant effect on varitint-waddler inner ear hair cell morphology and survival *in vivo*, cochlear whole-mount preparations of P10 and P21 of wild-type mice and of mice carrying single varitint- and deaf-waddler mutant alleles, as well as double mutants, were analyzed (Fig. 14). To generate double mutants, homozygous deaf-waddler (*Atp2b2*$^{dfw/dfw}$) mice were crossed with heterozygous varitint-waddler mice (*Mcoln3*$^{Va/+}$). Likewise, heterozygous varitint-waddler mice were crossed with heterozygous deaf-waddler mutants (*Mcoln3*$^{Va/+}$*; Atp2b2*$^{dfw/+}$). The resulting offspring was genotyped by sequence analysis (Fig. 14A). DNA sequence changes take place at position 1255 (G → C) of *Mcoln3* and at position 847 (G → A) of *Atp2b2*. Genomic DNA fragments of *Mcoln3* and *Atp2b2* were amplified, gel-purified, and sequenced. Oligonucleotides used for PCR and for sequencing are summarized in Table 4 (2.1.8.). Whole-mount preparations of the organs of Corti of all viable allelic combinations were analyzed for overall hair cell morphology and also for quantification of cochlear hair cell numbers at P10 and at P21 (Fig. 14B,C). Inner (IHCs) and outer hair cells (OHCs) of the apical, medial, and basal part of the cochlea were examined. At P10, no significant differences in hair cell numbers were observed in any of the preparations (hair cells/100 µm, means ±SEM): *Mcoln3*$^{Va/+}$*; Atp2b2*$^{dfw/dfw}$: IHC 12 ±0.8; OHC 39 ±0.4, *Mcoln3*$^{Va/+}$*; Atp2b2*$^{dfw/+}$: IHC 13 ±0.2; OHC 38 ±0.3, *Mcoln3*$^{Va/+}$*; Atp2b2*$^{+/+}$: IHC 13 ±0.5; OHC 40 ±0.6, and *Mcoln3*$^{+/+}$*; Atp2b2*$^{dfw/dfw}$: IHC 13 ±0.3; OHC 41 ±0.5 (Fig. 14B,C). However, hair bundles appeared to be affected in *Mcoln3*$^{Va/+}$*; Atp2b2*$^{dfw/dfw}$, *Mcoln3*$^{Va/+}$*; Atp2b2*$^{dfw/+}$, and *Mconl3*$^{Va/+}$*; Atp2b2*$^{+/+}$ mice compared to wild-type mice. The stereocilia of hair cells in these mutants were often fused together and reduced in number, or even completely absent. Nevertheless, *Mconl3*$^{Va/+}$*; Atp2b2*$^{+/+}$ mice carrying solely the varitint-waddler mutant allele, showed a milder hair bundle phenotype. In *Mcoln3*$^{+/+}$*; Atp2b2*$^{dfw/+}$ and *Mcoln3*$^{+/+}$*; Atp2b2*$^{dfw/dfw}$ mice, hair bundle morphology was not different from wild-type mice at P10 (Fig. 14B). To visualize stereocilia (F-actin), whole-mount preparations were labeled with fluorescein isothiocyanate (FITC)-conjugated phalloidin (red).

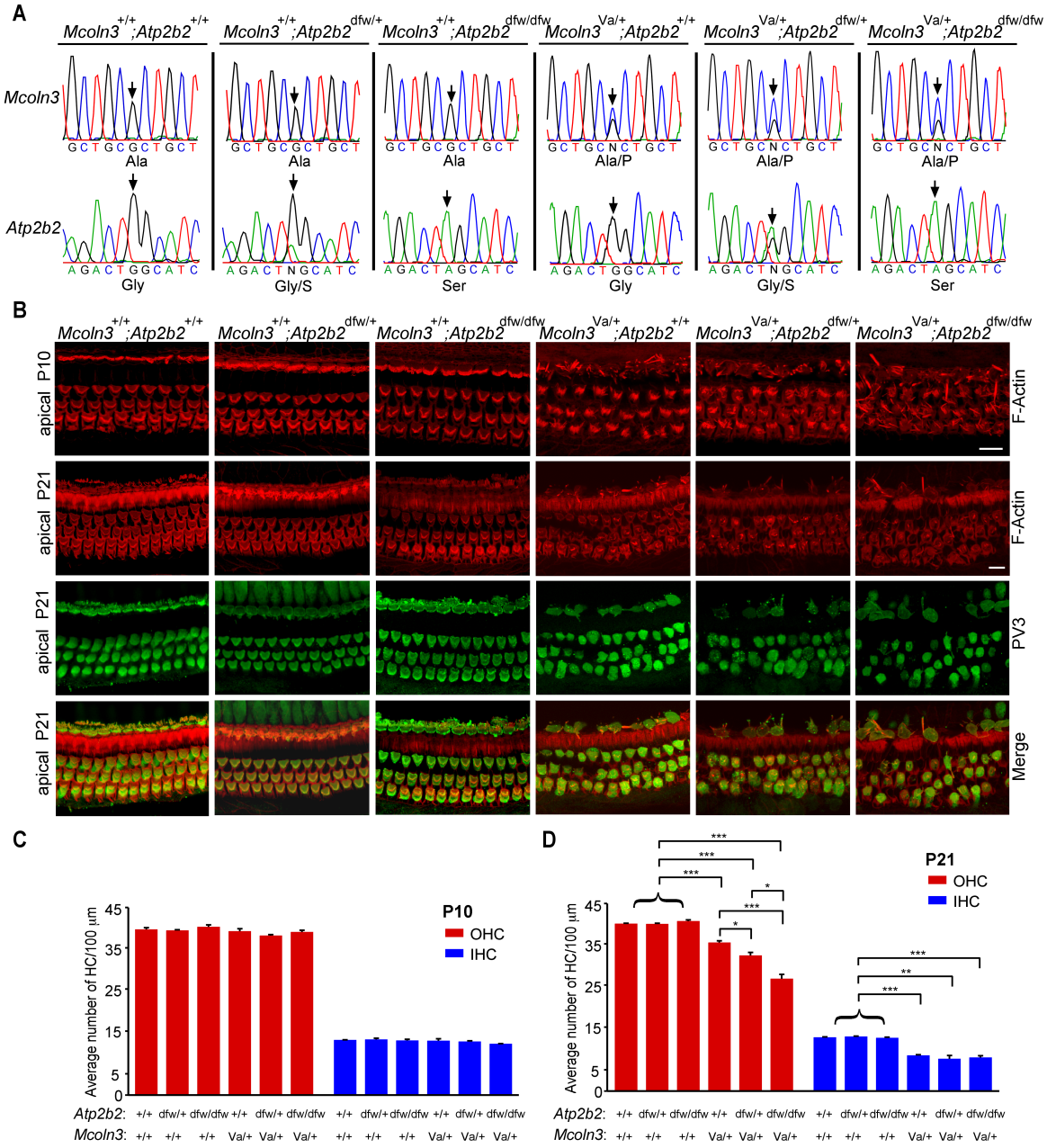

Figure 14: Genotyping and analysis of cochlear hair cell degeneration in P10 and P21 varitint-waddler, deaf-waddler, and varitin-waddler/deaf-waddler double mutant mice. A: Genotyping results showing genomic DNA sequence traces of wild-type mice (*Mconl3*$^{+/+}$*; Atp2b2*$^{+/+}$), heterozygous and homozygous deaf-waddler mice (*Mcoln3*$^{+/+}$*; Atp2b2*$^{dfw/+}$ and *Mcoln3*$^{+/+}$*; Atp2b2*$^{dfw/dfw}$), heterozygous varitint-waddler mice (*Mconl3*$^{Va/+}$*; Atp2b2*$^{+/+}$), as well as DNA sequences of double mutant animals (*Mcoln3*$^{Va/+}$*; Atp2b2*$^{dfw/+}$ and *Mcoln3*$^{Va/+}$*; Atp2b2*$^{dfw/dfw}$). Respective DNA sequence changes take place at position 1255 (G → C) of *Mcoln3* and at position 847 (G → A) of *Atp2b2* and were marked with black arrows. Belonging amino acid to it is written underneath. Nucleobases follow a color-code, A: green, T: red, C: blue, and G: black. **B:** Hair cell degeneration at P10 and P21 as genotyped in A. IHCs and OHCs from apical whole-mount preparations were labeled with FITC-conjugated phalloidin (F-actin) (red) and anti-parvalbumin 3 (PV3) (green). Scale bars = 10 µm. **C:** Quantification of hair cell numbers at P10. **D:** Quantification of hair cell numbers at P21. Shown are the average numbers of IHC (blue) and OHC (red) in the apical part of the cochlea (hair cells/100 µm, means ±SEM of at least three independent samples each, ***p<0.0001, **p<0.001, *p<0.01, Student's *t* test, unpaired).

At P21 the number of inner and outer hair cells was significantly reduced in all mice carrying the varitint-waddler mutation (hair cells/100 µm, means ±SEM): *Mcoln3*$^{Va/+}$*; Atp2b2*$^{dfw/dfw}$: IHC 8 ±0.4; OHC 27 ±1, *Mcoln3*$^{Va/+}$*; Atp2b2*$^{dfw/+}$: IHC 8 ±0.8; OHC 32 ±0.7, and *Mcoln3*$^{Va/+}$*; Atp2b2*$^{+/+}$: IHC 9 ±0.2; OHC 36 ±0.4, when compared to *Mcoln3*$^{+/+}$*; Atp2b2*$^{dfw/dfw}$: IHC 13 ±0.2; OHC 40 ±0.3, *Mcoln3*$^{+/+}$*; Atp2b2*$^{dfw/+}$, or *Mcoln3*$^{+/+}$*; Atp2b2*$^{+/+}$ mice (Fig. 14B,D). In *Mcoln3*$^{+/+}$*; Atp2b2*$^{dfw/+}$ and *Mcoln3*$^{+/+}$*; Atp2b2*$^{dfw/dfw}$ mice, hair bundle morphology as well as the number of hair cells per 100 µm organ of Corti segment was not different from wild-type mice (Fig. 14B,D). For the counting of remaining hair cells, whole-mount preparations were labeled with a hair cell marker parvalbumin 3 (PV3) (green), a Ca^{2+}-binding protein (Heller et al., 2002). Hair cells were strongly labeled throughout the cytoplasm, and the labeling extended into the hair bundles, as would be expected for a mobile Ca^{2+} buffer free to diffuse into the stereocilia cytoplasm. Overall, progressive degeneration of sensory hair cells was observed. Hair bundle and outer hair cell numbers were increasingly more affected starting with the most severe phenotype in *Mcoln3*$^{Va/+}$*; Atp2b2*$^{dfw/dfw}$ mice, over *Mcoln3*$^{Va/+}$*; Atp2b2*$^{dfw/+}$, and finally *Mcoln3*$^{Va/+}$*; Atp2b2*$^{+/+}$ mice, which displayed the mildest phenotype. The number of inner hair cells was significantly reduced in all preparations containing the *Mcoln3*$^{Va/+}$ mutant allele, but in contrast to the outer hair cells, the inner hair cells did not appear to be significantly affected by the presence of the deaf-waddler mutant allele. This inner hair cell result can be explained by the lower expression of PMCA2 and the presence of PMCA1 in inner hair cells compared to outer hair cells (Dumont et al., 2001). In general, the findings demonstrate that the addition of deaf-waddler mutant alleles successively enhances the varitint-waddler phenotype in outer hair cells of the organ of Corti. It supports my hypothesis that the survival of varitint-waddler sensory hair cells might be linked to their ability to deal with Ca^{2+} loads due to the abundance of PMCA isoforms.

3.1.3. Auditory brainstem response measurements of varitint-waddler/deaf-waddler double mutant mice at 3 weeks of age

Auditory brainstem response measurements (ABR) were used to evaluate hearing thresholds of P21 mice. The method including set-up and interpretation of the recordings is explained in the *Materials and Methods* section 2.2.5. Mice homozygous for PMCA2(G283S) (*Mcoln3*$^{+/+}$*; Atp2b2*$^{dfw/dfw}$) were all profoundly deaf; no ABR waveform was observed, even to sound stimuli of 120 dB hearing level (HL) (Fig. 15B).

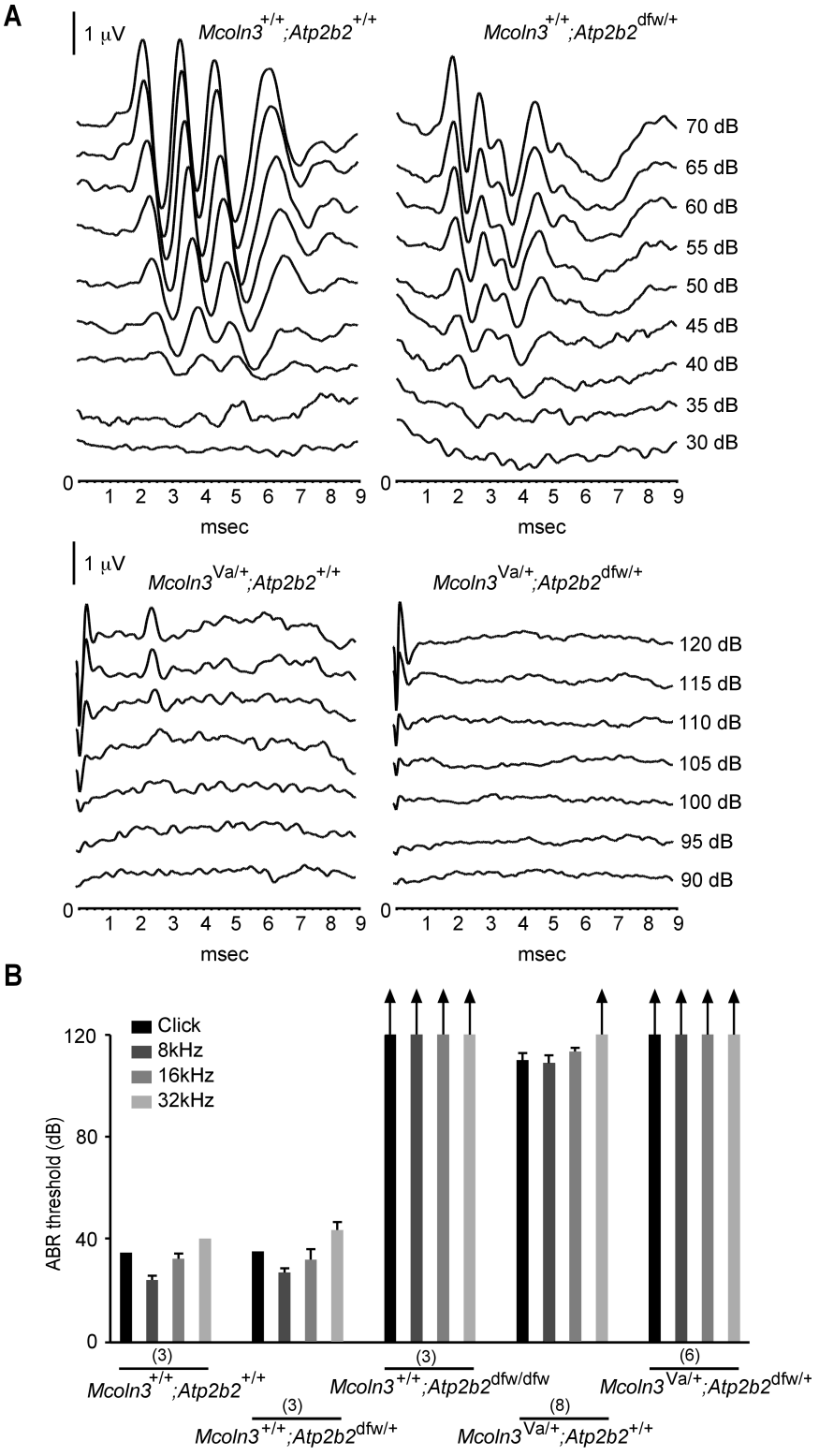

Figure 15: Auditory brainstem response (ABR) measurements. A: Shown are representative auditory brainstem responses of 3-week-old wild-type (RSV/LeJ), heterozygous varitint-waddler (*Mcoln3*$^{Va/+}$), heterozygous deaf-waddler (*Atp2b2*$^{dfw/+}$), and varitint-waddler/deaf-waddler double mutant mice (*Mcoln3*$^{Va/+}$*; Atp2b2*$^{dfw/+}$) to a click stimulus, respectively. **B,** Shown are ABR thresholds (mean values ±SEM) to click, 8 kHz, 16 kHz, and 32 kHz stimuli of *Mcoln3*$^{+/+}$*; Atp2b2*$^{+/+}$, *Mcoln3*$^{+/+}$*; Atp2b2*$^{dfw/+}$, *Mcoln3*$^{+/+}$*; Atp2b2*$^{dfw/dfw}$, *Mcoln3*$^{Va/+}$*; Atp2b2*$^{+/+}$, and *Mcoln3*$^{Va/+}$*; Atp2b2*$^{dfw/+}$, n = number of animals (parenthesized). Black arrows indicate that animals displayed no waveform to sound stimuli of 120 dB hearing level (HL).

Similarly, the double mutants *Mcoln3*$^{Va/+}$*; Atp2b2*$^{dfw/dfw}$ and *Mcoln3*$^{Va/+}$*; Atp2b2*$^{dfw/+}$ were also profoundly deaf (Fig. 15A,B, and data not shown). On the other hand, ABRs were measurable in *Mcoln3*$^{Va/+}$*; Atp2b2*$^{+/+}$ and *Mcoln3*$^{+/+}$*; Atp2b2*$^{dfw/+}$ mice (Fig. 15A,B). ABR thresholds for *Mcoln3*$^{Va/+}$*; Atp2b2*$^{+/+}$ mice were 109 ±3 and 113 ±1 dB HL for 8 kHz and 16 kHz tone bursts and 111 ±1 dB HL for click stimuli (n=8). The ABR thresholds for control mice *Mcoln3*$^{+/+}$*; Atp2b2*$^{dfw/+}$ were 27 ±1.7, 32 ±4.4, and 43 ±3.3 dB HL for 8 -, 16 -, and 32 kHz tone bursts, and 35 ±0 dB HL for click stimuli (n=3). The ABR threshold for *Mcoln3*$^{+/+}$*; Atp2b2*$^{+/+}$ were 25 ±0, 33 ±2, and 40 ±0 dB HL for 8 -, 16 - and 32 kHz tone bursts and 37 ±1.7 dB HL for click stimuli (n=3) (Fig. 15B). The results for *Mcoln3*$^{+/+}$*; Atp2b2*$^{dfw/+}$ mice are in accordance with previous findings that reported no significant differences in comparison to wild-type controls (Brendan et al., 2004). In summary these measurements confirm that already the addition of a single deaf-waddler mutant allele in heterozygote varitint-waddler mice led to profound deafness of *Mcoln3*$^{Va/+}$*; Atp2b2*$^{dfw/+}$ mice at P21, which is in support of my hypothesis that the combination of both mutations, varitint-waddler and deaf-waddler, aggravates the severity of the varitint-waddler phenotype, and in this experiment the hearing loss.

3.1.4. Deaf-waddler PMCA2 worsens degeneration of varitint-waddler utricle hair cells

The clear effects on cochlear hair bundle morphology and outer hair cell numbers elicited by combining one or both deaf-waddler mutant alleles with the heterozygote varitint-waddler mutation raised the question whether reducing PMCA2 activity would also affect the vestibular system. The vestibular system (balance system) is the sensory system that provides the dominant input about the movement and orientation in space (for reviews, see Tascioglu, 2005; Li et al., 2008).

P10 and P21 mouse utricle sensory epithelia were analyzed. To visualize all types of utricular sensory hair cell, whole-mount preparations were visualized with an antibody against calretinin, a Ca^{2+}-binding protein (Li et al., 2008). The hair bundles were labeled with FITC-conjugated phalloidin (F-actin). At P10, no significant hair cell loss or degenerative changes in hair bundle morphology were observed in any of the preparations. At P21, there was no effect on hair cell numbers, but the hair bundle morphology was affected, particularly in the striola region (Fig. 16). The striola is a band of low hair cell density that divides the hair cells into populations with opposing hair bundle polarities (Li et al., 2008).

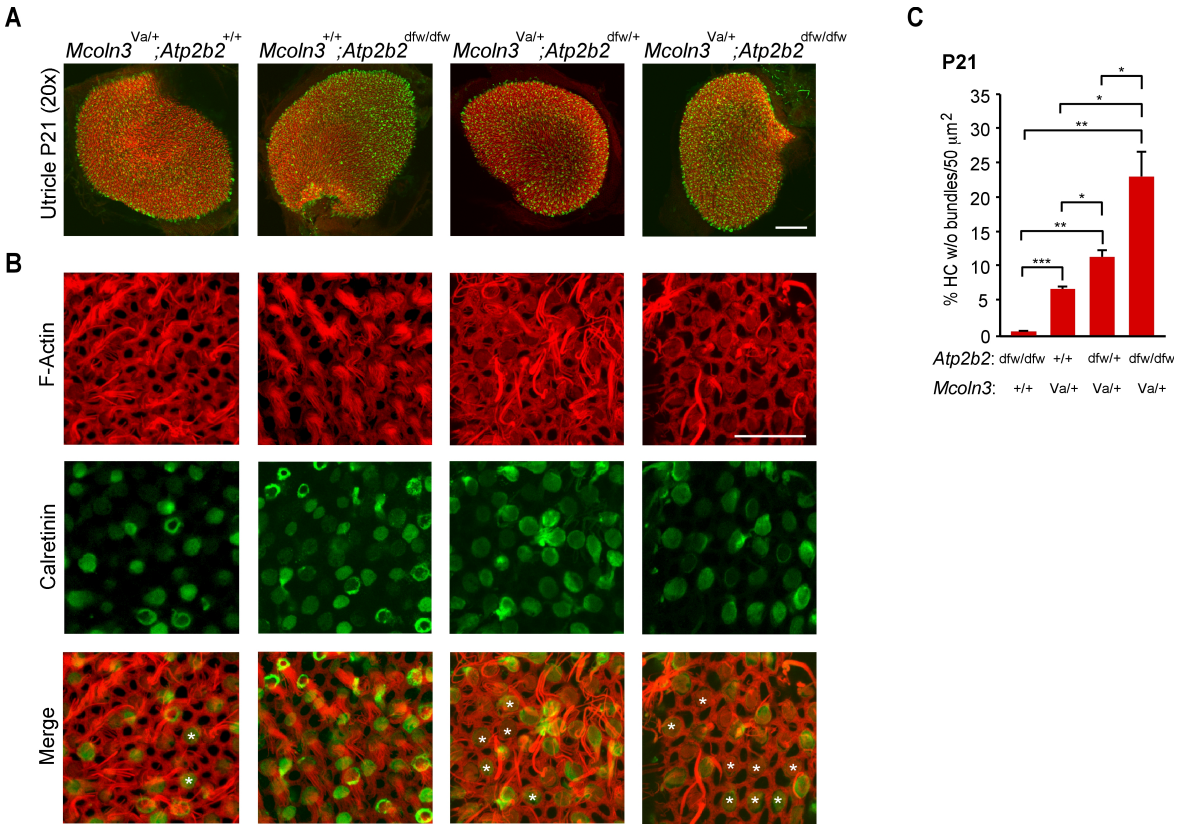

Figure 16: Analysis of vestibular hair cell degeneration in varitint-waddler, deaf-waddler, and varitint-waddler/deaf-waddler double mutant mice. A and B: Shown are representative immunofluorescence staining of P21 murine utricle preparations. The higher magnification examples (B) are from comparable areas in the striola region, where the phenotype was most noticeable. Whole-mount preparations were labeled with FITC-conjugated phalloidin (F-actin) (red) and anti-calretinin (green). Asterisks indicate hair cells without bundles. Scale bar in (A) = 100 µm and in (B) = 20 µm. **C:** Percentage of hair cells (HC) without bundles at P21 in the striola region of the utricle (hair cells/50 µm^2, mean values ±SEM of at least 3 independent samples each, ***p<0.001, **p<0.01, *p<0.05, Student's *t* test, unpaired).

High magnification studies revealed that the most severe hair bundle phenotype was detectable in *Mcoln3*$^{Va/+}$*; Atp2b2*$^{dfw/dfw}$ utricles, where hair bundles generally appeared to be thinner or were completely absent in the striola region. Hair bundles of *Mcoln3*$^{Va/+}$*; Atp2b2*$^{dfw/+}$ utricles were also disorganized and degenerated, and hair cells showed a complete lack of bundles. The striola region of *Mcoln3*$^{Va/+}$*; Atp2b2*$^{+/+}$ utricles was less affected, but still disorganized and splayed, and some hair cells also appeared to lack a hair bundle (Fig. 16B). *Mcoln3*$^{+/+}$*; Atp2b2*$^{dfw/dfw}$ and *Mcoln3*$^{+/+}$*; Atp2b2*$^{dfw/+}$ utricles were not different from the respective wild-type organs (*Mcoln3*$^{+/+}$*; Atp2b2*$^{+/+}$, Fig. 16 and data not shown). The percentage of hair cells per 50 µm^2 without bundles at P21 in the striola region of the utricle was determined (mean values ±SEM) (Fig. 16C): *Mcoln3*$^{Va/+}$*; Atp2b2*$^{dfw/dfw}$ with 22.8 ±3.7%, *Mcoln3*$^{Va/+}$*; Atp2b2*$^{dfw/+}$ mice with 11.4 ±0.9%, *Mcoln3*$^{Va/+}$*; Atp2b2*$^{+/+}$ mice with 6.9 ±0.4%, and *Mcoln3*$^{+/+}$*; Atp2b2*$^{dfw/dfw}$ mice with 0.6 ±0.04%.

The results demonstrate that the addition of deaf-waddler mutant alleles successively enhances the number of hair cells without hair bundles in the striola region of the utricle.

3.1.5. Lowering of PMCA2 efficacy causes circling and coordination problems in varitint-waddler mutants

An obvious vestibular phenotype could be observed when combining varitint-waddler and deaf-waddler mutant alleles. Double mutants displayed circling behavior (Fig. 17). Wild-type mice, heterozygous varitint-waddler mice (*Mcoln3*$^{Va/+}$*; Atp2b2*$^{+/+}$), or mice carrying one or both alleles of the deaf-waddler mutation (*Mcoln3*$^{+/+}$*; Atp2b2*$^{dfw/+}$, *Mcoln3*$^{+/+}$*; Atp2b2*$^{dfw/dfw}$) did not show circling behavior during the investigated time period, which was up to 6 months postnatal. In contrast, 67% (6 of 9 animals) and 71% (12 of 17 animals) of the *Mcoln3*$^{Va/+}$*; Atp2b2*$^{dfw/+}$ double mutants at 3 and at 6 weeks of age, respectively, as well as 100% of 3- and 6-weeks-old *Mcoln3*$^{Va/+}$*; Atp2b2*$^{dfw/dfw}$ double mutants showed overt circling behavior. *Mcoln3*$^{Va/+}$*; Atp2b2*$^{dfw/+}$ mice circled with 15.3 ±3.9 rpm (rounds per minute, mean ±SEM) at 3 weeks of age and with 23.9 ±3.4 rpm at 6 weeks of age. *Mcoln3*$^{Va/+}$*; Atp2b2*$^{dfw/dfw}$ mice circled with 11.7 ±2.7 rpm at 3 weeks of age and with 12.8 ±3.8 rpm at 6 weeks of age. The slower circling speed of *Mcoln3*$^{Va/+}$*; Atp2b2*$^{dfw/dfw}$ animals is likely due to the increased waddling phenotype. The mice's gait was affected by severe coordination problems in addition to circling (Fig. 17).

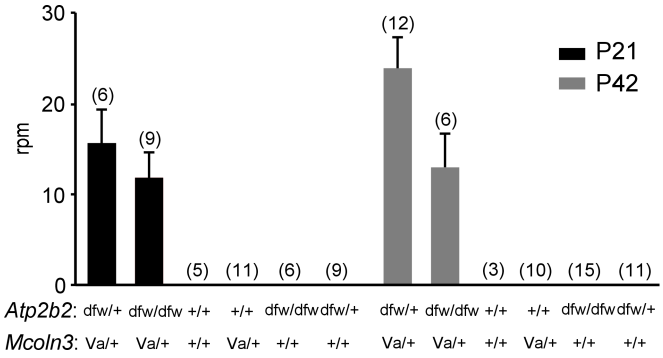

Figure 17: Circling behavior of varitint-waddler/deaf-waddler double mutant mice. The quantification was conducted at 3 and 6 weeks postnatal (P21 and P42). Wild-type littermates (RSV/LeJ), heterozygous varitint-waddler mice (*Mcoln3*$^{Va/+}$*; Atp2b2*$^{+/+}$), and deaf-waddler mutant mice (*Mcoln3*$^{+/+}$*; Atp2b2*$^{dfw/+}$and *Mcoln3*$^{+/+}$*; Atp2b2*$^{dfw/dfw}$) did not display circling behavior at P21 and P42 (n = parenthesized number = number of mice tested). 67% (n=6/9, P21) and 71% (n=12/17, P42) of the heterozygous double mutants (*Mcoln3*$^{Va/+}$*; Atp2b2*$^{dfw/+}$) as well as 100% (n=9/9, P21, n=6/6, P42) of the *Mcoln3*$^{Va/+}$*; Atp2b2*$^{dfw/dfw}$ double mutants showed severe circling behavior. Non-circling mice were excluded from rpm calculations. For each mouse, three tests of quantified circling were performed at consistent time points on different days.

3.2. High-throughput screen for small molecule activators of TRPML3

The identification of natural or artificial activators of TRPML3 could be an important step toward a better understanding of the channel's characteristics and its *in vivo* functionality. In this chapter, the identification of small molecule activators by high-throughput screening will be reported and discussed. This work has recently been published in *Chemistry & Biology* (Grimm*, Jörs*, et al., 2010).

* Contributed equally

3.2.1. Stable cell lines expressing hTRPML3 and drTRPN1

HEK293 cells stably expressing C-terminal YFP protein fusion constructs of human TRPML3 and *danio rerio* (dr) TRPN1 were used for the high-throughput screens (Fig. 18). TRPN1, which is only distantly related to TRPML3 (Fig. 1), served as a negative control for the TRPML3 screening project. Expression vectors were based on pcDNA3.1, which is described in the *Materials and Methods* part 2.1.6.1. The pcDNA3.1 vector contains the neomycin resistance gene for selection of stable cell lines conferring resistance to geneticin (G418) at a final concentration of 0.8 mg/ml. This amount of G418 was determined in dose-response pilot experiments and it kills HEK293 cells that do not express the selection gene coexpressed with TRPML3 or TRPN1. For more details on the generation of stable HEK293 cell lines, see in the *Materials and Methods* part 2.2.2.2. The cells were cultured under continuous selective pressure. The expression of the ion channels was monitored by their YFP-tag. Morphology, expression level, and stability of integration of the TRP channel protein in the generated stable cell lines were confirmed after each passage by fluorescence microscopy (Fig. 18A), and cell lines with abnormalities, such as loss of the fluorescent reporter, or unusual morphology were eliminated. TRPML3 and TRPN1 are located in the plasma membrane and in intracellular compartments when overexpressed in HEK293 cells.

Western blot analyses were done with all candidate stable lines to ensure that the fusion proteins were present as full-length isoforms. Western blots were incubated with a GFP antibody (Table 5), which also recognizes the YFP isoform. Figure 18B shows one representative of each generated TRP cell line. The fusion protein TRPML3-YFP is migrating at approximately 95 kDa and *danio rerio* TRPN1-YFP at 230 kDa (Fig. 18B). In addition to the human TRPML3-YFP stable cell line, a murine TRPML3-YFP stable cell line was generated. After comparison of murine and human TRPML3 cell lines for

stability of the tagged ion channels, growth, and survival rate after freezing and thawing, a human TRPML3-expressing cell line was selected for high-throughput screening. The human TRPML3 and *danio rerio* TRPN1 lines that were selected for screening were expanded and frozen in aliquot batches of about 50, to ensure that identical and early passage numbers were used for high-throughput experiments.

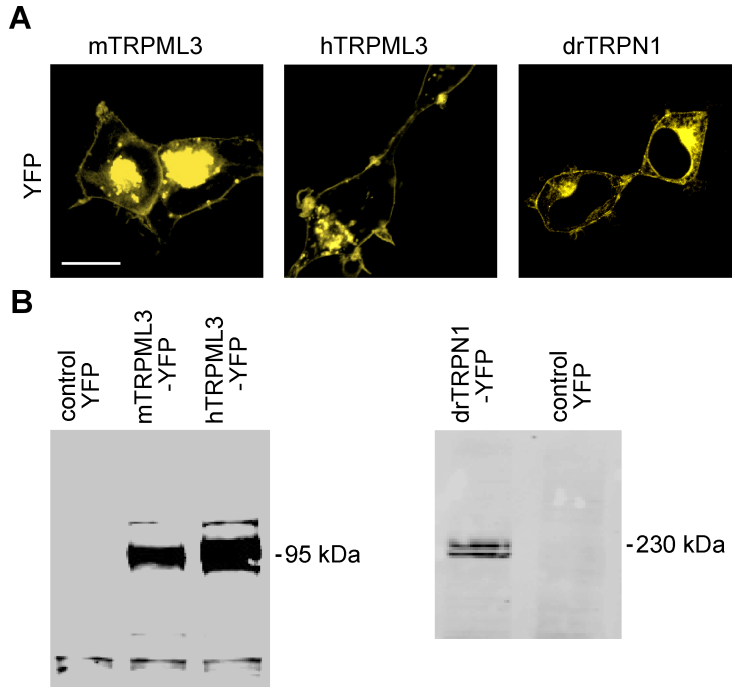

Figure 18: HEK293 cells stably expressing murine and human TRPML3 and *danio rerio* TRPN1. A: Shown are representative cells stably expressing the respective C-terminal YFP fusion constructs of mTRPML3, hTRPML3, and drTRPN1. Scale bar = 20 µm. **B:** Western blot analysis shows YFP-tagged mTRPML3, hTRPML3, and drTRPN1 visualized with antibody to GFP. Murine and human TRPML3-YFP are migrating at approximately 95 kDa and drTRPN1-YFP as a double band at approximately 230 kDa.

3.2.2. High-throughput screen reveals 53 activators of TRPML3

For conducting the high-throughput screen, a grant application was submitted to the National Institutes of Health (NIH) in response to the NIH high-throughput compound screening roadmap initiative (http://nihroadmap.nih.gov/molecularlibraries/). The application was funded and assigned to the Molecular Libraries Screening Centers Network (http://mli.nih.gov/mli/secondary-menu/mlscn/) and a collaborative project with the Scripps Research Institute Molecular Screening Center (Jupiter, Florida, USA) was initiated. To identify compounds that elicit a TRPML3-specific increase of $[Ca^{2+}]_i$, two parallel high-throughput screens were conducted with stable HEK293 cells expressing hTRPML3 or drTRPN1 protein. The screening conditions for high-throughput calcium

flux screening, with Fluo-8 calcium indicator dye, were optimized to give the best balance between assay performance, reagent consumption, and suitability of the protocol for robotic-based screening (see the *Materials and Methods* section for final conditions (2.2.4.4.)). This process established precisely matched conditions for both screening campaigns. A total of 217,969 compounds were tested at a concentration of 2.99 µM using FLIPR-based screening technology in 1536-well plate format. To determine agonistic compounds in each screen, two values were calculated: First, the average percent activation of all compounds tested, and second three times their standard deviation (Hodder et al, 2003). The sum of these two values was used as a cutoff parameter. Any compound that exhibited greater percentage activation than the cutoff value was considered active. A total of 632 primary hits were identified for TRPML3 (Fig. 19). In comparison with the control TRPN1 cell line, 300 overlapping compound hits were removed, resulting in 332 unique hits for TRPML3. Triplicate retesting using the same assay conditions as the original screen confirmed 244 candidates. Comparison of compound responses with the drTRPN1 cell line revealed that 29 of these 244 were active, and therefore, considered as non-selective for hTRPML3. 27 compounds were unavailable for further testing, which left 188 candidates. Compounds that passed this confirmation and counterscreening were used for dose response relationships (for a more detailed description see *Materials and Methods* section 2.2.4.4.2.). A 10-point dose-response curve with a 1:3 dilution series from 29.9 µM to 1.5 nM was used, with compounds being tested in triplicate. Dose-response assays were also performed against drTRPN1 to confirm that compounds identified as hTRPML3 agonists were selective. All confirmation, counterscreen assay, and dose-response data have been uploaded to the PubChem website (AID 1526: TRPML3 hit confirmation; AID 1525: TRPN1 counterscreen; AID 1562: TRPML3 dose-response determinations; AID 1682: TRPN1 dose-response determinations). Overall, agonist candidacy was based on <10 µM EC_{50} (median effective concentration) for hTRPML3, >10 µM EC_{50} for the control TRPN1, and >10-fold selectivity of EC_{50} on TRPML3 over TRPN1. The 53 compounds that fulfilled these criteria are shown in Table 6.

Table 6: List of the 53 identified small compound candidate activators of TRPML3. Shown in bold are the candidate activators from 8 different scaffolds (SF), as well as two singletons (SN) that were used in follow-up analyses. Maximal percent activation was normalized to the maximum carbachol response, and EC_{50} values are reported as mean values ±SD (n=3).

	SF	#	PubChem SID	Max % Activation (TRPML3)	Max % Activation (TRPN1)	EC_{50} (μM) (TRPML3)	EC_{50} (μM) (TRPN1)
1	**1**	**SF-11**	**26731169**	**135 ± 20**	**8 ± 1**	**0.26 ± 0.04**	**>29.9**
2	-	-	14727865	78 ± 4	12 ± 2	0.35 ± 0.1	>29.9
3	-	-	14737026	65 ± 3	23 ± 2	0.37 ± 0.09	>29.9
4	**-**	**SN-1**	**857766**	**151 ± 14**	**6 ± 0**	**0.88 ± 0.06**	**>29.9**
5	1	-	26731235	161 ± 7	17 ± 1	0.83 ± 0.06	>29.9
6	**2**	**SF-21**	**24801657**	**200 ± 7**	**61 ± 2**	**0.45 ± 0.04**	**>14.24 ± 2.03**
7	**2**	**SF-22**	**14746905**	**156 ± 16**	**1 ± 0**	**0.66 ± 0.06**	**>29.9**
8	**3**	**SF-31**	**14722627**	**130 ± 20**	**2 ± 1**	**0.99 ± 0.03**	**>29.9**
9	-	-	3716889	146 ± 6	15 ± 1	1.18 ± 0.2	>29.9
10	-	-	24808155	219 ± 10	27 ± 1	1.24 ± 0.33	>29.9
11	-	-	843249	113 ± 5	22 ± 1	1.25 ± 0.54	>29.9
12	-	-	14727681	181 ± 13	41 ± 7	1.27 ± 0.17	>29.9
13	3	-	24801969	144 ± 6	25 ± 4	1.34 ± 0.14	>29.9
14	-	-	22412252	63 ± 1	8 ± 5	1.34 ± 0.03	>29.9
15	3	-	14740076	137 ± 4	29 ± 3	1.35 ± 0.16	>29.9
16	**2**	**SF-23**	**3716245**	**174 ± 12**	**1 ± 1**	**1.10 ± 0.15**	**>29.9**
17	3	-	17412681	94 ± 5	6 ± 4	1.4 ± 0.14	>29.9
18	**4**	**SF-41**	**24787221**	**138 ± 12**	**12 ± 1**	**2.11± 0.69**	**>29.9**
19	**5**	**SF-51**	**7974698**	**175 ± 18**	**47 ± 3**	**0.93 ± 0.2**	**>29.9**
20	**3**	**SF-32**	**24786634**	**119 ± 5**	**2 ± 1**	**1.81 ± 0.14**	**>29.9**
21	-	-	17508875	137 ± 14	1 ± 1	1.54 ± 0.17	>29.9
22	**2**	**SF-24**	**17414375**	**86 ± 7**	**2 ± 0**	**2.41 ± 0.87**	**>29.9**
23	**3**	**SF-33**	**14727674**	**119 ± 21**	**2 ± 1**	**4.79 ± 1.09**	**>29.9**
24	3	-	24801736	121 ± 7	14 ± 2	1.71 ± 0.15	>29.9
25	-	-	4255785	104 ± 6	21 ± 2	1.78 ± 0.28	>29.9
26	**-**	**SN-2**	**22411609**	**149 ± 11**	**3 ± 1**	**1.13 ± 0.16**	**>29.9**
27	3	-	7973744	105 ± 6	15 ± 2	1.81 ± 0.3	>29.9
28	-	-	17505026	133 ± 13	24 ± 3	1.81 ± 0.08	>29.9
29	3	-	4257276	130 ± 10	12 ± 1	1.82 ± 0.06	>29.9
30	**6**	**SF-61**	**17387508**	**120 ± 22**	**2 ± 1**	**3.74 ± 1.02**	**>29.9**
31	3	-	4263276	111 ± 7	5 ± 2	1.88 ± 0.17	>29.9
32	4	-	24792359	146 ± 8	7 ± 2	1.94 ± 0.46	>29.9
33	-	-	17410437	129 ± 8	1 ± 0	1.99 ± 0.45	>29.9
34	3	-	17414208	87 ± 6	5 ± 2	2.09 ± 0.45	>29.9
35	-	-	24787220	112 ± 16	10 ± 2	2.09 ± 0.21	>29.9
36	-	-	14739638	149 ± 8	11 ± 5	2.25 ± 0.23	>29.9
37	3	-	17414135	121 ± 11	3 ± 2	2.27 ± 0.21	>29.9
38	-	-	11532942	63 ± 3	28 ± 5	2.28 ± 0.23	>29.9
39	**7**	**SF-71**	**24790495**	**85 ± 8**	**2 ± 1**	**2.52 ± 0.83**	**>29.9**
40	2	-	26731263	114 ± 7	1 ± 1	2.32 ± 0.22	>29.9
41	-	-	14727636	99 ± 9	15 ± 4	2.33 ± 0.12	>29.9
42	-	-	24802071	192 ± 9	22 ± 9	2.39 ± 0.09	>29.9
43	**8**	**SF-81**	**14733059**	**138 ± 21**	**1 ± 0**	**2.29 ± 0.19**	**>29.9**
44	2	-	22410940	109 ± 7	9 ± 2	2.54 ± 0.24	>29.9
45	9	-	17408204	149 ± 16	25 ± 1	2.54 ± 0.05	>29.9
46	3	-	14745679	74 ± 3	21 ± 2	2.59 ± 0.12	>29.9
47	5	-	17412260	91 ± 10	6 ± 0	2.67 ± 0.52	>29.9
48	2	-	22405272	119 ± 8	28 ± 5	2.76 ± 0.52	>29.9
49	3	-	14720454	104 ± 3	17 ± 3	2.84 ± 0.68	>29.9
50	-	-	17406723	119 ± 13	24 ± 6	2.85 ± 0.27	>29.9
51	-	-	22411449	104 ± 7	6 ± 3	2.86 ± 0.69	>29.9
52	3	-	24802031	130 ± 11	3 ± 3	2.88 ± 0.36	>29.9
53	3	-	22411442	110 ± 17	20 ± 2	2.92 ± 0.5	>29.9

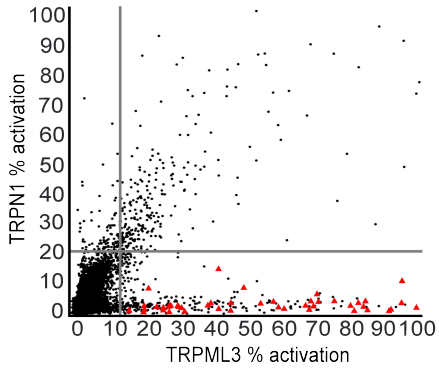

Figure 19: Correlation plot for hTRPML3 and drTRPN1 high-throughput screens. Circles or triangles represent the responses, expressed as percentage activation, for 217,969 compounds tested for activation of TRPML3 (x-axis) or TRPN1 (y-axis). Molecules found to be TRPML3-selective agonists are displayed as red triangles. Compound activity is normalized to the maximum carbachol response. Vertical and horizontal grey lines represent the hit cutoff values of the TRPML3 (11.46%) and TRPN1 (18.88%) screens. (Data were kindly provided by Dr. S. A. Saldana.)

3.2.3. Chemotypes of identified molecule activators

Structure analyses placed the 53 activators into nine chemical scaffolds (SF) and 20 singletons (SN). Singletons do not share obvious chemical and structural relationship with the rest of the identified compounds. "TRPML3-selective" small compound agonist scaffolds were: SF-1 = (pyrazol-5-yl)isoxazole-benzenesulfonamides, SF-2 = secondary arylsulfonamides, SF-3 = tertiary arylsulfonamides, SF-4 = sulfonylarylpiperazines, SF-5 = 1-(2,2,4-trimethylquinolinyl)-alkylones, SF-6 = spirobenzoannulene-arylpyrazo-lones, SF-7 = t-butyl-3-methyl-4-(arylsulfonyl)-pyrazol-5-ols, SF-8 = aryl-sulfonyl-pyridin-2-ones, and SF-9 = t-butyl-3methylfuran-2-carboxamides.

3.2.4. Identified compounds elicit Ca^{2+} influx into TRPML3-expressing HEK293 cells

The 15 compounds that were selected for follow-up analyses are highlighted in red in Table 6. Criteria for this selection were low EC_{50} values for TRPML3 activation, low activation of TRPN1, and compound availability. At least one representative of each chemical scaffold and two singletons, SN-1 and SN-2 were selected for further analyses. SF-9 compounds were not tested, because they were not commercially available. All 15 compounds were obtained from commercial vendors, verified by liquid chromatography-mass spectrometry, and reconfirmed in a tertiary TRPML3 and TRPN1 calcium imaging assay. In this assay, all 15 compounds displayed EC_{50} values of less than 5 µM. In the case of SF-11, SF-21, SF-22, SF-31, SF-51 and SN-1 the EC_{50} values were less than 1 µM.

Compounds SF-21 and SF-51 exhibited activity against TRPN1 (Table 6). This activity, however, could not be confirmed in follow-up experiments using single-cell calcium imaging and patch-clamp electrophysiology. The follow-up calcium imaging experiments differed from the confirmation tests in the use of fura-2 *versus* fluo-8 calcium indicator dye, transiently transfected cells *versus* stable cell lines, and analysis of individual cells *versus* a cell population. Both methods are explained in *Materials and Methods* section 2.2.4. Electrophysiological patch-clamp measurements provided an additional independent assay to calcium imaging. Furthermore, electrophysiology was showing inward and outward current differences, and current/voltage relationships for each compound activation. Dr. Christian Grimm performed the electrophysiological measurements.

Specifity and activity were confirmed using HEK293 cells transiently expressing hTRPML3, mTRPML2, hTRPML1, hTRPM2, mTRPV5, mTRPV2, hTRPC3, drTRPN1, and hTRPA1 (all C-terminally tagged with YFP). When used at 10 μM, each compound alone elicited strong and prompt increases of intracellular Ca^{2+} in TRPML3 transfected cells using fura-2-AM as the calcium indicator dye (Fig. 20). The strongest responses, amounting to ≥1.5-fold increase in the 340 nm/380 nm ratio, were obtained with compounds SF-21, SF-22, SF-23, SF-31, SF-41, SN-1, and SN-2. Compounds SF-21, SF-41, and SN-2 elicited a more rapid Ca^{2+} influx than the other compounds did. SF-33 and SF-51 displayed the slowest kinetics. Three compounds, SF-21, SF-41, and SF-81, also elicited responses in TRPML2-expressing HEK293 cells (Fig. 20B,D, and H, green traces and bars). In contrast, no responses were observed in cells expressing wild-type TRPML1. Normally, TRPML1 is predominantly localized in lysosomal or endosomal membranes. However, when both lysosomal targeting sequences (LTS) were deleted, the mutant isoform TRPML1(NC) was localized to the plasma membrane (see 3.2.9. for more details), and compound SF-22was able to activate this channel (Fig. 20B). None of the other compounds substantially activated any of the other TRP channels tested. Compounds SF-21 and SF-51 exhibited activity against TRPN1 in initial screenings (Table 6). This activity could not be confirmed in calcium imaging experiments. One possible reason for this discrepancy could be the different manufactures or the storage of the compound stock solution dissolved in DMSO, which could have led to degradation products with different features. Additional controls included cells transfected with control YFP plasmid only and non-transfected HEK293 cells, which did not show any response.

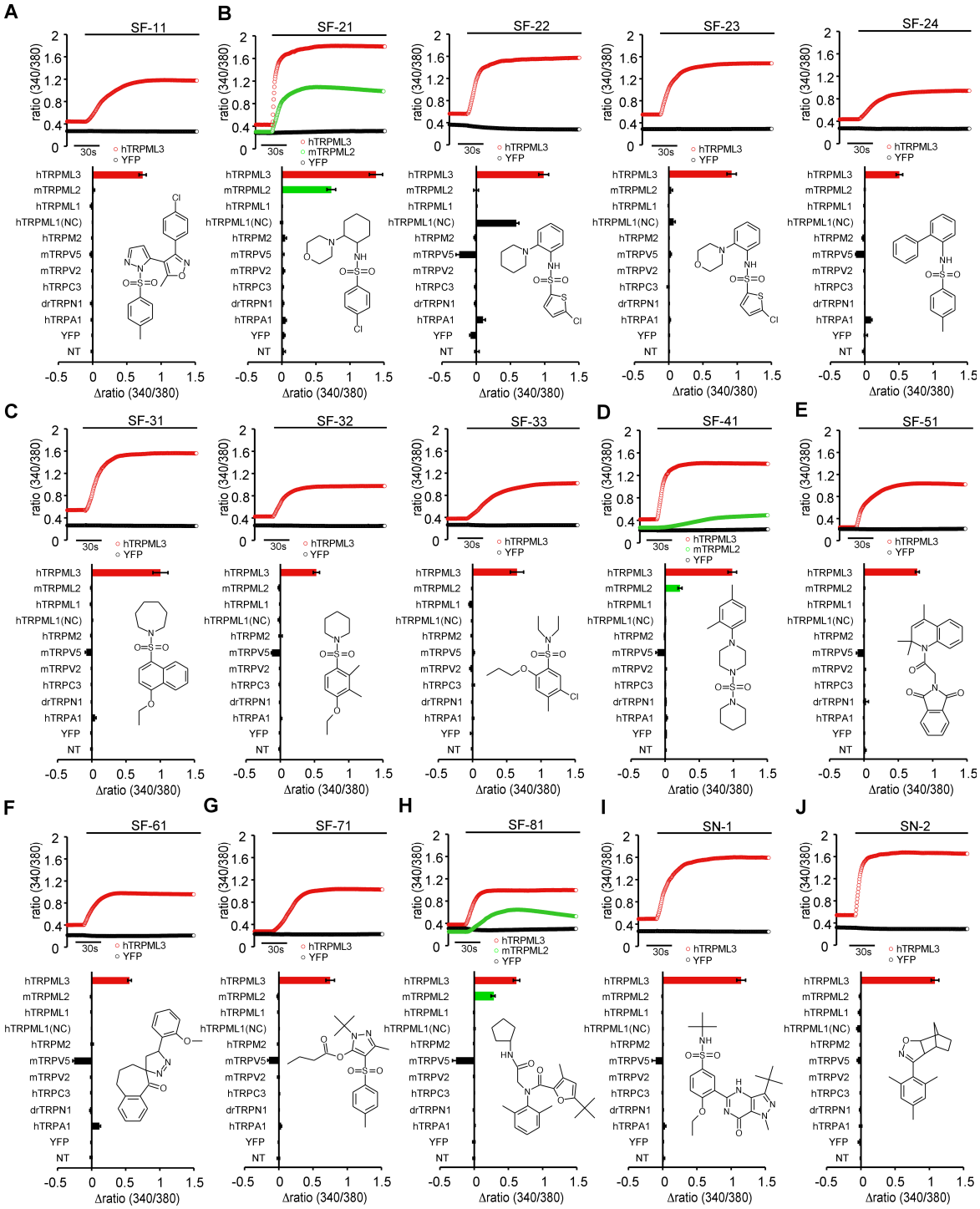

Figure 20: Identified compounds elicit Ca^{2+} influx into TRPML3-expressing HEK293 cells. A-H: $[Ca^{2+}]_i$ increases of HEK293 cells transiently expressing human (h) TRPML3, other human, or murine (m) TRP channels, or *danio rerio* (dr) TRPN1 in response to application of 10 µM of 13 selected compounds from 8 different scaffolds (SF-11, -21, -22, -23, -24, -31, -32, -33, -41, -51, -61, -71, -81). TRPML1(NC) is a TRPML1 variant that is localized to the plasma membrane. YFP-transfected or non-transfected (NT) HEK293 cells were used as additional controls. SF-21, SF-41, and SF-81 activated TRPML2, indicated in green. Bar diagrams represent average $[Ca^{2+}]_i$ levels 2 min after compound application relative to the respective Ca^{2+} level before application (mean values ±SEM, n≥3 independent experiments with 20-30 cells). **I-J:** Calcium imaging experiments as described in A-H showing the effect of 10 µM of the singleton compounds SN-1 (I) and SN-2 (J). All measurements were performed 20-25 hours after transfection.

TRPV5-expressing HEK293 cells displayed increased baseline intracellular Ca^{2+} concentration, based on the feature that TRPV5 is a constitutively active calcium selective cation channel (Vennekens et al., 2000). Low internal calcium levels further activate the channel, and a Ca^{2+}-dependent feedback regulation leads to fast channel inactivation. After application of some compounds to TRPV5-expressing HEK293 cells, a decrease of intracellular calcium was measured. This decrease could be a result of direct channel inactivation, thereby indicating that these compounds might be able to directly interact with TRPV5. This has to be further investigated.

The findings obtained with single-cell calcium imaging were confirmed in whole-cell patch-clamp experiments, which were performed in collaboration with Dr. Christian Grimm. All compounds displayed inwardly rectifying currents with average current densities between 20 and 600 pA/pF at -80 mV (Fig. 21). The sulfonamide probenicid (4-(dipropylsulfamoyl)benzoic acid) was used as a negative control, and did not activate TRPML3 (Fig. 21). Cells transfected with YFP only served as controls and they showed no significant currents. Average current densities in TRPML3 transfected cells perfused with compounds SF-22, SF-23, SF-31, SF-81, SN-1, and SN-2 were comparable to average current densities obtained from cells expressing the constitutively active varitint-waddler isoform A419P of TRPML3, which was used as a positive control (Fig. 21, green bar). Stronger responses were obtained with SF-21, SF-41, and SF-51. Compound SF-11 elicited weaker but significant responses in TRPML3-expressing cells, when compared with the TRPML3(A419P) control. Table 7 is summarizing the data obtained by calcium imaging and whole-cell patch-clamp experiments, comparing TRPML3- with YFP (control)-expressing HEK293 cells.

To investigate whether the compounds activate TRPML3 from the inside or outside of the cell, cell permeance was determined for compounds SF-11, SF-22, and SN-2 in collaboration with Dr. Alexander Obukhov (Indiana University School of Medicine, IN, USA). Data were included in Figure 21 as amber bars. SF-11 elicited responses when applied intracellular, which indicated that this compound is either cell membrane permeant or that it is able to act on intra- and extracellular sites of TRPML3. SF-22 and SN-2 only activated when applied to the outside of the cells (Fig. 21), indicating that the compounds were acting exclusively extracellularly on TRPML3, and suggesting that the compounds are not plasma membrane permeable.

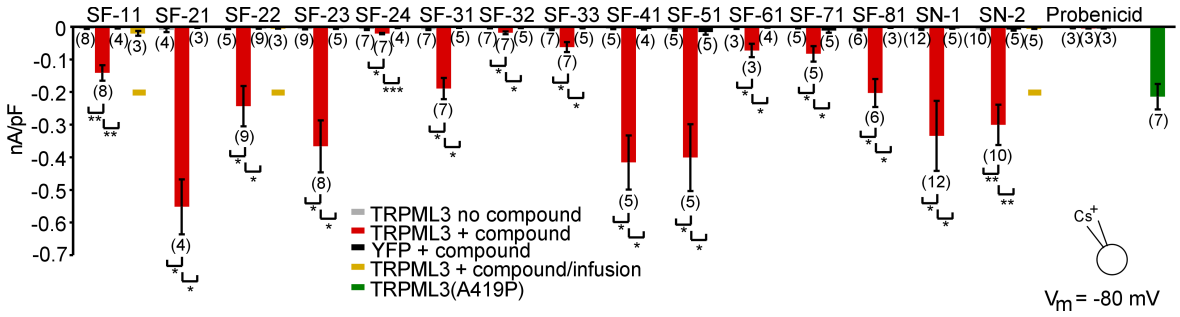

Figure 21: Identified compounds tested in whole-cell patch clamp experiments. Bar diagram showing average inward current densities at -80 mV of TRPML3-expressing HEK293 cells before (no compound) and after compound application (+ compound). The major cation in the pipette solution was 150 mM Cs^+ (pH 7.2). Cells transfected with constitutively active hTRPML3(A419P) isoform (green) were used as positive control, and cells transfected with pcYFP vector were used as negative controls. In general, three bars are shown for each test series (no compound and with compound on TRPML3-expressing cells and with compound on YFP-expressing cells). For compound SF-11, SF-22, and SN-2 intracellular application (infusion) is shown, resulting in a fourth bar (indicated in amber). Statistical comparisons of means were made using one-way ANOVA followed by Tukey's post test (mean values ±SEM, number in parentheses are the number of cells analyzed). *** indicates $p<0.0001$, ** indicates $p<0.001$, * indicates $p<0.01$. (Data were kindly provided by Dr. Christian Grimm.)

Table 7: Summery of data for the 15 tested TRPML3 selective small molecule activators obtained by calcium imaging and whole-cell patch clamp experiments. Fura-2 calcium imaging (Δ340/380) and whole-cell patch-clamp (nA/pF) data are mean values ±SEM (n≥3). Controls were YFP-expressing HEK293 cells.

ID	ΔF340/F380 TRPML3	ΔF340/F380 Control	nA/pF (-80mV) TRPML3	nA/pF (-80mV) Control
SF-11	0.72 ±0.05	- 0.005 ±0.002	- 0.14 ±0.02	- 0.004 ±0.001
SN-1	1.15 ±0.06	0.005 ±0.004	- 0.33 ±0.10	- 0.005 ±0.001
SF-21	1.38 ±0.10	0.033 ±0.008	- 0.55 ±0.08	- 0.003 ±0.001
SF-22	1.00 ±0.07	- 0.082 ±0.014	- 0.24 ±0.06	- 0.004 ±0.001
SF-31	1.00 ±0.10	- 0.011 ±0.001	- 0.19 ±0.03	- 0.003 ±0.001
SF-23	0.93 ±0.07	0.005 ±0.005	- 0.37 ±0.08	- 0.005 ±0.001
SF-41	0.99 ±0.07	0.015 ±0.001	- 0.42 ±0.07	- 0.007 ±0.002
SF-51	0.78 ±0.03	- 0.007 ±0.005	- 0.41 ±0.10	- 0.016 ±0.008
SF-32	0.52 ±0.05	- 0.008 ±0.005	- 0.02 ±0.01	- 0.003 ±0.001
SF-24	0.51 ±0.05	0.016 ±0.023	- 0.02 ±0.01	- 0.003 ±0.001
SF-33	0.65 ±0.10	- 0.007 ±0.016	- 0.06 ±0.02	- 0.003 ±0.001
SN-2	1.08 ±0.05	- 0.024 ±0.012	- 0.30 ±0.07	- 0.009 ±0.003
SF-61	0.56 ±0.03	- 0.005 ±0.006	- 0.07 ±0.01	- 0.002 ±0.001
SF-71	0.75 ±0.06	- 0.002 ±0.004	- 0.08 ±0.02	- 0.012 ±0.006
SF-81	0.62 ±0.05	- 0.005 ±0.016	- 0.20 ±0.03	- 0.002 ±0.001

3.2.5. Cochlear hair cells expressing TRPML3 do not respond to compound activators

TRPML3 immunoreactivity is detectable in the plasma membrane of cochlear hair cell stereocilia during the first weeks after birth (Di Palma et al., 2002; van Aken et al., 2008). In varitint-waddler mutant hair cells, constitutively active TRPML3(A419P) leads to Ca^{2+}-overloading, and resulting hair cell death. These observations suggested that TRPML3(A419P) is localized in the plasma membrane (Grimm et al., 2007; Kim et al., 2007; Nagata et al., 2008; Xu et al., 2007). Consequently, this led to the hypothesis that TRPML3-activating compounds should elicit a response in neonatal hair cells. Because rat cochlear hair cells are more robust for electrophysiological interrogation than murine cochlear hair cells, neonatal P5-P6 rat organs of Corti were isolated, and cochlear outer and inner hair cells were tested for response to application of TRPML3 activating compounds. Surprisingly, all compounds tested, including SF-21 and SN-2, which were most extensively investigated (>100 cells) at concentrations of up to 100 μM, did not elicit TRPML3 channel activity. The hair cell electrophysiology experiments were done in collaboration with Dr. Bifeng Pan (Stanford University). The result suggested that, albeit TRPML3 is located in the postnatal hair cell plasma membrane, it might be somehow modified or inhibited. TRPML3 is also expressed in epidermal skin melanocytes. Therefore, melanocytes were used to further investigate the discrepancy between activation of TRPML3 in transfected cells *versus* cells that natively express the channel protein.

3.2.6. Human epidermal melanocytes expressing TRPML3 show a robust response to compound SN-2

Mouse skin melanocytes also express TRPML3 (Di Palma et al., 2002). To test whether TRPML3 and other TRPML channels are present in human epidermal melanocytes, purified primary neonatal human epidermal melanocytes (HEM) were examined. RT-PCR analyses revealed robust expression of TRPML1, TRPML2, and TRPML3 (Fig. 22A). All 15 compounds were tested in calcium imaging experiments up to a concentration of 100 μM. Only SN-2 elicited robust responses at 100 μM and smaller responses after application of 30 μM. All the other compounds led to no or very small responses (Fig. 22B). Compounds SF-22, SF-71, and SF-81 did not show a Ca^{2+} increase after application to HEM, whereas all the others elicited a small response. NIH 3T3 cells do not

express TRPML3 natively (Fig. 22C), and therefore were used as a negative control. None of the compounds tested at 100 µM final concentration, including SN-2, showed a response (Fig. 22D). Compound SN-1 elicited a small transient increase of $[Ca^{2+}]_i$, which was considered non-specific because it also occurred when tested with NIH 3T3 cells. Fura-2 calcium imaging data obtained from HEM and NIH 3T3 were summarized in Table 8.

Table 8: Summery of calcium imaging data obtained in human epidermal melanocytes and NIH 3T3 cells in response to the application of 100 µM of various compounds. $[Ca^{2+}]_i$ increase in HEM and NIH 3T3 cells in response to application of 100 µM compounds. Fura-2 (Δ340/380) data are mean values ±SEM; n≥3 independent experiments with 20-30 cells.

ID	ΔF340/F380 HEM	ΔF340/F380 NIH 3T3
SF-11	0.016 ±0.01	-0.038 ±0.01
SF-21	0.063 ±0.02	0.005 ±0
SF-22	-0.037 ±0.01	-0.005 ±0
SF-23	0.073 ±0.02	-0.018 ±0
SF-24	0.042 ±0.01	-0.053 ±0.03
SF-31	0.018 ±0	0.005 ±0.01
SF-32	0.013 ±0	-0.018 ±0
SF-33	0.111 ±0.02	-0.029 ±0.02
SF-41	0.034 ±0.01	-0.012 ±0.01
SF-51	0.042 ±0.01	-0.002 ±0.01
SF-61	0.031 ±0.01	-0.049 ±0.01
SF-71	-0.03 ±0.03	-0.021 ±0
SF-81	-0.024 ±0.01	-0.011 ±0
SN-1	0.088 ±0.02	0.03 ±0.02
SN-2	0.473 ±0.04	-0.004 ±0.01

When melanocytes were transfected with a TRPML3-YFP expression vector, they showed robust increases in intracellular Ca^{2+} after compound application similar to the ones found in HEK293 or other tested cell lines such as NIH 3T3 cells with overexpressed TRPML3 (Fig. 22E,F). This control shows that primary melanocytes have no inherent inability to respond to activators. In addition, posttranslational modifications can be excluded; otherwise, the TRPML3-driven response upon activators would be much smaller in TRPML3-overexpressing melanocytes. Interestingly, overexpression of TRPML1-YFP in melanocytes resulted in strongly decreased responses after application of compound SN-2 when compared to non-transfected or YFP transfected melanocytes (Fig. 22E).

Based on these results, it can be hypothesized that presence of TRPML3 in the plasma membrane might be limited or tightly regulated in primary melanocytes and also in

sensory hair cells (see previous section). Native TRPML3 might be in a state that renders it little or non-responsive to most compounds.

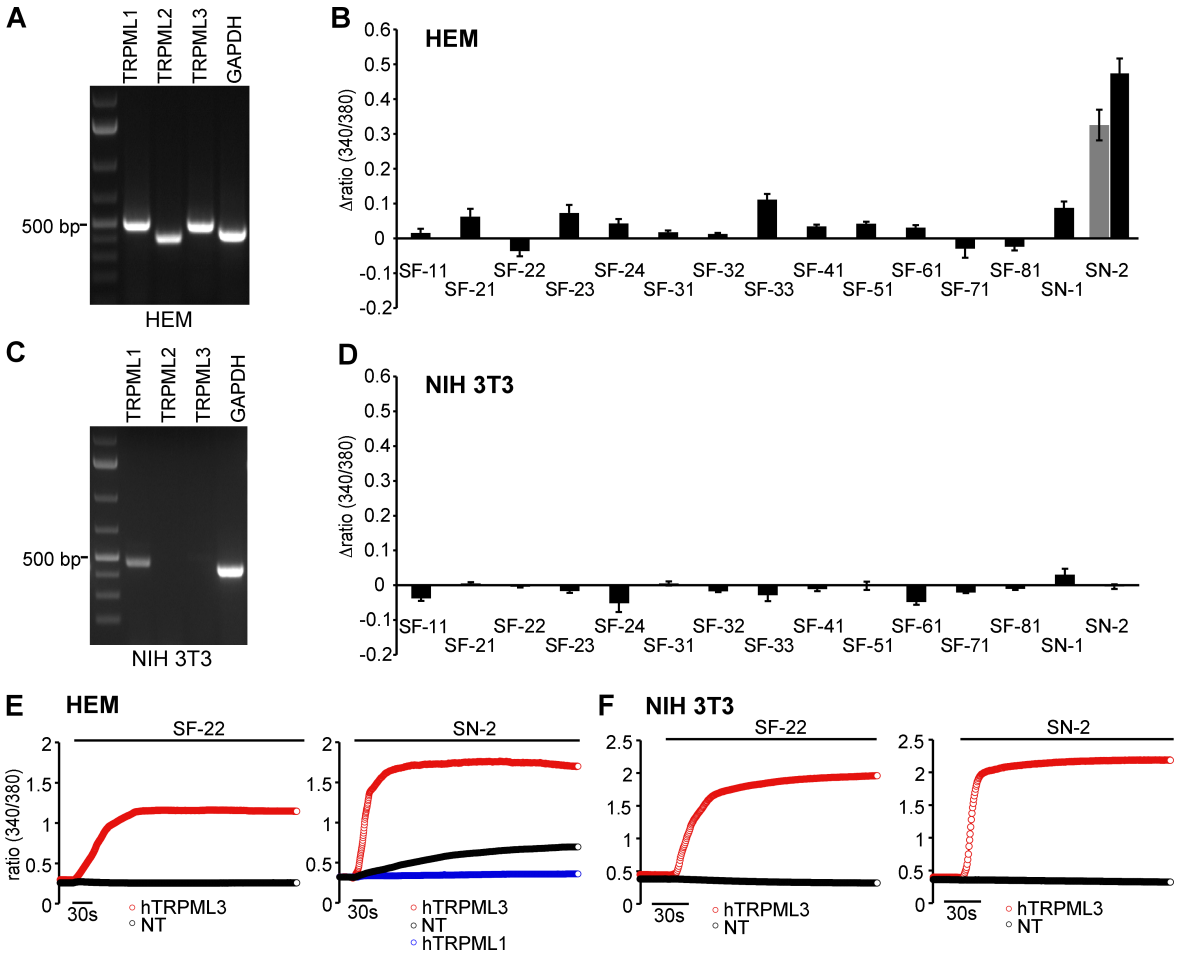

Figure 22: Compound effect on human epidermal melanocytes. A: RT-PCR analysis of TRPML channel expression in human epidermal melanocytes (HEM). All TRPML channels are expressed in melanocytes. Shown is amplified cDNA representing TRPML1 (500 bp), TRPML2 (411 bp), TRPML3 (487 bp), and GAPDH as a control (444 bp). **B:** $[Ca^{2+}]_i$ increase in HEM cells in response to application of 100 µM compounds. Responses to SN-2 are shown for 30 µM (grey bar) and 100 µM. Bar diagrams represent average $[Ca^{2+}]_i$ levels 5 min after compound application relative to the respective Ca^{2+} level before application. Mean values ±SEM; n≥3 independent experiments with 20-30 cells. **C:** RT-PCR analysis of TRPML channel expression in mouse NIH 3T3 cells demonstrated only TRPML1 (470 bp) and GAPDH (442 bp) transcripts, but not TRPML2 (500 bp) and TRPML3 (550 bp). **D:** Calcium imaging experiments as described in (B) showing compound effect at 100 µM on NIH 3T3 cells. **E:** Calcium imaging experiments showing $[Ca^{2+}]_i$ increases in HEM transfected cells with hTRPML3-YFP or non-transfected cells (NT) upon application of SF-22 and SN-2 at 30 µM. Transfected cells with hTRPML1-YFP did not elicit a response after application of compound SN-2. **F:** Calcium imaging experiments as described in (E) showing compound effect on non-transfected (NT) NIH 3T3 cells or transfected cells with hTRPML3-YFP.

3.2.7. Dominant negative variant D458K inhibits native TRPML3 in melanocytes

The effect of SN-2 on melanocytes raised the question whether this compound acts nonspecifically. In calcium imaging experiments, it was shown that none of the other tested TRP channels beside TRPML3 responded to SN-2, including the related TRPML2 and TRPML1(NC) isoforms (Fig. 20J). As mentioned earlier, SN-2 only activates when applied to the outside of the cells (Fig. 21). It can therefore be concluded that its action on melanocytes is based on an interaction with an extracellular site. For further investigation, a dominant negative TRPML3 mutant isoform was utilized (Kim et al., 2009). This mutant displays an asparagine to lysine substitution at amino acid position 458 (D458K) in the pore region between TM5 and TM6 of TRPML3 (Fig. 23A). It has been shown that the dominant negative mutant has an effect in reducing endocytosis and autophagy (Kim et al., 2009). First, it was confirmed that TRPML3(D458K) completely eliminated responses to activators SF-21 and SN-2 when transiently coexpressed with wild-type TRPML3 in HEK293 cells (Fig. 23B,C). Control cells were cotransfected with wild-type TRPML3 and TRPML2 or TRPV2. Coexpression of TRPML2 and TRPV2 did not show a decrease of TRPML3 responsiveness in HEK293 cells (Fig. 23B,C). These controls confirmed specifity of the dominant negative TRPML3(D458K) isoform. Expression of the dominant negative TRPML3(D458K) in primary melanocytes, however, completely abolished the effect of SN-2 activation (Fig. 23D). This result demonstrated that the Ca^{2+} increase elicited by SN-2 is inhibited by coexpression of the dominant negative TRPML3 isoform. Thus, the SN-2 effect appears to be specific and TRPML3 channels are very likely present in the plasma membrane of primary melanocytes.

In the following chapter, I will focus on mechanisms with potential impact on TRPML3 localization and function. These mechanisms could decrease compound responsiveness of native TRPML3 in sensory hair cells or skin melanocytes.

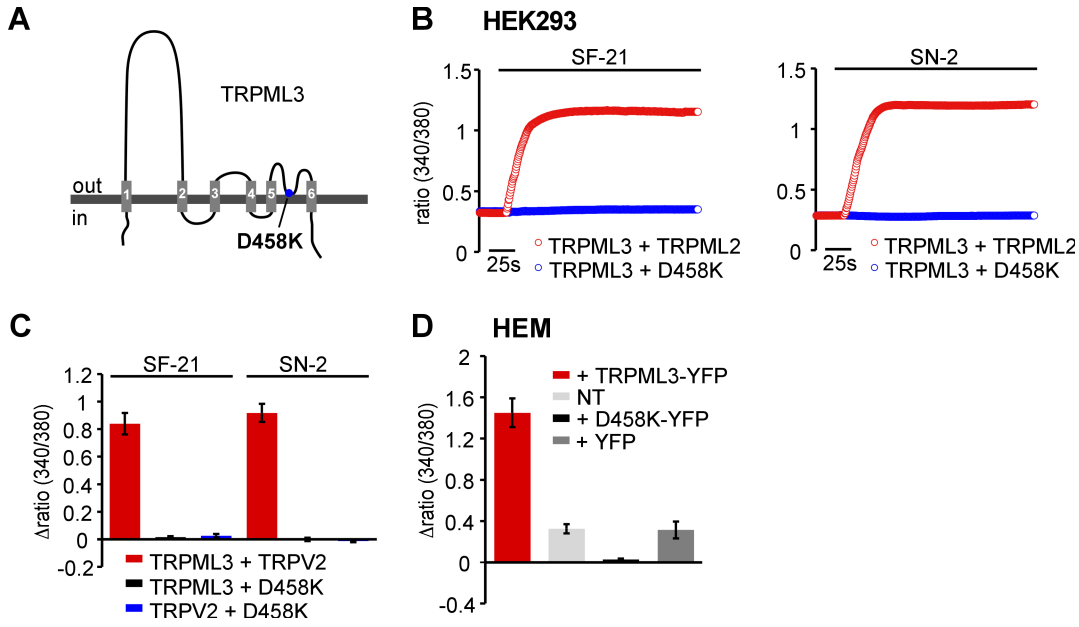

Figure 23: Effect of dominant negative TRPML3(D458K) mutant. A: Schematic drawing of TRPML3 showing position of D458K in the pore region between TM5 and TM6. **B:** Calcium imaging experiments on HEK293 cells transiently expressing TRPML3 and dominant negative TRPML3(D458K) or TRPML2 as a control. Shown are responses to 10 µM of compounds SF-21 and SN-2. **C:** Shown are HEK293 cells cotransfected with TRPML3 and TRPV2, TRPML3 and TRPML3(D458K), and TRPV2 and TRPML3(D458K) in response to 10 µM of compounds SF-21 and SN-2. Bar diagram represent average $[Ca^{2+}]_i$ levels 2 min after compound application relative to the respective Ca^{2+} level before application (mean values ±SEM, n≥3 independent experiments with 20-30 cells). **D:** Calcium imaging experiments on HEM transfected with TRPML3, dominant negative TRPML3(D458K), and YFP control. NT = non-transfected cells. Bar diagram represents average $[Ca^{2+}]_i$ levels 4 min after compound SN-2 application (30 µM) relative to the respective Ca^{2+} level before application (mean values ±SEM, n≥3 independent experiments with 5-10 cells).

3.2.8. Coexpression of TRPML1 decreases compound responsiveness of TRPML3

HEK293 cells transiently transfected with hTRPML1 and hTRPML3 alone showed predominant localization of TRPML1 in intracellular compartments, whereas TRPML3 was detected in intracellular vesicles as well as in the plasma membrane (Fig. 5, *Introduction*). When hTRPML1 was coexpressed with hTRPML3, the subcellular localization of TRPML3 changed: more TRPML3 protein was visible in intracellular compartments where it overlapped with TRPML1 expression. Nearby cells that did not express or only expressed small amounts of TRPML1 still showed clear plasma membrane localization of TRPML3 (Fig. 24). This finding, which suggests an interaction between TRPML1 and TRPML3, is supported by fluorescence resonance energy transfer (FRET) experiments using TRPML-CFP and TRPML-YFP fusion proteins, which show that TRPML protein subunits are able to heteromerize with each other in overexpression studies (Venkatachalam et al., 2006; Curcio-Morelli et al., 2009; Grimm et al., 2010; for a

review, see Puertollano and Kiselyov, 2009). Hence, presence of TRPML1 impacts the subcellular localization of TRPML3, which led to the hypothesis that TRPML1 can regulate the ratio of plasma membrane concentration *versus* intracellular location of TRPML3 (Venkatachalam et al., 2006; reviewed in Cheng et al., 2010). On the other hand, coexpression in cells or tissue, which usually overburdens cells with recombinant protein, does not necessarily mean that endogenous TRPML channels are targeted to the same subcellular locations (Kim et al., 2009; Zeevi et al., 2009).

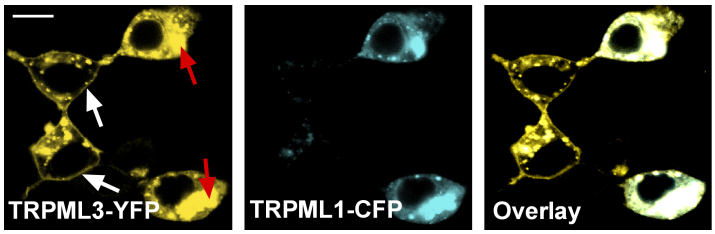

Figure 24: Representative micrographs of HEK293 cells expressing hTRPML1-CFP and hTRPML3-YFP fusion proteins. Shown are four cells that all express hTRPML3-YFP. Two of these cells also express hTRPML1-CFP. White arrows indicate expression of TRPML3 in the plasma membrane, when cells only express small amounts of TRPML1. Red arrows indicate intracellular TRPML3 protein aggregations, when coexpressed with TRPML1 in one cell. Scale bar = 15 µm.

If TRPML channels interact and TRPML1 is able to take TRPML3 out of the plasma membrane, than I would expect that coexpression of TRPML1 would decrease compound responsiveness of TRPML3. HEK293 cells transiently cotransfected with hTRPML1 and hTRPML3 were tested in calcium imaging experiments (Fig. 25). With all four compounds tested (SF-21, SF-22, SF-23, and SN-2), a robust reduction of the intracellular Ca^{2+} responses was observed when TRPML1 was coexpressed. Coexpression with mTRPML2 or mTRPV2 did not result in decrease of TRPML3 responsiveness (Fig. 25). For these experiments, either fusion proteins with YFP were used, or proteins tagged with a hemagglutinin tag (HA). HA is invisible in calcium imaging experiments and cells cannot be selected for the presence of both ion channel proteins. Therefore, the selected cells may not express both proteins at the same time, or one construct is less expressed than the other is. To circumvent any irregular expression pattern of both players, I swapped the tags and tested again (Fig. 25E-H) with the result that the tags did not show any irregularities in expression. As expected, these experiments confirmed that TRPML1 is indeed able to reduce the increase of intracellular Ca^{2+} in TRPML3 cotransfected cells.

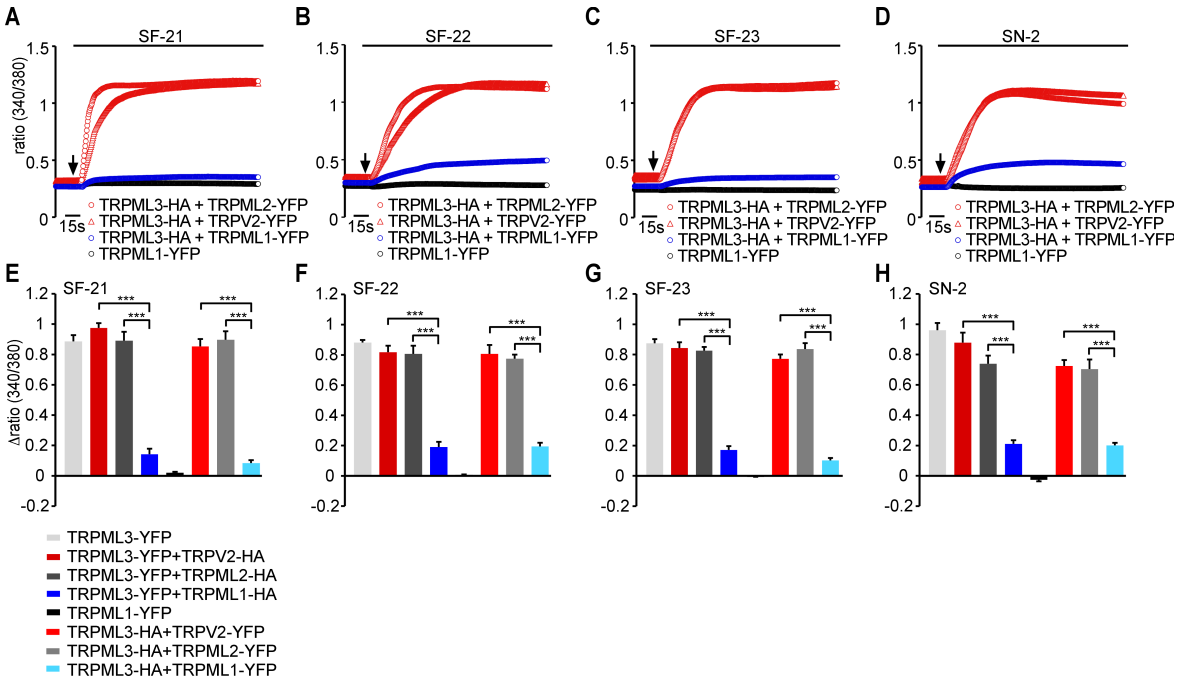

Figure 25: Coexpression of TRPML1 with TRPML3 results in decreased activation effects of TRPML3 agonists SF-21, SF-22, SF-23, and SN-2. A-D: Shown are calcium imaging measurements of $[Ca^{2+}]_i$ changes in HEK293 cells coexpressing TRPML3-HA with TRPML1-YFP, TRPML2-YFP (control), or TRPV2-YFP (control) and TRPML1-YFP alone in response to 10 µM compounds. Mean values, n≥3 independent experiments with 20-30 cells each. **E-H:** Bar diagrams represent average $[Ca^{2+}]_i$ levels 2 min after compound application relative to the respective Ca^{2+} level before application. Shown are values of cotransfected HEK293 cells either with TRPML3 tagged with YFP and TRPV2-HA, TRPML2-HA and TRPML1-HA, or TRPML3-HA with TRPV2-YFP, TRPML2-YFP, and TRPML1-YFP and TRPML1-YFP alone. Comparison of both ways showed no irregularities. Statistical comparisons of means were made using one-way ANOVA followed by Tukey's post test (mean values ±SEM, n≥3 independent experiments with 20-30 cells), ***p<0.0001.

3.2.9. Coexpression of TRPML1(NC) mutant isoform with TRPML3

Further, I hypothesized that coexpression of TRPML3 with a membrane-localized TRPML1 isoform will result in a smaller reduction of TRPML3 response upon compound application than coexpression with wild-type TRPML1. To investigate the effect of TRPML1 on TRPML3 trafficking, TRPML1 mutants with a plasma membrane instead of an endosome/lysosome localization profile were generated. This was achieved by removal of either or both of the two TRPML1-specific dileucine motifs (lysosomal targeting site = LTS) that are located in the N- and C-termini (Miedel et al., 2006; Venkatachalam et al., 2006; Vergarajauregui and Puertollano, 2006) (Fig. 26A,B). All three hTRPML1 mutant isoforms were C-terminally tagged with YFP and transiently overexpressed in HEK293 cells (Fig. 26C). Only when both LTSs were absent, the resulting TRPML1(NC) mutant isoform was detected in the plasma membrane. TRPML1(N) resulted in a similar

intracellular localization pattern as wild-type TRPML1. TRPML1(C) was mainly located intracellular and only a few cells showed a faint signal for the channel protein in the plasma membrane (Fig. 26C). Based on these results of the localization studies, TRPML1(NC) was used for further investigations.

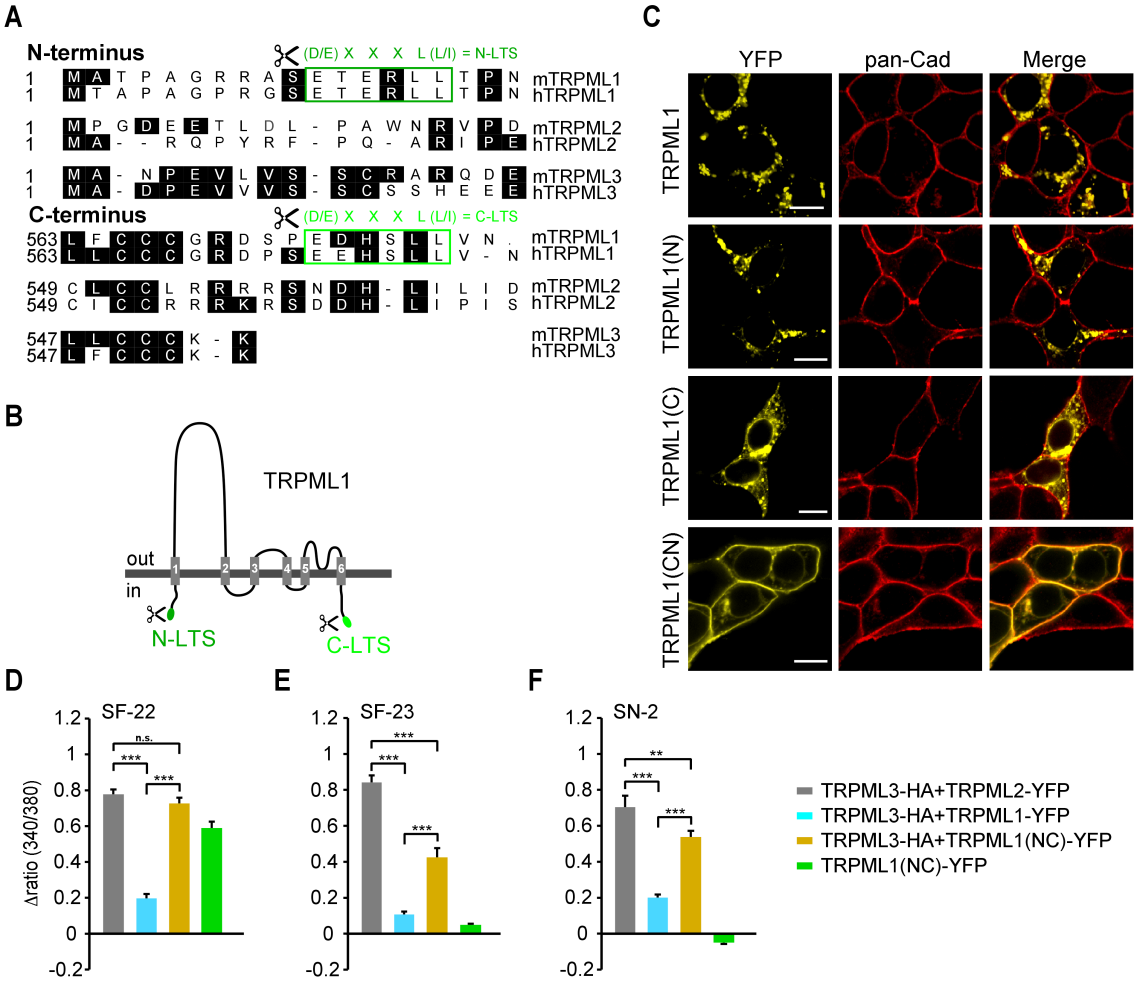

Figure 26: TRPML1 lacking lysosomal targeting motifs displays reduced functional suppression of TRPML3 agonist effect. A: Protein sequence comparison of the N- and C-termini of TRPML channels. Different lysosomal targeting sequence (LTS) motifs are labeled in green. **B:** Simple drawing of TRPML1 topology indicating the position of the LTS motifs that were removed in mutant TRPML1 isoforms. **C:** Confocal micrographs of HEK293 cells overexpressing C-terminal YFP fusion constructs of wild-type TRPML1 and mutant isoforms TRPML1(N), TRPML1(C), and TRPML1(NC) (yellow). The plasma membrane is visualized with pan-Cadherin (pan-Cad) antibodies (red). Scale bars = 10µm. **D-F:** Calcium imaging results showing relative $[Ca^{2+}]_i$ increases after application of compound SF-22, SF-23, and SN-2 in HEK293 cells coexpressing TRPML3-HA with wild-type or mutant isoform of TRPML1-YFP, or coexpressing TRPML3-HA with TRPML2-YFP (controls as shown in Fig. 25F-H), and TRPML1(NC)-YFP alone. Shown are mean values ±SEM, n≥3 independent experiments with 20-30 cells each. ***p<0.0001, **p<0.001, n.s. not significant.

The hypothesis was that the coexpression of TRPML3 with TRPML1(NC) would result in a smaller reduction of TRPML3 response upon compound application than coexpression with wild-type TRPML1. Indeed, TRPML1 lacking both LTS motifs showed higher response levels upon agonist application than coexpression with wild-type TRPML1 (Fig. 26D-F). Furthermore, we observed that TRPML1(NC) mutant isoform, but not wild-type TRPML1, can be activated by compound SF-22 (Fig. 26D), a compound that is not cell permeable (Fig. 21). This control experiment shows that TRPML1(NC) is targeted to the plasma membrane and that this channel is functional when activated by extracellular application of SF-22. In addition, it confirmed that wild-type TRPML1 is absent from the plasma membrane. Coexpression of TRPML3 with TRPML2, on the other hand, does not lead to reduced responsiveness to compound SF-23 and SF-22 and only to slight, but not significant reduction, in response to SN-2. Based on the results, it can be concluded that wild-type TRPML1 influences the subcellular localization of TRPML3 thereby affecting the responsiveness of cells expressing TRPML3 to compound application, which might be an underlying cause for the observed lack of responsiveness or reduced response of melanocytes.

3.2.10. Suppression of native TRPML1 in human epidermal melanocytes

Generally, the data above confirmed the hypothesis that interaction with TRPML1 generates TRPML3/TRPML1 heteromers that preferentially localize to intracellular compartments *in vitro*. The question is whether this interaction is relevant in cells that natively express TRPML3 such as HEM. Specific small hairpin RNA (shRNA) was used to knockdown native TRPML1 in HEM. ShRNA binds to homologous RNA and decreases their activity, for example by preventing mRNA from producing a protein or by inducing the destruction of the particular mRNA. It was shown that shRNA 1208 is able to strongly downregulate overexpressed human TRPML1 (Samie et al., 2009, Fig. 27A,B). This shRNA was kindly provided by Dr. Math P. Cuajungco (California State University, Fullerton, CA, USA). The efficiency of the shRNA 1208 was tested in transfected HEK293 cells. Wild-type hTRPML1-YFP and hTRPML1(C1218T)-YFP were transfected in a ratio 1 to 3 with shRNA 1208. hTRPML1(C1218T) was used as a control that should not be affected by shRNA 1208 because of a nucleotide exchange C to T, which introduced a silent mutation in the binding site of shRNA 1208. Therefore, shRNA 1208 should not bind and consequently not downregulate hTRPML1(C1218T). However, if a downregulation would occur, this shRNA were to be considered as unspecific and would

not be used in my experiments. Confocal imaging and RT-PCR analyses revealed that only wild-type TRPML1 but not the mutant, is specifically downregulated by shRNA 1208 (Fig. 27A,B). This experiment proved the specificity of this particular shRNA. TRPML1 mRNA was still detected by RT-PCR, but its translation was disrupted (Fig. 27A,B). In native cells, however, expression of shRNA 1208 to TRPML1 did not affect responsiveness to compound activation (Fig. 27C). Although this lack of responsiveness could be due to incomplete inhibition of TRPML1 expression, despite the efficacy of the knockdown in heterologous expression situations (Miedel et al., 2008; Samie et al., 2009), it revealed that the regulation of TRPML3 surface expression by TRPML1 might not determine compound responsiveness of TRPML3 in HEMs.

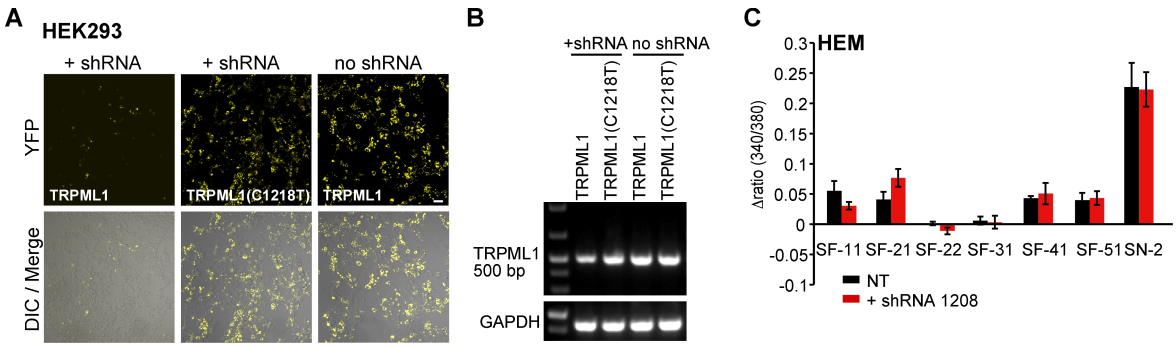

Figure 27: TRPML1 knockdown with specific shRNA. A: Confocal micrographs of HEK293 cells overexpressing wild-type TRPML1-YFP or TRPML1-YFP mutant (C1218T silent mutation) in presence or absence of TRPML1 shRNA 1208. Scale bar = 50 µm. **B:** RT-PCR analysis of TRPML1 channel (500 bp) expressing in transfected HEK293 cells (TRPML1-YFP and TRPML1(C1218T)-YFP with and without shRNA). GAPDH (444 bp) was used as a loading control. **C:** Measurements of $[Ca^{2+}]_i$ changes in HEM cells expressing shRNA 1208 (red bars) or non-transfected HEM (black bars) upon application of selected TRPML3 activating compounds from five different scaffolds (SF-11, SF-21, SF-22, SF-31, SF-41, and SF-51) and singleton SN-2 at 30 µM. Mean values ±SEM, n≥3 independent experiments with 5-10 cells. An expression vector for YFP was cotransfected with the shRNA 1208 in all cases for identification of the transfected cells.

3.2.11. Effect of endocytosis modulation on TRPML3 compound responses

Beside a possible regulation of TRPML3 plasma membrane localization by TRPML1, other plausible regulation mechanisms have recently been explored (Kim et al, 2009). The authors found that a dominant negative dynamin mutant (DynK44A) increased plasma membrane expression of TRPML3, which led them to conclude that TRPML3 recycles or shuttles between the plasma membrane and intracellular compartments via a dynamin dependent endocytotic pathway. Based on this finding, I would expect that increase of dynamin-mediated endocytosis would decrease the number of TRPML3 channels in the plasma membrane, whereas inhibition of dynamin would increase responsiveness to TRPML3 activators. To test this hypothesis, wild-type dynamin was coexpressed with TRPML3 in HEK293 cells.

Indeed, a significant reduction was found in response to selected weak (SF-24) and strong (SN-2) TRPML3 activators compared to control experiments (Fig. 28A-D). When the dominant negative K44A mutant of dynamin was coexpressed with TRPML3, consistently small, but overall not significant response increases were observed (Fig. 28C,D). Expression of dynamin and dynamin K44A mutant alone did not elicited a Ca^{2+} change in HEK293 cells in response to compounds. When dynamin was expressed in human melanocytes, a reduction of the response to SF-11, SF-51, and in particular to SN-2 was found (Fig. 28E), indicating that the responsive channel is affected by increased endocytosis. However, when a dominant negative dynamin K44A variant was expressed in HEM, no change in response levels to TRPML3 activating compounds were detected (Fig. 28E).

In contrast to their effects on overexpressed TRPML3 channel activation in HEK293 cells, neither TRPML1 knockdown nor block of dynamin-mediated endocytosis appeared to significantly increase responses in human melanocytes natively expressing TRPML3, suggesting that these manipulations were not strong or sufficient enough, or that alternative mechanisms are involved in the regulation of TRPML3.

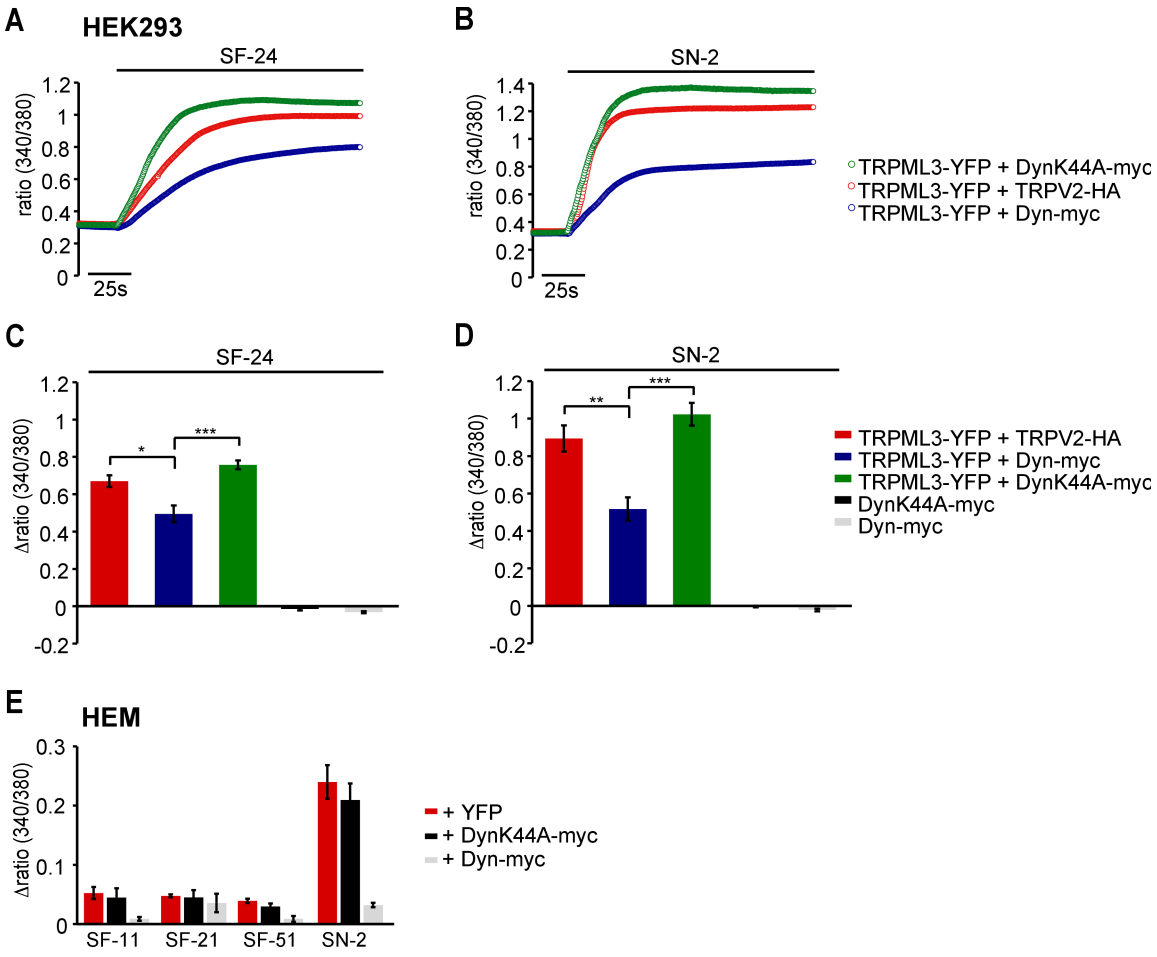

Figure 28: Effect of dynamin and dynamin K44A mutant on TRPML3 activation on HEK293 cells and melanocytes. A,B: Measurements of $[Ca^{2+}]_i$ changes in HEK293 cells coexpressing TRPML3 with dynamin (Dyn), dynamin K44A dominant negative mutant (DynK44A), or TRPV2 (control) in response to 10 µM SF-24 (A) or SN-2 (B). **C,D:** Bar diagrams represent average $[Ca^{2+}]_i$ levels 2 min after compound application (SF-24 or SN-2) relative to the respective Ca^{2+} level before application. Shown are values of cotransfected HEK293 cells either with TRPML3 and TRPV2, Dyn or DynK44A, and Dyn and DynK44A alone. Statistical comparisons of means were made using one-way ANOVA followed by Tukey's post test (mean values ±SEM, n≥3 independent experiments with 20-30 cells). **E:** Calcium imaging results showing changes in $[Ca^{2+}]_i$ in HEM transfected with either Dyn, DynK44A, or YFP (control) in response to application of TRPML3 activating compounds SF-11, SF-21, SF-51, and singleton SN-2 at a concentration of 30 µM, each (mean values ±SEM, n≥3 independent experiments with 5-10 cells).

3.3. Genetic inactivation of *Trpml3* does not lead to hearing and vestibular impairment in mice

The most promising approach to elucidate the physiological role of TRPML3 *in vivo* is the creation of a conditional *Trpml3* inactivation in mice. TRPML3, on the one hand, has clearly been proven to be expressed in cells of the inner ear and the varitint-waddler mutations of the channel cause hair cell degeneration and deafness. On the other hand, hair cell death-mediated hearing loss, due to a constitutive active ion channel, is not sufficient to justify a function in the hearing process itself. How would loss of function of TRPML3, as in a knockout, affect hearing and balance? In this chapter, the conditional *Trpml3* inactivation will be presented. The analysis of the hearing and vestibular phenotype in mice with conditionally inactivated *Trpml3* has recently been published in *PLoS ONE* (Jörs et al., 2010).

3.3.1. Generation of a floxed *Trpml3* allele (*Trpml3^{loxP}*)

3.3.1.1. Strategy and introduction of individual elements

TRP channel knockouts have successfully been generated through targeted deletion of the genomic region encoding the presumptive pore-loop domain of the ion channel (Kwan et al., 2006; Bautista et al., 2006; Moqrich et al., 2005). In contrast to traditional knockouts, conditional gene modification using Cre-lox or Flp-FRT technology allows the gene of interest to be disrupted in only a subset of tissues/cells or only at a particular time, circumventing lethality (Dymecki, 2000). Because gene targeting can be controlled both spatially and temporally, the function of a given gene can be studied in the desired cell types and at a specific time point. Exon 11 of *Trpml3* encodes for the region between TM5 and TM6 including the pore-loop, and TM6 itself. Thus, it is expected that deletion of exon 11 leads to an effective inactivation by destroying the core domain of TRPML3, the pore (Fig. 29A). The *Trpml3* gene is localized on chromosome 3 in mice (MGI: 1890500 or Ensembl Gene ID: ENSMUSG00000036853). The targeting construct consisted of two arms of genomic DNA: the 5' arm (left arm = LA) and the 3' arm (right arm = RA). When introduced into embryonic stem (ES) cells, the DNA of the two arms will undergo site-specific recombination with their matching sequences on one chromosome. The arms envelop a FRT-flanked neomycin phosphotransferase-encoding gene (*neo^{R}*) and the *loxP*-flanked intron-exon 11 cassette. In a successful targeting event, the genomic DNA

between the regions of homology on mouse chromosome 3 will be replaced with the *neo*^{R} selection cassette and exon 11 targeted sequences (Fig. 29B).

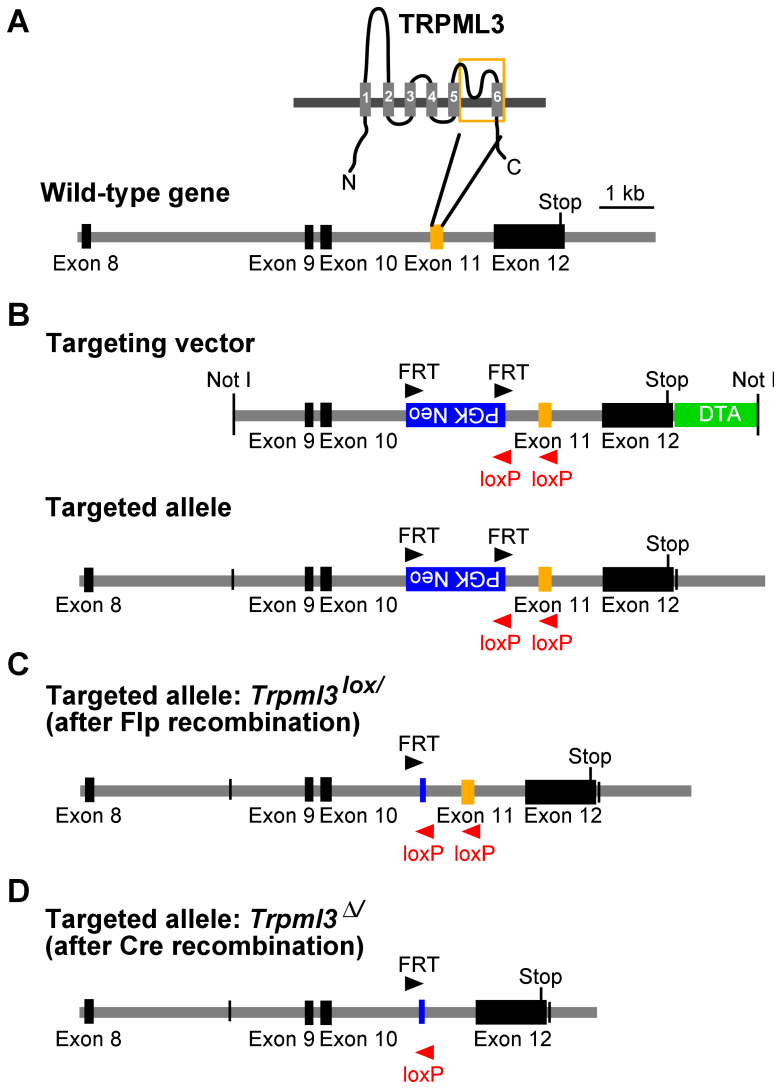

Figure 29: Targeting strategy for disruption of the *Trpml3* gene. A: Transmembrane protein domains are depicted by grey bars and numbered from 1-6. Orange frame indicates the part of the TRPML3 protein that is encoded by exon 11, which will be deleted (pore loop and TM6). Exons are shown as black and orange bars on the schematic genomic map below. **B:** Shown are the targeting vector and the targeted allele after homologous recombination. The blue bar represents the PGK promoter-driven *neo*^{R} expression cassette, which was used as positive selection. The DTA cassette, used for negative selection, is shown in green. The black and red arrowheads symbolize position and orientation of FRT and *loxP* sites. The targeting vector containing both FRT-flanked *neo*^{R} marker and *loxP*-flanked exon 11 was introduced into ES cells. **C:** Targeted allele after Flp site-specific recombination in ES cells, resulting in excision of the *neo*^{R} cassette, and leaving one FRT site behind. **D:** Excision of exon 11 using Cre site-specific recombinase, resulting in disruption of the *Trpml3* gene.

Cre recombinase (*c*auses *re*combination), a site-specific integrase isolated from the P1 bacteriophage, catalyzes recombination between two of its consensus *loxP* (locus of cross-over (*x*) in P1) DNA recognition sites (Sauer and Henderson, 1998). These *loxP* sites are 34 bp in length, consisting of two 13 bp palindromic sequences surrounding a central sequence of 8 bp, which determines the directionality of the *loxP* site (Fig. 30A). Two *loxP* sites were placed in *trans* orientation on either side of *Trpml3* exon 11. In presence of Cre recombinase, this configuration results in excision of exon 11 (Fig 30B). Flp recombinase was utilized with a similar strategy. In contrast to the *loxP* site, the symmetry elements of the FRT site contain only a single bp difference (Dymecki, 2000). Although few lines of mice have been generated to express Flp *in vivo*, this system is very useful for the *in vitro* removal of the selection gene from the targeted gene at the ES cell stage (Fig. 29C). The selection cassette has to be removed because its presence in an intron can result in disruption of the regulation and splicing of the targeted gene, or the expression of neighboring genes can be altered by the promoter elements present in selection cassettes (Dymecki, 2000). This alteration of gene function could produce an unwanted or even lethal phenotype (Scacheri, 2001). In the targeting construct, neo^R was used as a positive selection marker, which allowed the selection of clones that have integrated the targeting construct. The housekeeping gene promoter PGK (Phosphoglycerine kinase) was driving the neo^R gene. Besides exactly integrating into the targeted gene, the targeting construct can also integrate into random loci, a phenomenon that happens quite frequently (Dymecki, 2000). Any integration event, random or specific, however, confers drug resistance to the cell. After growing the transfected cells under selection, the challenge is to screen enough clones to find the rare homologous recombination events. The rate of correct targeting events, also called the targeting frequency, is generally in the range of ~1%. Negative selection markers can yield an up to 10-fold enrichment of correct targeting events. The negative selection drug simply enriches for the desired homologous recombination event over random integrations by killing cells, which have retained a copy of the negative selection gene. It is present when homologous recombination did not take place (Dymecki, 2000). Diphtheria toxin A (DTA) was used as a negative selection marker (Fig. 29B). With its own promoter, DTA was expressed in cells with random integration, causing them to die. In case of correct recombination into the genome, DTA was not integrated into the genome. After selection, the neo^R cassette was removed by Flp recombinase, before the ES cells were injected into host blastocysts to generate mice. With this system, the chimeric offspring contained only a minimal genetic modification, the

addition of two *loxP* sites and one FRT site, in the gene of interest (Fig. 29C). The last critical step is the Cre site-specific recombination. As mentioned above, exon 11 of *Trpml3* gene is flanked by *loxP* sites. The recombination allows the completely removal of exon 11, which would result in production of either a mutated or a truncated protein, or no protein at all (Fig. 29D).

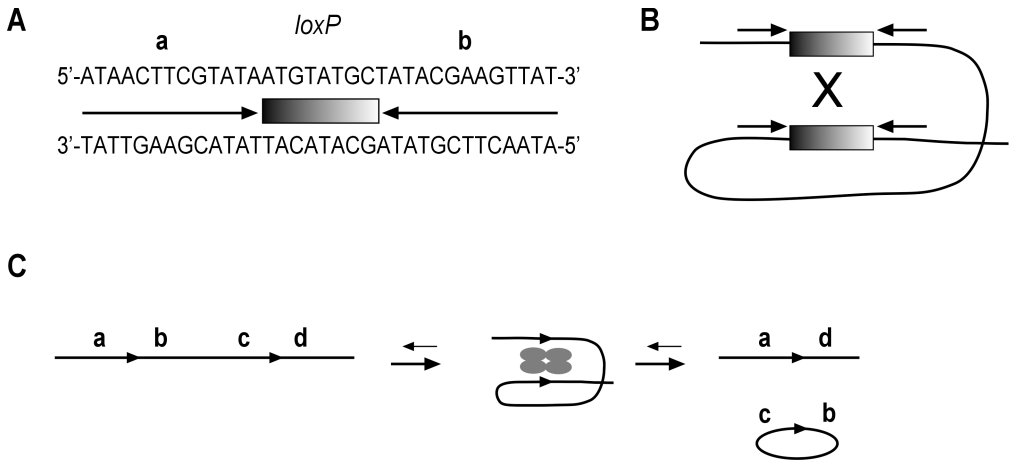

Figure 30: Cre recombinase target site: *loxP*. A: *LoxP* target site contains inverted 13 bp symmetry elements (horizontal arrows a and b) flanking an 8 bp A:T-rich non-palindromic core (shaded rectangle). **B:** Synaptic complex formed between recombinase molecules and two directly orientated target sites. X: cross-over. **C:** Shown is recombinase deletion reaction catalyzed by Cre recombinase. Black rectangles indicate recombinase recognition target sites and black lines the chromosomal DNA with orientation indicated by the letters a, b, c, and d. Grey ovals represent recombinase monomers, which bind to symmetry elements in target site. The reaction is reversible, which is indicated by arrows between recombinase substrates and products. Directly orientated sites lead to an excision of a circular molecule. In final products, the symmetry arms of the two target sites have been exchanged. (Adapted from Dymecki, 2000.)

3.3.1.2. Step 1: Cloning of the targeting vector

Each step of generating the conditional *Trpml3* knockout will be discussed in more detail, including pitfalls and troubleshooting. The *Trpml3* targeting vector was initially assembled by Dr. Christian Grimm. His cloning strategy is summarized in the *Materials and Methods* section 2.1.8. and Table 1. To PCR-amplify all *Trpml3* genomic sequences for the targeting construct, he used genomic DNA (129sv/svj), provided by the Stanford transgenic research center (http://med.stanford.edu/transgenic). This targeting vector needed to be modified after a series of initial targeted recombination experiments with embryonic stem cell revealed incomplete recombination events into the genomic site. The modification of the targeting vector was performed by myself, and will be discussed in the next paragraph.

3.3.1.3. Incomplete integration of the *Trpml3* targeting construct and troubleshooting

After screening of neomycin positive ES cell clones, the lack of the second *loxP* site was discovered by sequence analysis (Table 4). A review of the targeting vector revealed a possible scenario: The 3' arm of homology with 1700 bp was too short in comparison to the 5' arm with 3027 bp and the targeting intron-exon 11 sequence with 1473 bp. The illustration below is showing the expected and occurred homologous recombination into the ES cell genome (Fig. 31A,B). The homologous recombination was incomplete and did not occur between the 5' arm (LA) and 3' arm (RA) and its homologous sequences in the genomic *Trpml3* locus, but rather between the LA and targeted exon 11 sequences, resulting in the omission of the second *loxP* site. In addition, the existence of rather large non-homologous regions such as the neo^R selection cassette (1747 bp) within the targeting construct could increase the likelihood of incomplete recombination events (Dymecki, 2000). This raised the question how the targeting construct could be modified in a fast and efficient way to increase the likelihood of correct and complete integration into the genomic *Trpml3* locus. To exchange the existing 3' arm of homology with a longer 3' arm using the previously used restriction endonuclease *Sma*I was unfortunately not an option. The targeting vector would have been endonucleolytically digested into several pieces. Another option was to use QuikChange site-directed mutagenesis. This strategy included deletion of the existing second *loxP* site and insertion of a new *loxP* site plus the unique restriction site *Pac*I immediately downstream of exon 11 in the intron sequence (Table 2 and 2.2.1.2.), paying attention to splice acceptor, donor, and branch sites, respectively. *Pac*I was inserted to facilitate the identification of correct mutagenesis and ES cell clones. The length of the 3' arm was increased by 537 bp, and the length of the targeted *Trpml3* exon 11 segment was decreased by 569 bp (Fig. 31C).

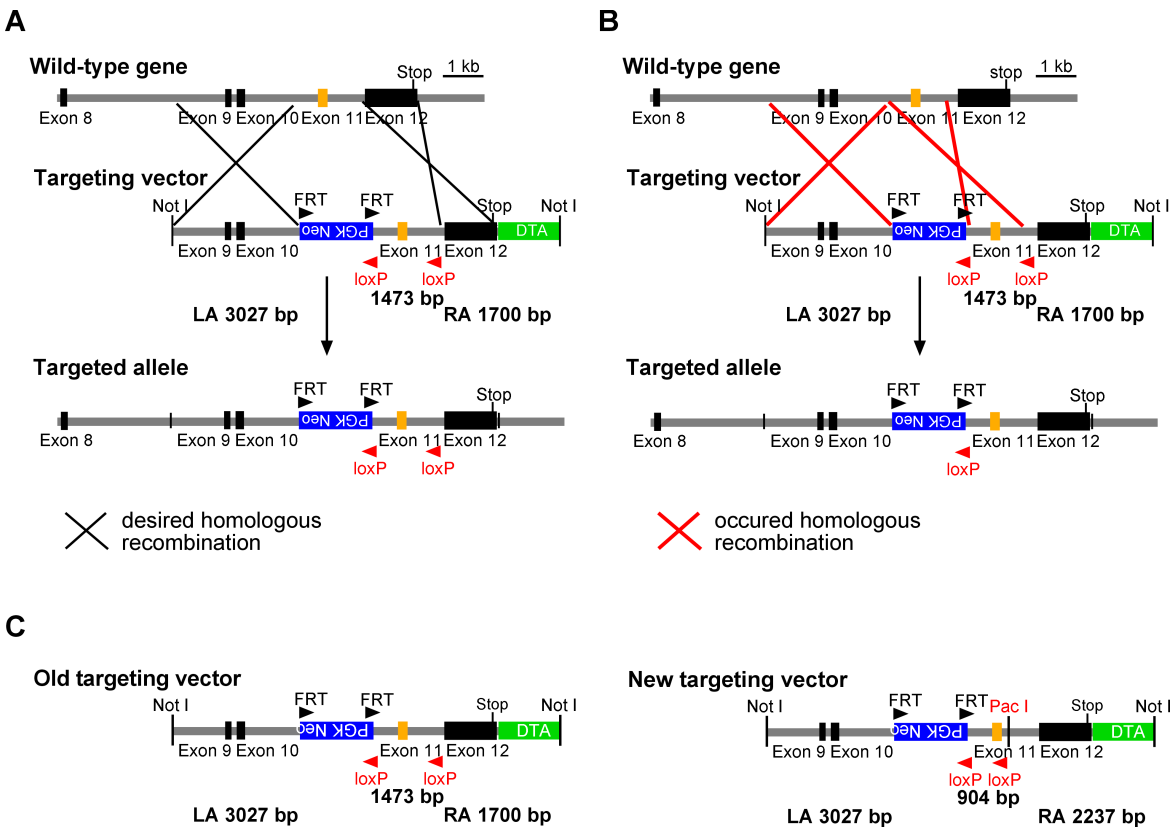

Figure 31: Homologous recombination into the genomic *Trpml3* locus. A: Showing expected homologous recombination. 5' arm (left arm = LA) and 3' arm (right arm = RA) of homology undergo recombination with their matching sequences in the *Trpml3* locus, carrying both cassettes (FRT-flanked *neo*^{R} and *loxP*-flanked intro-exon 11 sequence) with them. **B:** Homologous recombination occurred between LA and intron-exon 11 sequences with their homologous sequence in *Trpml3* locus, carrying only the *neo*^{R} cassette with them. Incomplete recombination into the genomic *Trpml3* locus resulted in loss of the second *loxP* site. **C:** Illustrating old and changed targeting vector. The new targeting vector was obtained by mutagenesis reactions; the removal of *loxP* site downstream of intron-exon 11-intron and neighboring vector sequences and insertion of a new *loxP* site immediately downstream of *Trpml3* exon 11 in the intron sequence. Mutagenesis reactions resulted in increased length of 3' arm of homology from 1700 bp to 2237 bp, and decreased the length of the *Trpml3* exon 11 targeted sequences from 1473 bp to 904 bp, thereby reducing the chance of incomplete homologous recombinations.

3.3.1.4. Step 2: Electroporation of *Trpml3* targeting construct in 129sv/svj ES cells

The final vector DNA was digested with *Not*I, gel purified, and submitted to the Stanford Transgenic Research Center. The staff at the Stanford Transgenic Research Center performed electroporation into 129sv/svj ES cells, selection and ES cell colony picking, and provided ES cell clones to screen for homologous recombination. Screening was done by PCR from genomic DNA. As mentioned above, only neomycin-resistant clones are able to grow in presence of the selective reagent geneticin (G418), which is used in conjunction with the neomycin resistance gene. In total, 156 clones were grown in selective culture medium. 110 of these clones were screened by PCR. Specific

oligonucleotides were used to amplify the targeted genomic region, which should include the second *loxP* site and the sequences downstream of the 3' arm (Fig. 32A). The resulting amplified PCR product indicative of correct targeting should have had a length of 3300 bp. Four ES cell clones (96-well plate #1: D2, E5; 96-well plate #2: C5, D8) were identified with this strategy, indicative of correct recombination into the *Trpml3* gene (Fig. 32B). Despite the existence of a negative DTA selection marker, many clones with random integration were encountered. Nevertheless, sequence analyses revealed that the second *loxP* site was integrated in all four ES cell clones (Fig. 32C). Examination of the downstream transition of the 3' arm revealed that clone 1D2 was still carrying 50 bp of the DTA cassette, and 2D8 had a mismatch of 60 bp of unknown source. Clones 1E5 and 2C5 did show the correct integration of the 3' arm. Both correct clones were further examined by amplifying the 5' arm of homology with a length of approximately 3300 bp (Fig. 32B'). Integration of the 5' arm, the first *loxP* site, and the following exon 11 were further analyzed by sequencing of the respective PCR amplification products. Sequencing of PCR amplification products showed correct integration of all necessary elements at the correct positions. The most important oligonucleotides used for sequencing are illustrated in Figure 33A, additional sequencing oligonucleotides are summarized in Table 4. Analysis solely by PCR amplification or even by Southern blot could not have revealed the existence of all necessary elements, such as both *loxP* sites. Sequence analysis of the complete targeted locus did not only prove the existence of both *loxP* sites, but also the correct transition of the 5' and 3' arm of homology into the *Trpml3* allele.

Figure 32: Genotyping analysis of ES cells. A: Schematic drawing of the *Trpml3* targeted construct before and after Flp site-specific recombination (*Trpml3*$^{loxP/}$) as shown in Figure 29. The position of sense (sn) and antisense (asn) oligonucleotides used for PCR are indicated with black arrows, those for sequencing analysis with grey arrows. The names of PCR products and the corresponding lengths are parenthesized. (The sequences of oligonucleotides and the length of PCR fragments are shown in Table 4.) **B:** PCR amplification products of neomycin resistant ES cells clones: 3' arm (right arm = RA): 3300 bp. Positive clones were 1D2, 1E5, 2C5, and 2D8, which were indicated with bold red writing. **B':** PCR amplification products of ES cells clones: 5' arm (left arm = LA): 3300 bp. Only 1E5 and 2C5 clones have shown a positive signal. **C:** Representative genotyping result showing genomic RA – 2nd *loxP* DNA sequence traces of ES cell clones with and without integrated 2nd *loxP* site, respectively. The nucleotides are color-coded, A: green, T: red, C: blue, and G: black. **D:** Genotyping protocol after Flp site-specific recombination. The removal of *neo*^{R} cassette is resulting in a shortened target. Two clones of each ES cell line, E5 and C5, are presented with different PCR runs: lox: 471 bp (targeted *Trpml3*) and 309 bp (wild-type *Trpml3*); neo: 374 bp (targeted *Trpml3* after *neo*^{R} excision) and 2116 bp (targeted *Trpml3* if *neo*^{R} would not have been excised); LA: 3200 bp; and RA: 3300 bp. Clone 2C5A1 did not show LA and RA amplification products.

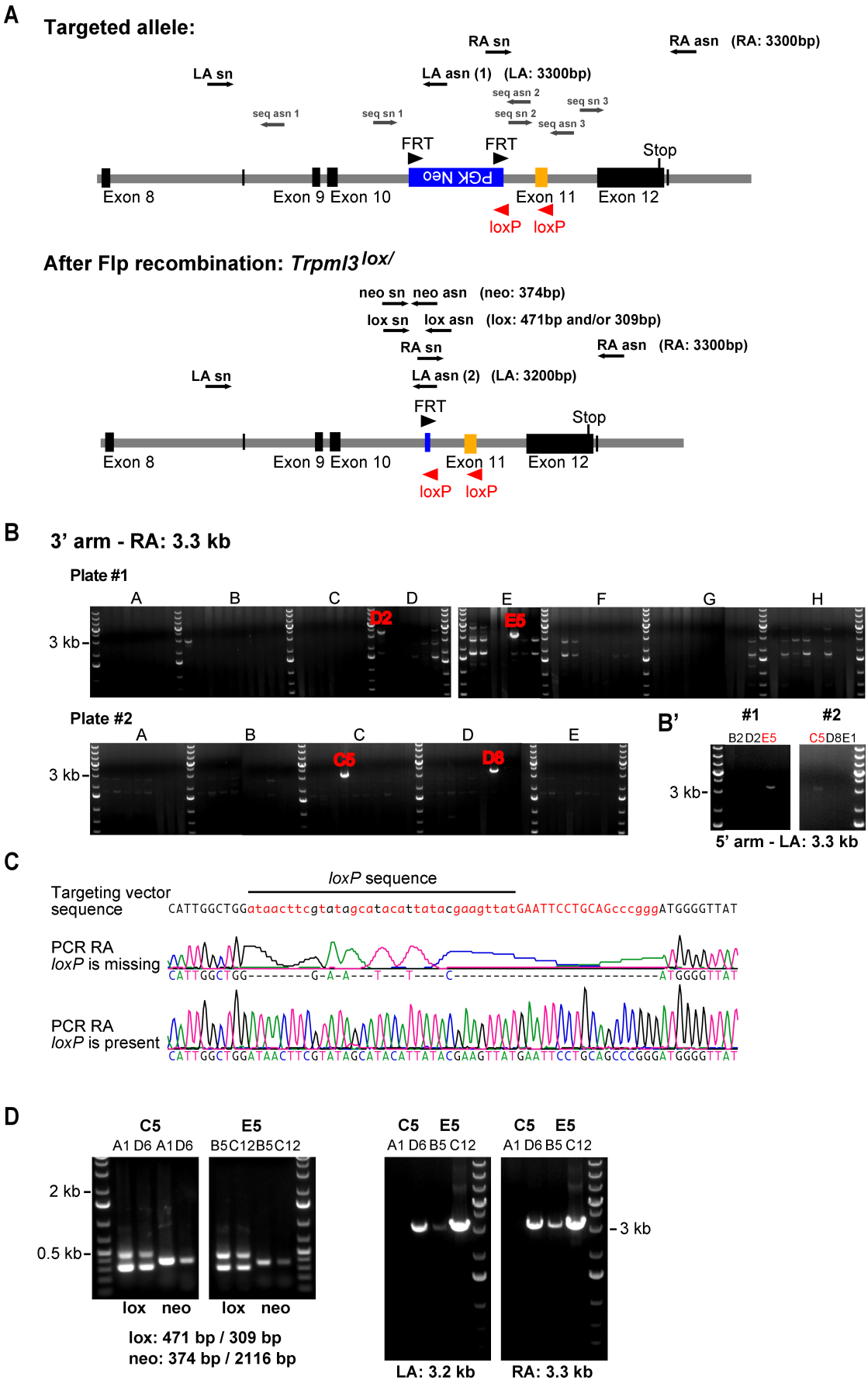

Figure 32: Genotyping analysis of ES cells.

3.3.1.5. Step 3: Removal of the selection gene *neo*^{R} by Flp site-specific recombination

One of the straightforward ways to avoid selection interference and genetic ambiguity in gene targeting experiments is to use site-specific recombination to remove the *neo*^{R} cassette after homologous recombination. This is done at the ES cell stage. Both clones 1E5 (= 96-well plate #1, clone E5) and 2C5 (= 96-well plate #2, clone C5) were expanded and transfected by electroporation with an expression vector for Flp site-specific recombinase, resulting in transient expression of Flp recombinase in the targeted ES cell clones. Excision of *neo*^{R} was readily detectable by PCR analysis. Oligonucleotides were designed to distinguish between positive and negative Flp recombination events (Fig. 32A, Table 4). After effective recombination, a 374 bp *versus* 2116 bp PCR fragment was amplified. Two clones of both lines, 1E5 and 2C5, were examined one more time with the entire genotyping protocol (Fig. 32D). Finally, two independent ES clones were used to generate chimeric mice. 1E5FlpC12 (= ES cell clone 1E5 after Flp treatment; clone C12 in initial 96-well plate) was the first ES cell clone, which was injected into blastocysts of C57BL/6J mice.

3.3.1.6. Step 4: Injections into blastocysts generating chimeric mice and germline transmission

ES cell line 1E5FlpC12 carrying the targeted *Trpml3* allele was first injected into blastocysts to generate germline chimeric mice by the Stanford Transgenic Research Center. The most convenient and readily apparent genetic marker of chimerism is coat color. Chimeric combination of strains that differ in only one coat color locus allow a simple visual appreciation of the degree of tissue contribution stemming from injected ES cells in terms of the proportion of the coat that expresses the specific ES cell coat color allele. ES cells for targeting were derived from 129sv/svj mice with agouti coat color, whereas host blastocysts were black C57BL/6J. Blastocysts carrying cells with agouti and black genotype were then transferred into foster mothers to generate chimeric animals. The decision of whether or not to breed a particular chimera depends on its level of chimerism. This is done by estimating the ratio of cells derived from 129sv/svj ES cells by examining the coat color of the chimeric mice. If a clone contributes more than 60% (more agouti than black) of the coat in a chimeric mouse, then it is generally expected that germline transmission of the transgenic line will happen at a similar level (Papaioannou and Johnson, 2000). 1E5FlpC12 ES cell lines contributed to more than 60%. Only male chimeras were used for mating with C57BL/6J wild-type females, since male chimeras can

produce more offspring than females in a given period of time. A chimeric male of 80% derived from 1E5FlpC12 delivered successful germline transmission (Fig. 33). Agouti pups were analyzed by PCR of genomic DNA (with the same genotyping protocol used in Fig. 32D), which revealed that in total three out of four agouti mice were heterozygous for *Trpml3*$^{loxP/+}$.

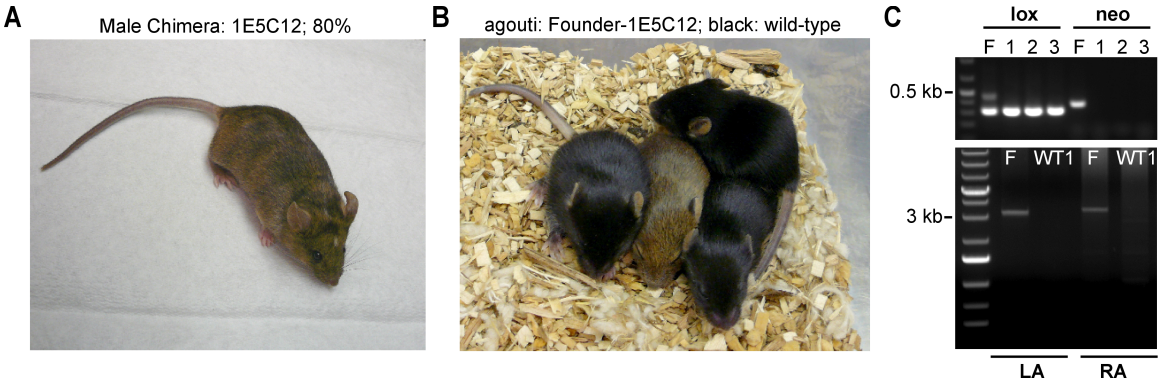

Figure 33: Chimerism and germline transmission. A: Shown is a male chimera derived from ES cell clone 1E5FlpC12 with a chimerism of 80%. **B:** P10 offspring of 1E5FlpC12 male and wild-type C57BL/6J female. On the basis of the agouti coat color, germline transmission was easily visible. Black mice are wild-type C57BL/6J mice. **C:** Shown are genotyping results of tail tissue of the particular offspring (B). Although the agouti coat color is representing that this mouse is derived from ES cell clone 1E5FlpC12, it was not certain that the newly engineered *Trpml3* sequence was incorporated. For example, an ES cell colony may not be truly clonal and may contain targeted and non-targeted ES cells. Therefore, additional genotyping was necessary. As the results are showing, the agouti mouse is a *Trpml3*$^{lox/+}$ founder (lane "F"): lox: 471 bp and 309 bp; neo: 374 bp; LA; 3200 bp; and RA: 3300 bp. Black mice (lanes "1,2,3") were C57BL/6J wild-type mice: lox: 309 bp (represents the wild-type fragment, as in a heterozygous *Trpml3*$^{lox/+}$ mouse); and as expected no amplification with neo, LA, and RA oligonucleotides. WT1 = wild-type mouse 1.

3.3.1.7. Step 5: Excision of the *Trpml3* exon 11 using different Cre mice

Heterozygous *Trpml3*$^{lox/+}$ mice were mated with different Cre driven mouse lines. The widely used "standard" mouse strain for many transgenic experiments, C57BL/6J, has early age-related hearing loss (Li and Borg, 1991; Zheng et al., 1999), a fact that could substantially complicate our analysis. Therefore, we decided to generate all *Trpml3-Cre* animals in the FVB/NJ mouse strain that does not display elevated auditory brainstem recording thresholds during the first three month of life and is considered a normal hearing mouse strain (Zheng et al., 1999). Also the litter size varies among strains, ranging from about three pups per litter in some poorly breeding 129 substrains to 12 or more pups per litter in the FVB/NJ mouse strains (Silver, 1995; Lamberts, 2007). Given the costs of keeping mice, the breeding colony was kept relatively small. But to finish the experiments (n≥3 for each group) in a short time period, a larger litter size was important. All Cre

mouse lines were crossed into the FVB/NJ albino genetic background to obtain FVB/NJ-Cre inbred lines. A strain is defined as inbred if it was produced by sibling mating for more than 20 generations after which all mice are considered isogenic or genetically identical (Lamberts, 2007). The *Trpml3*$^{lox/}$ locus (129sv/svj) has been crossed into the FVB/NJ background for 3 generation so far, therefore, it cannot yet be considered being isogenic. First matings of *Trpml3*$^{lox/+}$ with ear-specific and ubiquitously expressing Cre drivers were performed (Fig. 34). The Cre mouse lines used in these experiments, *Math1-CreER*^{TM} and *Hprt*^{Cre} will be described in more detail below.

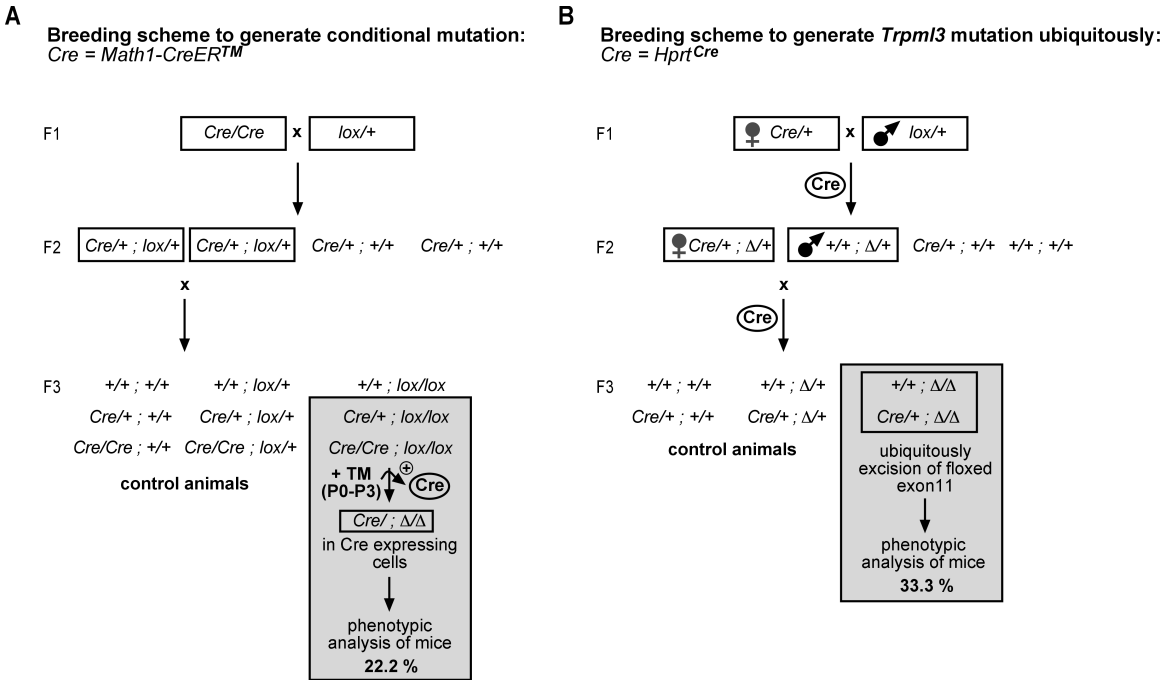

Figure 34: Examples of breeding schemes for conditional gene targeting. The symbol Δ indicates the deleted *Trpml3* exon 11 generated by recombination of the floxed (lox) locus; +, represents the wild-type locus. **A:** Shown is the breeding scheme to generate a conditional mutation. After two generations, mice were harboring the recombinase locus and were homozygous for the floxed exon 11, which represented ~22.2% of the offspring (highlighted by large box). After tamoxifen application to P0 to P3 pups, Cre was activated and translocated to the nucleus of sensory hair cells to perform site-specific recombination. **B:** Shown is the breeding scheme to generate ubiquitously *Trpml3*$^{\Delta/\Delta}$ mice, using *Hprt*^{Cre}. The use of female *Hprt*^{Cre} animals was ensuring the excision of the floxed exon 11 regardless of *Hprt*^{Cre} inheritance early in the development. After two generations, the first homozygous *Trpml3*$^{\Delta/\Delta}$ mice were obtained with a likelihood of ~33.3% (highlighted by a large box).

3.3.1.7.1. Ubiquitous excision of the *Trpml3* exon 11 using an *Hprt*^{Cre} transgenic line

To investigate whether TRPML3 plays general roles or whether the knockout of the gene affects development, heterozygous *Hprt*$^{Cre/+}$ mice were used to introduce a ubiquitous and highly efficient excision of the *Trpml3* exon 11. The hallmark of the *Hprt*$^{Cre/+}$ transgenic

mouse line is the highly efficient ubiquitous excision that is complete at the first stages of development. Another trait of the line is that the *Hprt* locus is X-linked (Tang et al., 2001). $Hprt^{Cre/+}$; $Trpml3^{lox/+}$ females were mated to $Trpml3^{lox/+}$ males (Fig. 34B). The floxed exon 11 was always excised regardless of $Hprt^{Cre}$ inheritance. It was shown before that oocytes of $Hprt^{Cre}$ females have sufficient stored Cre recombinase to excise floxed DNA segments already at the zygote or early cleavage stages (Tang et al., 2001), which results in recombination of floxed *Trpml3* already early during development. The mutation went into germline as well, meaning that there was no need to utilize Cre any more in later stages. After two generations, mice were harboring homozygously excised *Trpml3* exon 11 (Fig. 34B). Referring to the wide expression of TRPML3 mRNA (see 1.4, Fig. 6), it was expected that the following tissues and organs might be affected by this inactivation procedure: skin, kidney, lung, colon, eye, thymus, or olfactory bulb. Surprisingly, $Hprt^{Cre/}$; $Trpml3^{\Delta/\Delta}$ mice were not only viable, but also without visible phenotype. The symbol Δ indicates the deleted *Trpml3* exon 11 generated by recombination of the floxed locus. $Hprt^{Cre/}$; $Trpml3^{\Delta/\Delta}$ mice were indistinguishable from their heterozygous or wild-type littermates in size and weight. The breeding performance of homozygous animals was normal. This was obvious because a stable ubiquitous $Trpml3^{\Delta/\Delta}$ mouse line was maintained next to a control line. To ensure that *Trpml3* exon 11 was indeed excised, genomic amplification of the specific region and PCR analyses were performed (Figs. 35C and 36).

To facilitate understanding of the PCR analysis, Figure 36B is showing PCR results of genomic DNA isolated from progeny of wild-type (+/+), heterozygous (lox/+) and homozygous (lox/lox) $Trpml3^{lox/}$ animals without Cre background. As previously shown, oligonucleotides were designed to distinguish between targeted and untargeted *Trpml3* loci. Positions of oligonucleotide-hybridization are schematically indicated (Fig. 35A). The oligonucleotide-pair “lox” is designed to provide information about the genotype. Homozygous animals only showed one PCR product with the length of 471 bp, whereas heterozygous animals additionally had a wild-type 309 bp *Trpml3* fragment. The second oligonucleotide pair “neo” demonstrates the existence of the targeted *Trpml3* only. PCRs of LA and RA also proved the correct integration into the *Trpml3* allele. Wild-type lanes (+/+) showed no amplification product. The proof of excised exon 11 is shown in Figure 35C. Since “lox-asn“ oligonucleotide is located in the intron sequence, which was excised together with exon 11 by Hprt-driven Cre recombinase, only the wild-type *Trpml3* allele was amplified with “lox” oligonucleotides. However, the existence of targeted

Trpml3 could be determined with "neo"-PCR in homozygous and heterozygous animals (Fig. 35C, left gel). The excision of exon 11 also resulted in a shortened right arm PCR amplification fragment (2340 bp), as well as in a 993 bp fragment with oligonucleotide pair "exc" (Fig. 35C right PCR panel). The wild-type product had a length of 1952 bp. PCR results of genomic DNA revealed the complete excision of the *Trpml3* exon 11.

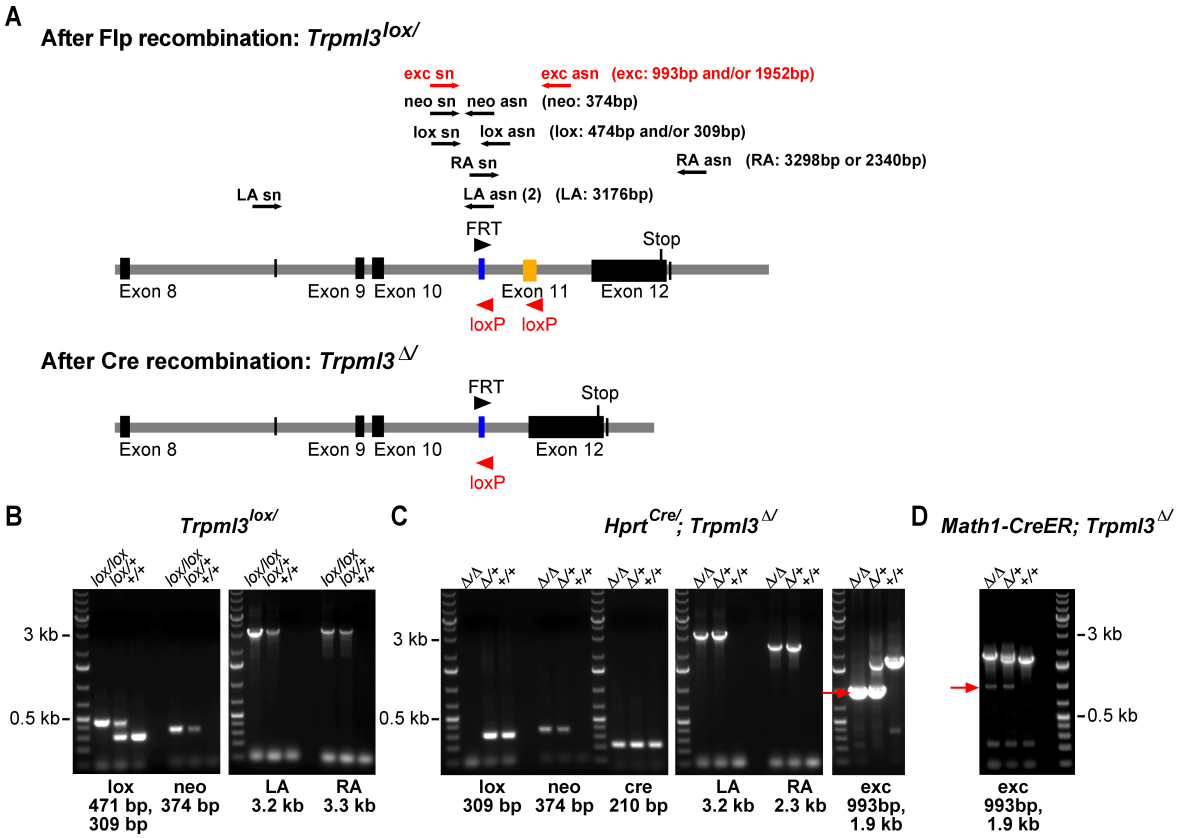

Figure 35: Genotyping analysis. A: Schematic drawing of the *Trpml3* targeted allele before (*Trpml3*$^{loxP/}$) and after Cre recombination (*Trpml3*$^{\Delta/}$) as shown in Figure 28. The position of sense (sn) and antisense (asn) oligonucleotides are indicated with arrows. The names of PCR products and the corresponding lengths are parenthesized. **B:** PCR amplification products of *Trpml3* locus of homozygous (lox/lox), heterozygous (lox/+), and wild-type (+/+) *Trpml3*$^{lox/}$ mice are shown: lox: 309 bp and/or 471 bp, neo: 374 bp, and left arm (LA): 3176 bp and right arm (RA): 3298 bp. **C:** Genotyping after Cre recombination of representative *Hprt*$^{Cre/}$*; Trpml3*$^{\Delta/}$ mice. All mice are heterozygous for *cre* (210 bp). The same sets of oligonucleotides were used as in (B), however lox-PCR only displayed the wild-type 309 bp PCR fragment, since the lox asn-oligonucleotides cannot hybridize after the targeted exon 11 was excised; and RA: 2340 bp, since exon 11 was excised by Cre. The last panel on the right shows the shortened fragment (indicated with a red arrow): 1952 bp for *Trpml3*$^{loxP/}$ and 993 bp for *Trpml3*$^{\Delta/}$. **D:** Genotyping results after Cre recombination of representative *Math1-CreER; Trpml3*$^{\Delta/}$ mice (using oligonucleotide pair exc). Since the excision of exon 11 was only introduced in sensory hair cells, the PCR results of homozygous and heterozygous mice for the *Trpml3* locus are contaminated with unexcised PCR amplification fragments (1952 bp). The shortened 993 bp fragment is indicated with a red arrow. The symbol Δ indicates the deleted exon 11 in the *Trpml3* allele generated by recombination of the floxed (*loxP*) locus; + represents the wild-type locus.

To examine whether the mutant *Trpml3*$^{\Delta}$ allele is being transcribed, RT-PCRs were performed (Fig. 36). mRNA from kidney and inner ear was harvested from P21 mice of each genotype. RT-PCR amplification of specific cDNA sequences before and after the site of deletion indicated that wild-type and *Trpml3*$^{\Delta}$ mRNA was present in kidney and the inner ear of all animals (Fig. 36A,B, RT-2 and 3), whereas amplification of cDNA encoding exon 11 (RT-1) was only possible from wild-type (*Trpml3*$^{+/+}$) and heterozygous animals (*Trpml3*$^{\Delta/+}$), but not from mRNA of *Trpml3*$^{\Delta/\Delta}$ mice. With the loss of exon 11, which is encoding for the region between TM5 and TM6 including the pore-loop and TM6 itself, it is expected that this deletion would lead to a TRPML3 ion channel without a core-domain, the pore. Therefore *Trpml3*$^{\Delta/\Delta}$ mice will be unable to generate functional TRPML3 protein.

An additional oligonucleotide pair was used (RT-4) to amplify and then sequence-analyze the coding region comprising exon 10, 11, and 12 (Fig. 36A-C). Sequence analysis revealed that in mutated animals, splicing occurred without frame shift between exon 10 and exon 12, resulting in a shorter message (266 bp instead of 473 bp) (Fig. 36C). The recombination allowed the complete removal of exon 11, which could result in the translation of a non-functional, truncated protein of predicted 55.5 kDa, instead of 63.7 kDa.

To demonstrate that the pore-less TRPML3 protein does not function as an ion channel, a cDNA encoding a fusion protein of mTRPML3(Δ exon11) with yellow fluorescent protein was generated and expressed in HEK293 cells. The subcellular distribution of the mutant channel TRPML3(Δ exon11), analyzed by confocal microscopy, was different from wild-type TRPML3-YFP fusion protein. TRPML3(Δ exon11) protein appeared to be absent from the plasma membrane and was mainly located intracellular. In calcium imaging experiments, it was shown that the TRPML3 agonist SN-2 does not activate TRPML3(Δ exon11). No changes of $[Ca^{2+}]_i$ were detected, whereas wild-type TRPML3-expressing HEK293 cells responded with a robust increase in $[Ca^{2+}]_i$. The average maximum $[Ca^{2+}]_i$ levels were 0.81 ± 0.073 (Δratio 340nm/380nm, n=10) for wild-type TRPML3 and -0.016 ± 0.009 (Δratio 340nm/380nm, n=6) for TRPML3(Δ exon11). The differences between wild-type and mutant were statistically significant (Student's *t* test: $p<0.0001$). These results indicate that TRPML3(Δ exon11) is an inactive ion channel when expressed in HEK293 cells. Therefore, I presume that *Trpml3*$^{\Delta/\Delta}$ mice lack functional TRPML3 protein. The localization study and the calcium imaging experiments of TRPML3(Δ exon11) were done in collaboration with Dr. Lars Becker.

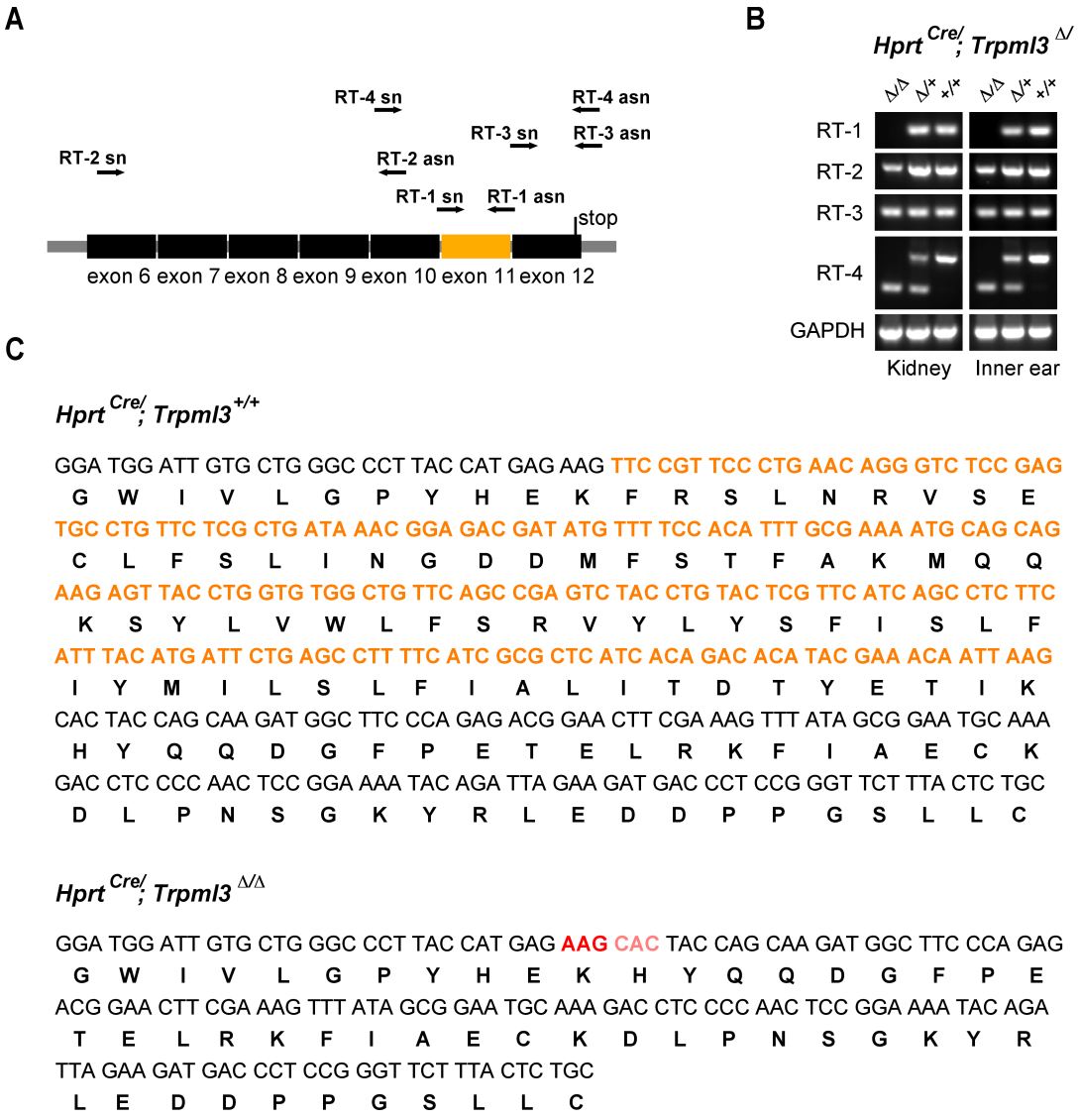

Figure 36: RT-PCR analysis of TRPML3 mRNA expression in kidney and inner ear from 3-week-old *Hprt$^{Cre/}$; Trpml3$^{\Delta/}$* mice. **A:** Schematic illustration is showing exon 6-12. The sense (sn) and antisense (asn) oligonucleotides are indicated with black arrows. Oligonucleotides RT-3 and RT-4 hybridize to the UTR sequence of *Trpml3*. **B:** Amplification products RT-1 (200 bp), RT-2 (512 bp), RT-3 (181 bp), and RT-4 (473 bp for wild-type cDNA, and 266 bp for Cre targeted *Trpml3* cDNA). Oligonucleotides for GAPDH (442 bp) were used to control for RNA preparation quality. The symbol Δ indicates the deleted exon 11 in the *Trpml3* allele generated by recombination of the floxed (*loxP*) locus; + represents the wild-type locus. **C:** Representative sequencing results of gel-purified RT-4 *Hprt$^{Cre/}$; Trpml3$^{+/+}$* and *Hprt$^{Cre/}$; Trpml3$^{\Delta/\Delta}$* PCR fragments. The translated protein sequence is shown underneath the nucleotide sequences. The wild-type PCR product (top panel sequence) includes intron 11 (in orange), whereas the exon 11 was completely missing in the *Hprt$^{Cre/}$; Trpml3$^{\Delta/\Delta}$* PCR product (bottom panel). The splicing occurred between exon 10 and exon 12. The red codon AAG represents the end of exon 10, and the pink codon CAC the beginning of exon 12.

3.3.1.7.2. Sensory hair cell specific Cre mice: *Math1-CreER^{TM}*

To investigate the conditional inactivation of *Trpml3* in the mouse inner ear, two different Cre driver mice were available: *Foxg1^{Cre}* (Hébert and McConnell, 2000) and *Math1-CreER^{TM}* (Chow et al., 2006) mice. In *Foxg1^{Cre}* mice, Cre recombinase expression is controlled by the Foxg1 promoter, which has previously been shown to efficiently inactivate floxed alleles in developing otic vesicles (Zelarayan et al., 2007). This expression is well characterized and at E8.5, the first signs of Cre expression are visible in the inner ear anlage, and at E10.5, the entire otocyst shows Foxg1-driven Cre expression (Hébert and McConnell, 2000). Foxg1-driven Cre affects most cell types of the inner ear, including inner and outer hair cells, supporting cells, and spiral ganglion cells, but the stria vascularis is devoid of expression (Zelarayan et al., 2007). It was decided, however, not to pursue this mouse line further because mice with a ubiquitous *Hprt^{Cre}*-driven *Trpml3* inactivation were viable and a backup for early embryonic lethality was not required. Another reason to avoid this strain was the aggressive behavior of male *Foxg1^{Cre}* mice. They attack their mates as well as their offspring, which made it difficult to maintain the line.

The *Math1-CreER^{TM}* transgenic model is using a technique, where spatial and temporal control over genome modification involves the use of a recombinase-steroid receptor fusion protein that can be activated at will by systemic administration of an altered hormone. This mouse line was generated by placing the gene encoding a fusion protein of Cre with the altered ligand-binding domain of the estrogen receptor (ER^{TM}) under the control of a Math1 enhancer/basic promoter (Chow et al., 2006). The mutation in ER^{TM} prevents binding of its natural ligand (17β-estradiol) at normal physiological concentrations, but renders the ER^{TM} domain responsive to 4-hydroxy-tamoxifen (4-OH-TM) (Danielian et al., 1993). Fusion of Cre and ER^{TM} leads to the ER^{TM}-dependent cytoplasmatic sequestration of Cre by Hsp90, thereby preventing Cre-mediated recombination because the fusion protein is excluded from the nucleus. Binding of the hormone tamoxifen, however, leads to a disruption of the interaction with Hsp90, permitting access of Cre-ER^{TM} to the nucleus and initiation of recombination at *loxP* sites (Chow et al., 2006). Math1 is a transcription factor involved in the development of the cerebellum and hair cells of the cochlea and vestibular organs (Ben-Arie et al., 1997; Bermingham et al., 1999). In the inner ear of *Math1-CreER^{TM}* mice, the Cre activity had to be induced between P0 and P5 because the Cre-ER transgene is downregulated at P6 and cannot be induced at P7 or in adulthood (Chow et al., 2006). It has been shown that

tamoxifen at a dose of 3-4 mg/40 g body weight daily for one to three injections was sufficient to induce Cre activity in the inner ear (Chow et al., 2006). Control experiments show that neither tamoxifen treatment alone nor expression of Cre nor Cre-ER in hair cells results in detectable effects on hearing sensitivity in mice, as measured by auditory brainstem response thresholds (Chow et al., 2006, Li et al., 2004; Tian et al., 2004). As a strategy to overcome potential compensatory effects, tamoxifen-induced *Math1-CreER*^{TM} mice were used to introduce the excision of *Trpml3* exon 11 only in sensory hair cells (and cerebellar granule cell precursors) at P0-P3, shortly before sensory cochlear hair cells acquire functional mechanosensation (Fig. 34A).

To examine the excision of exon 11, the same genotyping protocol of organ of Corti genomic DNA was performed (as described for *Hprt*$^{Cre/}$; *Trpml3*$^{\Delta/}$; in 3.3.1.7.1. and Fig. 35C), which showed clearly the excised 993 bp PCR-fragment (Fig. 35D). Since the disruption was only introduced in sensory hair cells, the PCR results were contaminated with unexcised PCR amplification fragments. Furthermore, because no good antibodies to TRPML3 exist and the channel's mRNA is expressed at quite low levels, it was virtually impossible to unequivocally ascertain the extent of TRPML3 inactivation, which could range from only a few hair cells *versus* all.

3.3.1.8. Auditory brainstem response measurements of *Trpml3*$^{loxP/}$ mice

Based on the varitint-waddler mutant phenotype, TRPML3 has been proposed to play a role in hearing, and the potential of playing a role as part of the hair-cell transduction channel complex has not been convincingly excluded (Cuajungco et al., 2007). Consequently, we were curious to investigate whether the disruption of *Trpml3* in mice would display hearing and balance defects. Three-week-old *Hprt*$^{Cre/+}$; *Trpml3*$^{+/+}$, *Hprt*$^{Cre/+}$; *Trpml3*$^{\Delta/+}$, and *Hprt*$^{Cre/+}$; *Trpml3*$^{\Delta/\Delta}$ mice showed normal Preyer's reflex, which means that they flick the pinna of their ears when startled with a loud sound (Jero et al., 2001). Auditory-evoked brainstem response measurements were used to evaluate hearing thresholds of P21 mice (Fig. 37). As the Preyer's reflex and other subjective ways to assess hearing are only effective for identification of profound hearing loss, more objective electroacoustical tests were conducted: Click, 8-, 16-, and 32 kHz tone burst measurements revealed no significant differences in ABR thresholds and interwave latencies among all three groups (see *Materials and Methods* for explanation, 2.2.4.1.) *Hprt*$^{Cre/+}$; *Trpml3*$^{+/+}$, *Hprt*$^{Cre/+}$; *Trpml3*$^{\Delta/+}$, and *Hprt*$^{Cre/+}$; *Trpml3*$^{\Delta/\Delta}$ (Fig 37A,B) (means ±SEM): ABR thresholds for control mice *Hprt*$^{Cre/+}$; *Trpml3*$^{+/+}$ were 32.5 ±1.12,

15.83 ±1.54, and 37.5 ±2.5 dB HL for 8 -, 16 -, and 32 kHz tone bursts and 34.17 ±0.83 dB HL for click stimuli (n=6). *Hprt*$^{Cre/+}$; *Trpml3*$^{\Delta/+}$ showed ABR thresholds of 33.3 ±1.05, 15.83 ±2.39, and 40 ±2.89 dB HL for 8 -, 16 -, and 32 kHz tone bursts, and 35 ±1.83 dB HL for click stimuli (n=6). For *Hprt*$^{Cre/+}$; *Trpml3*$^{\Delta/\Delta}$ ABR thresholds were 33.3 ±1.05, 15 ±2.24, and 37.5 ±1.83 dB HL for 8 -, 16 -, and 32 kHz tone bursts and 35 ±1.29 dB HL for click stimuli (n=6) (Fig. 37B).

Interwave latencies between wave I and wave III at 70 dB, which are indicative of the afferent auditory nerve conductance were (means ±SEM) 1.9 ±0.026 msec in *Hprt*$^{Cre/+}$; *Trpml3*$^{+/+}$ animals (n=6), compared to 1.87 ±0.026 msec in *Hprt*$^{Cre/+}$; *Trpml3*$^{\Delta/+}$ (n=6), and 1.86 ±0.019 msec in *Hprt*$^{Cre/+}$; *Trpml3*$^{\Delta/\Delta}$ littermates (n=6). These results suggest that TRPML3 as a homomer does not play a critical role in hearing. Nevertheless, because the excision of *Trpml3* exon 11 using *Hprt*^{Cre}-mediated recombination was introduced very early in development, compensation effects cannot be excluded with this approach (Dymecki, 2000). A different TRP channel, such as the related TRPML2 might compensate for loss of TRPML3.

To circumvent potential compensatory mechanisms, tamoxifen-inducible *Math1-CreER*^{TM} mice were used to inactivate TRPML3 in cochlear hair cells between P0-P3. Control mice injected with up to three doses of tamoxifen retain normal hearing (Chow et al., 2006). In fact, the only manifestation of tamoxifen toxicity was a transient weight loss. However, ABR measurements of *Math1-CreER*^{TM}*; Trpml3*$^{\Delta/\Delta}$ mice at three weeks of age revealed no differences compared to their control littermates *Math1-CreER*^{TM}*; Trpml3*$^{\square/\square}$ and *Math1-CreER*^{TM}*; Trpml3*$^{\Delta/+}$ (Fig. 37C), suggesting that compensatory mechanisms most likely do not explain the lack of a TRPML3 hearing phenotype. ABR thresholds for *Math1-CreER*^{TM}; *Trpml3*$^{+/+}$ mice were 31.67±1.67, 15 ±0, and 35 ±5 dB HL for 8 -, 16 -, and 32 kHz tone bursts and 35 ±0 dB HL for click stimuli (n=3). For *Math1-CreER*^{TM}; *Trpml3*$^{\Delta/+}$ mice ABR thresholds were 31.67 ±1.67, 16 ±1.67, and 35 ±0 dB HL for 8 -, 16 -, and 32 kHz tone bursts, and 35 ±0 dB HL for click stimuli (n=3). The ABR thresholds for *Math1-CreER*^{TM}; *Trpml3*$^{\Delta/\Delta}$ mice were 30 ±2.89, 13.3 ±1.67, and 40 ±2.89 dB HL for 8 -, 16 -, and 32 kHz tone bursts and 33.3 ±1.67 dB HL for click stimuli (n=3) (Fig. 37C). Mice were also analyzed at 3 months of age to determine possible enhancement or early onset of age-related hearing loss. But reviewing audiograms revealed no ABR threshold differences between mutant mice and respective control mice (data not shown). The use of *Math1-CreER*^{TM} mice did not reveal potential compensatory mechanisms of *Trpml3* inactivation.

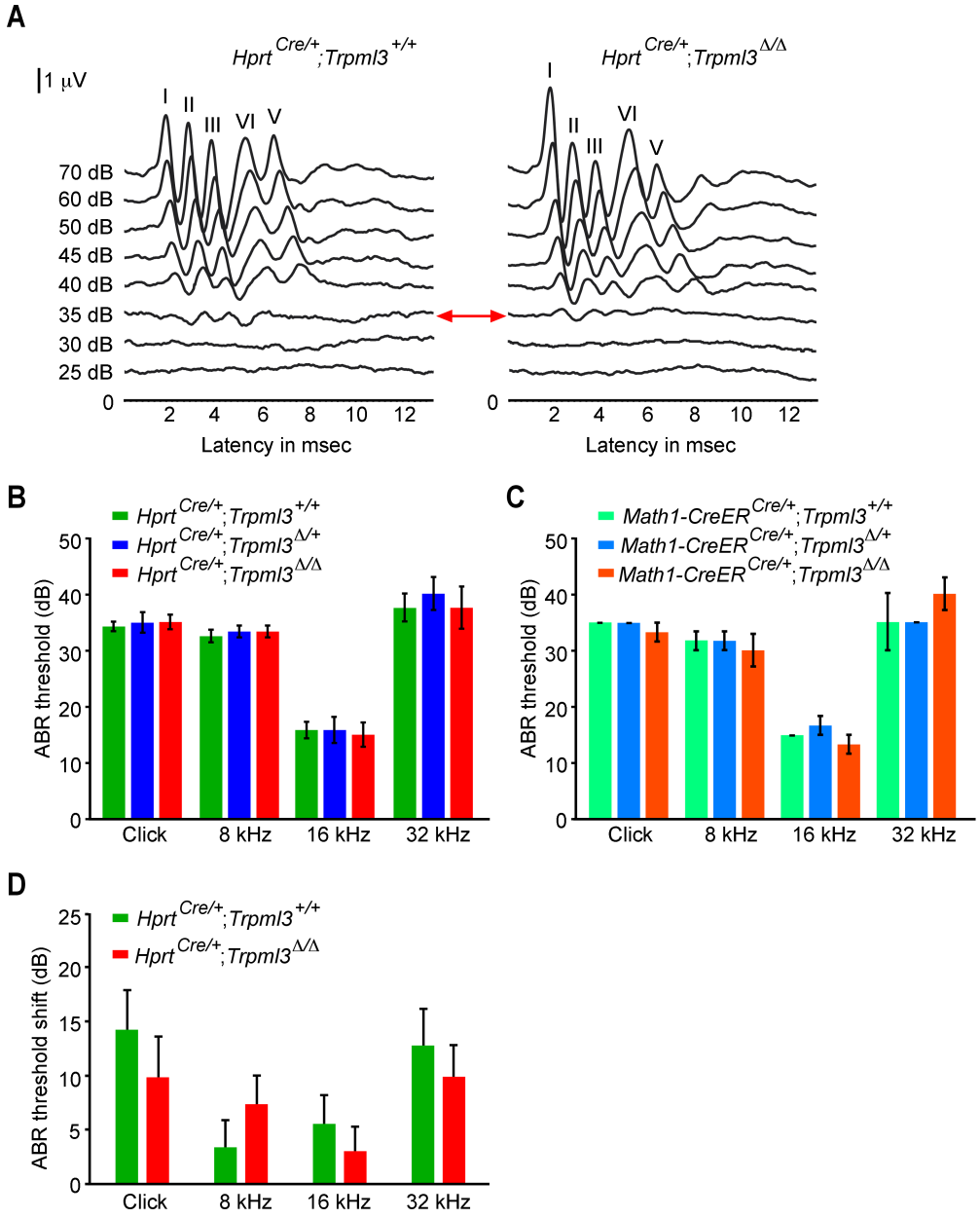

Figure 37: Auditory brainstem response (ABR) measurements. A: Graph shows representative auditory brainstem responses of 3-week-old *Hprt*$^{Cre/+}$*; Trpml3*$^{+/+}$ and *Hprt*$^{Cre/+}$*; Trpml3*$^{\Delta/\Delta}$ mice in response to a click stimulus. ABRs were recorded at sound stimulation intensities 25-70 dB hearing level. ABR waves I-V are indicated above the peaks. Threshold was determined by reducing the stimulus intensity in 5 dB steps. Red arrow highlights the hearing threshold, which is at 35 dB in this representative example pair. **B:** Shown are ABR thresholds (mean values ±SEM) to click, 8-, 16-, and 32 kHz stimuli of *Hprt*$^{Cre/+}$*; Trpml3*$^{+/+}$ (n=6), *Hprt*$^{Cre/+}$*; Trpml3*$^{\Delta/+}$ (n=6), and *Hprt*$^{Cre/+}$*; Trpml3*$^{\Delta/\Delta}$ (n=6). **C:** Shown are ABR thresholds (mean values ±SEM) to click, 8-, 16-, and 32 kHz stimuli of *Math1-CreER*$^{Cre/+}$*; Trpml3*$^{+/+}$ (n=3), *Math1-CreER*$^{Cre/+}$*; Trpml3*$^{\Delta/+}$ (n=3), and *Math1-CreER*$^{Cre/+}$*; Trpml3*$^{\Delta/\Delta}$ (n=3) mice, respectively. **D:** ABR threshold shifts of 3-month-old *Hprt*$^{Cre/+}$*; Trpml3*$^{+/+}$ (n=7) and *Hprt*$^{Cre/+}$*; Trpml3*$^{\Delta/\Delta}$ (n=8) one week after the acoustic overexpression of 125 dB at 4 kHz for 4 hours. Shown are mean values ±SEM. Statistical comparisons of means of different genotypes were made using one-way ANOVA followed by Tukey's post test; no significant differences were observed, $p>0.05$. (Data shown in D were kindly provided by Dr. Lars Becker.)

To investigate whether acoustic challenge of the auditory system would reveal a more subtle role of TRPML3, 3-month-old *Hprt*$^{Cre/+}$;*Trpml3*$^{+/+}$ and *Hprt*$^{Cre/+}$;*Trpml3*$^{\Delta/\Delta}$ mice were exposed for 4 hours to 4 kHz pure tone at 125 dB SPL in a truncated pyramid-shaped exposure box (Liberman and Gao, 1995; Tabuchi et al., 2005). ABR thresholds of littermates of both genotypes before and one week after the noise exposure revealed no significant differences in noise susceptibility between the two groups (Fig. 37D). ABR threshold shifts (mean ±SEM) for *Hprt*$^{Cre/+}$;*Trpml3*$^{+/+}$ were 3.57 ±2.37, 5.71 ±2.54, and 13 ±3.22 dB for 8 -, 16 -, and 32 kHz tone bursts and 14.28 ±3.69 dB HL for click stimuli (n=7). For *Hprt*$^{Cre/+}$;*Trpml3*$^{\Delta/\Delta}$ ABR threshold shifts were 7.5 ±2.54, 3.13 ±2.18, and 10 ±2.89 dB for 8 -, 16 -, and 32 kHz tone bursts and 10 ±3.65 dB HL for click stimuli (n=8). Unlike TRPV4 knockout mice which display increased susceptibility to acoustic injury (Tabuchi et al., 2005), mice carrying two inactive *Trpml3* alleles did not show increased acoustic vulnerability.

3.3.1.9. Motor coordination tests in *Hprt*$^{Cre/+}$; *Trpml3*$^{+/+}$ and *Hprt*$^{Cre/+}$; *Trpml3*$^{\Delta/\Delta}$ mice

Besides evaluating the auditory system, the vestibular function was also assessed. Genetic *Trpml3* inactivation did not result in circling behavior, imbalance, head bobbing, or waddling and they could walk along the top of a 3 mm thin wall, suggesting normal vestibular function (data not shown). To obtain more objective and quantitative data on potential balance deficits, Rotorod tests (Jones and Roberts, 1968) were performed in collaboration with Dr. Lars Becker. A four track Rotarod instrument was used to test for a balance and motoric impairment in 3-month-old *Hprt*$^{Cre/+}$; *Trpml3*$^{+/+}$ and *Hprt*$^{Cre/+}$; *Trpml3*$^{\Delta/\Delta}$ mice. There was no significant difference between both genotypes for the 6-day-period tested (Fig 38), indicating that inactivation of *Trpml3* does not lead to balance defects in this test.

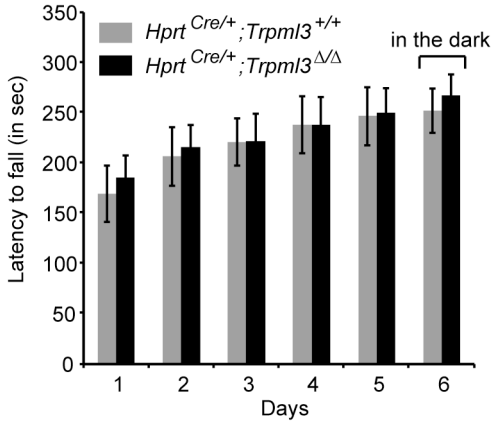

Figure 38: Rotarod experiments. A: The average latencies to fall ±SEM (in sec) are shown for three-month-old *Hprt*$^{Cre/+}$*; Trpml3*$^{+/+}$ (n=8) and *Hprt*$^{Cre/+}$*; Trpml3*$^{\Delta/\Delta}$ (n=8) mice. The experiment was executed over a time range of 6 days. For testing, the mice were placed onto the Rotarod for a 330 sec trial with constant acceleration from 3 rpm to 40 rpm. Four trials with 45 min inter-trial periods were performed each day. The day 6 experiment was performed in the dark to exclude compensation via visual cues. The difference between genotypes was not statistically significant at any given time point ($p>0.05$, one-way ANOVA, followed by Tukey's post test). (Data were kindly provided by Dr. Lars Becker.)

4. Discussion

4.1. Survival of varitint-waddler sensory hair cells

The function of TRPML3 in the cochlea has not yet been elucidated. The varitint-waddler mouse model is providing us with invaluable tools not only to gain access to study TRPML3, but also to gain access to the molecular basis of hearing and deafness. The varitint-waddler mutation of TRPML3 leads to constitutive activity of this TRP channel, which is expressed by inner ear sensory hair cells. TRPML3 mutant isoforms result in depolarization by an inwardly rectifying leak conductance (Grimm et al., 2007; van Aken et al., 2008). Cells that express this mutant TRPML3 isoform undergo rapid apoptosis. Varitint-waddler sensory hair cells, however, are able to survive with mutant TRPML3 for weeks before they ultimately degenerate.

In the first *Results* chapter, the mechanism by which sensory hair cells are able to deal with a severe Ca^{2+} overload caused by constitutive activity of the TRPML3 channel in varitint-waddler mice was investigated. Leading to this study were *in vitro* pilot experiments, which had revealed that coexpression of PMCA2, a highly effective plasma membrane calcium ATPase, significantly reduced $[Ca^{2+}]_i$ increase and apoptosis in HEK293 cells expressing TRPML3(A419P) or TRPML3(I362T/A419P). The deaf-waddler isoform of PMCA2(G283S), which operates at 30% activity when compared with wild-type PMCA2, showed a significantly decreased ability to rescue the Ca^{2+}-loading of cells expressing TRPML3(A419P) when compared with wild-type PMCA2. This observation led to the conclusion that cell death is caused by massive intracellular Ca^{2+} overload. This finding also explains why sensory hair cells of varitint-waddler mice that express the mutant TRPML3 channel during the first postnatal week (Di Palma et al., 2002; van Aken et al., 2008) are able to survive for several weeks after birth. Numerous mobile Ca^{2+} buffers (Edmonds et al., 2000; Heller et al., 2002) and highly efficient Ca^{2+} extrusion mechanisms (Yamoah et al., 1998; Dumont et al., 2001) that control local Ca^{2+} homeostasis in the hair bundle and at synaptic sites have been identified in hair cells. I therefore hypothesized that the survival of varitint-waddler sensory hair cells is linked to their ability to deal with Ca^{2+} loads due to the abundance of PMCAs and hair cells could adapt, at least temporarily, to the otherwise devastating A419P varitint-waddler mutation of TRPML3 (Fig. 39).

To test this hypothesis *in vivo*, I used the naturally occurring deaf-waddler mutation. Deaf-waddler mice express a less efficient mutant isoform of PMCA2. Since PMCA2 is one of the major Ca^{2+} clearing proteins in hair cells, I hypothesized that a slight reduction in the Ca^{2+} extrusion ability of hair cells would increase the severity of the varitint-waddler phenotype. I expected that the combination of both alleles would worsen the hair bundle defects and hair cell loss compared to the respective single mutants.

The deaf-waddler mutation was selected because its heterozygous phenotype is relatively mild compared with the phenotype of the heterozygous varitint-waddler mutation. Heterozygous mice for the varitint-waddler mutant allele were crossed with mice heterozygous for the deaf-waddler mutant allele, which generated mice that carried both mutations. These mice were analyzed for hair cell morphology in the organ of Corti and utricle at P10 and P21. Combination of the mutant alleles led to more severe hair cell bundle defects as well as increased hair cell loss when compared to mice heterozygous for each mutant allele alone. These results indicated that the reduction of PMCA2 efficiency that normally does not lead to any cellular or phenotypical defects in heterozygous animals, amplifies the effect of TRPML3(A419P) in hair cells. Furthermore, heterozygous double mutants lack auditory brainstem responses, even when stimulated with 120 dB of hearing level, which is a more severe phenotype than that detected in their respective littermates containing only single mutant alleles. Likewise, heterozygous double mutant mice exhibited severe circling behavior, which was not observed in heterozygous varitint-waddler or deaf-waddler mice, an indication that also the vestibular system, likely via increased degeneration of vestibular hair cells, is affected by combining TRPML3(A419P) with the defective PMCA2(G283S) Ca^{2+} pump.

In the cochlea, the observed effect of reducing PMCA2 efficacy was only significant in outer hair cells, whereas inner hair cell degeneration appeared not further enhanced by addition of deaf-waddler mutant alleles. This result can be explained by the lower expression of PMCA2 and the presence of PMCA1 in inner hair cells compared to outer hair cells (Dumont et al., 2001).

In this study, I have shown that sensory hair cells are able to deal with a constitutive active TRPML3 channel, which when overexpressed in HEK293 cells results in rapid cell death. I also have demonstrated that the durability to resist sustained Ca^{2+} loads is due to the inherent ability of hair cells to buffer and extrude Ca^{2+}, which normally enters hair cells via active mechanoelectrical transduction channels and synaptic Ca^{2+} channels. These buffering and extrusion mechanisms are able to delay imminent cell death for several

weeks. This extraordinary robustness of inner ear hair cells to deal with sustained Ca^{2+} influx implies that Ca^{2+}-loading is an unlikely primary cause of hair cell death in ototoxic stress situations. Ototoxic stress situations, such as noise trauma, have previously been linked to hair cell death by Ca^{2+}-loading (Fridberger et al., 1998). My results argue against such mechanism, which is an important finding in the context of ototoxicity and causes of hearing loss. Beside Ca^{2+}-loading, the mechanical damage of stereocilia and their rootlets has also been discussed as detrimental factors causing hair cell death in stress situations (Duncan and Saunders, 2000), and my results imply that these factors might play more pronounced roles in hair cell loss than previously thought.

Overall, *in vitro* and *in vivo* results show that even massive Ca^{2+}-loading is not immediately toxic for hair cells, which highlights that hair cell death in response to overstimulation involves other, more subtle mechanisms.

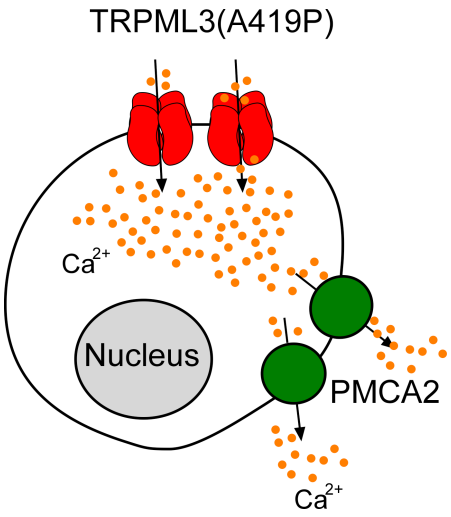

Figure 39: Schematic model of a cell expressing TRPML3(A419P) and PMCA2. Cell death in presence of constitutively active TRPML3(A419P) (in red) is caused by massive intracellular Ca^{2+} (in orange) overload. If PMCA2 (in green) is coexpressed, Ca^{2+} is extruded from the cells, resulting in comparably long survival.

4.2. Small molecule activators of TRPML3

TRPML3 has recently become the focus of intense research and a recent study reported activation of the channel by decreasing the extracellular Na^+ concentration (Kim et al., 2007). In the second *Results* part, I presented the first activators of TRPML3, found in a high-throughput screen of 217.969 compounds. Fifty-three selective small molecule activators were identified and confirmed using calcium imaging and patch clamp analyses. Although the majority of the compounds were sulfonamides, they displayed a wide variety of structures belonging to nine chemical scaffolds and 20 singletons. The detailed analysis of 15 compounds revealed that these molecules activated the channel with distinct kinetic profiles. The maximal response levels also varied between compounds. The strongest and most rapid responses were obtained with compounds SF-21, SF-41, and SN-2. In this study, I also presented data that showed that SF-11 elicited responses when applied intracellular, which indicates that this compound is either cell permeant or that it is able to act on intra- and extracellular sites of TRPML3. Beside that, some of the compounds were able to activate the related TRPML1 and TRPML2 channels. Therefore, I concluded that the TRPML3 activators open the channel by multiple mechanisms. Further experiments are necessary to reveal the specific mechanisms by which the compounds open TRPML3, and on which domain they act. TRPML3 mutants that are still localized to the plasma membrane could be used to identify the site of compound action. Furthermore, the collection of different TRPML3 activators provides an unprecedented set of novel tools to study the biophysical and physiological characteristics, and possibly the function of TRPML3.

Towards these goals, our group has already analyzed the relationship between compound activation and regulation of TRPML3 by extracellular Na^+ (Grimm et al., 2010). The regulation by Na^+ is an interesting feature of wild-type TRPML3, because the transient expression of TRPML3 in the apical plasma membrane of sensory hair cells in the mouse cochlea (van Aken et al, 2008) coincides with changes of the ionic composition of the cochlear endolymph. The endolymph is the extracellular solution of the cochlear *scala media* into which the mechanosensitive hair bundles protrude. TRPML3 expression is strong from P2 to P6 in cochlear hair cell stereocilia, where it localizes toward the stereociliary base (van Aken et al. 2008). At P10, TRPML3 immunoreactivity appears to diminish in cochlear hair cells (van Aken et al., 2008), although I was able to detect expression of TRPML3 mRNA in the organ of Corti by RT-PCR throughout neonatal development and in adult animals (Fig. 6). TRPML3 is regulated by changes in the

extracellular Na^+ composition and it is conceivable that native TRPML3 is a constitutively active channel that is blocked by extracellular Na^+ (Kim et al. 2007; Kim et al. 2008). The composition of the endolymph, the fluid in which the hair bundles protrude, is drastically changing during the first neonatal week and the consequential decrease of Na^+, accompanied by an increase of K^+, could lead to the activation of TRPML3 during a time that is critical for hair bundle, hair cell, and organ of Corti development. Between P0 and P5, the endolymphatic Na^+ drops from 36 mM to 4.1 mM. At P7, all ions reach adult concentration (low Na^+ 2.8 mM and high K^+ 202 mM) (Yamasaki et al, 2000), while TRPML3 immunoreactivity is starting to disappear in stereocilia (Di Palma et al., 2002; van Aken et al., 2008). Exposing wild-type TRPML3 to endolymph-like solution resulted in channel activation visualized by appearance of an inward rectifying current (Grimm et al., 2010). The maximal amplitudes were dependent on the extracellular Na^+ concentration. TRPML3 was activated when Na^+ dropped below 20 mM, and its activation was gradually more efficient when the Na^+ was stepwise lowered to 2 mM, which elicited the maximal response. This concentration range matches the Na^+ concentration changes during the neonatal maturation of cochlear endolymph (Yamasaki et al, 2000). We tested the relationship between low extracellular Na^+ and the activators SN-2 (high efficient compound) and SF-24 (low efficient compound), and found strong synergism between them in activation of TRPML3. In addition, we confirmed that Na^+ is not an inactivator of TRPML3 because compound activation happens in high extracellular Na^+ (138 mM). Nevertheless, lowering Na^+ to 2 mM led to a 10-fold increase of the current response (Grimm et al., 2010). These results indicate that the two activation mechanisms are cooperatively acting on TRPML3.

Elicited responses in TRPML1(NC) and TRPML2-expressing HEK293 cells:

TRPML1 and TRPML2 are primarily localized in the late endosomes and lysosomes (Treusch et al., 2004; Venkatachalam et al., 2006). Localization and the inactivity of the available wild-type proteins make it difficult to characterize their channel properties. Interestingly, some of the TRPML3-activating compounds also elicited significant Ca^{2+} influx in TRPML1(NC) (SF-22) and TRPML2 (SF-21, SF-41, and SF-81)-expressing cells. Our collaborator Dr. Alexander Obukhov has shown that the compound SF-22 does not penetrate the plasma membrane, which is a strong indication that the TRPML1(NC) mutant is localized to the plasma membrane because SF-22 can only act on an extracellular site of TRPML1. Future studies on wild-type TRPML1, which is

intracellular, using SF-22 will require lysosome patch clamp techniques. The cell permeation of TRPML2-activating compounds SF-21, SF-41, and SF-81 has not been determined yet. But in general, these compounds offer the opportunity to fully characterize the wild-type channel properties of TRPML1 and TRPML2 *in vitro* and *in vivo*. Furthermore, the structure of these compounds could be used to design and develop new and more specific activators or even inhibitors for TRPML1 and TRPML2.

Cochlear hair cells expressing TRPML3 do not respond to compound activators:

Neonatal cochlear hair cells that natively express TRPML3 were investigated whether they are able to elicit TRPML3 responses when exposed to compound activators. Surprisingly, none of the tested compounds evoked TRPML3 activity in sensory hair cells, even at very high compound concentrations. Also in combination with endolymph-like solution, which led to a 10-fold increase of current responses *in vitro*, did not elicit responses from cochlea hair cells. The potential explanation offered for this result is that albeit TRPML3 is located in the postnatal hair cell plasma membrane, it might be somehow modified or inhibited. The plasma membrane-bound TRPML3 might be strictly regulated by endocytotic removal of the channel from the plasma membrane, which may cause hair cells nonresponsiveness. Even if some TRPML3 channel would be present in the plasma membrane, there contribution to a whole cell response might have been below electrophysiological detection levels. A second possibility is that the identified TRPML3 activators might act only on homomeric TRPML3 channels and these homomers only form when TRPML3 is overexpressed. The high throughput screen and follow-up experiments were performed in HEK293 cells overexpressing homomeric TRPML3. In sensory hair cells, TRPML3 may be a subunit of a more complex channel of unknown composition, which is not responsive to TRPML3 compound activators.

The lack of reliable commercially available TRPML3 antibodies made it difficult to detect and therefore to confirm previous studies that demonstrate expression of endogenous TRPML3 in the plasma membrane of cochlear hair cells. For this reason, I cannot rule out the possibility that TRPML3 is not present in hair cell plasma membranes. If this were to be the case, the varitint-waddler phenotype (Di Palma et al., 2009; Grimm et al., 2007) would have to be caused by mislocalization of the constitutively active TRPML3(A419P) isoform to the plasma membrane. Furthermore, cochlea hair cells from varitint-waddler mice showed TRPML3 current (Grimm et al., 2007, van Aken et al., 2008), proving TRPML3 as an active channel when located to the plasma membrane.

Human primary epidermal melanocytes expressing TRPML3 show no or only small responses to compound activators:

Epidermal melanocytes also natively express TRPML3. This cell type is more suitable for *in vitro* inquires than sensory hair cells because melanocytes can be transfected with expression vectors. In my study, I showed that the compounds elicited no or only very small responses, with the exception of SN-2, which at elevated concentrations elicited a robust increase of the intracellular Ca^{2+} concentration. This observation raised the question whether SN-2 might act nonspecifically. I was proving in calcium imaging experiments that SN-2 did not show any responses on other TRP channels, not even on the related TRPML1 and TRPML2. Second, I demonstrated that SN-2 is not cell permeant, which leads to the conclusion that its action on melanocytes is based on an interaction with an extracellular site. To further investigate this, I used the channel-inactive dominant negative TRPML3 isoform TRPML3(D458K), which was recently reported by Kim et al., 2009. TRPML3(D458K) exerts a strong dominant negative effect on wild-type TRPML3 when coexpressed in HEK293 cells. Expression of TRPML3(D458K) in primary human melanocytes completely abolished SN-2 activation, which demonstrates that the weak Ca^{2+} increase elicited by SN-2 could be inhibited by a dominant negative isoform of TRPML3. This result confirmed that the SN-2 effect is not an artifact but rather that SN-2 activates a channel that is not responsive in presence of TRPML3(D458K). Such dominant negative action might be due to potential heteromerization of TRPML3(D458K) with the SN-2 responsive channel. Future studies, e.g. direct comparison of skin melanocytes from wild-type and knockout *Trpml3* animals, will be necessary to investigate this idea more in detail. I would expect that melanocytes, isolated from *Trpml3* knockout mice, would not respond with intracellular Ca^{2+} increase to SN-2 compound application.

Based on results in sensory hair cells and primary epidermal melanocytes, it can be hypothesized that the presence of TRPML3 in the plasma membrane might be limited or tightly regulated. Native TRPML3 might be modified such that the modification renders TRPML3 nonresponsive to most compounds. In addition, heteromerization could regulate TRPML3. In this case, TRPML3 proteins would interact with related ion channel proteins, resulting in either altered channel properties or translocation from the plasma membrane to intracellular compartments. A heteromerization relies on the endogenous expression of other channel proteins capable of interacting with TRPML3. I detected TRPML1 and TRPML2 mRNA in the inner ear and in epidermal melanocytes, which would make heteromerization with TRPML1 and TRPML2 a possibility in these cell types.

TRPML1 changes compound responsiveness of TRPML3:

Interactions between TRPML proteins have been reported in overexpression studies many times using diverse methods (Venkatachalam et al., 2006; Curcio-Morelli et al., 2009; Grimm et al., 2010; Zeevi et al., 2009; for a review, see Puertollano and Kiselyov, 2009). I also showed that TRPML1 has an impact on the subcellular localization of TRPML3. TRPML1 is located in intracellular compartments, whereas TRPML3 is located in intracellular vesicles and plasma membrane when expressed in HEK293 cells. TRPML3 localization altered when it was coexpressed with TRPML1. More TRPML3 protein was localized intracellular, where TRPML3 colocalized with TRPML1. Based on this result, I hypothesized that TRPML1 has a strong impact on the subcellular localization of TRPML3, and it is regulating the ratio of TRPML3 in the plasma membrane directly by "pulling" TRPML3 out of the plasma membrane. In contrast to my hypothesis, it has been reported that in native cells, TRPML3 is largely segregated from TRPML1. Implying that coexpression of both proteins in native cells and tissue does not essentially mean that TRPML channels are targeted to the same subcellular locations (Kim et al., 2009; Zeevi et al., 2009).

If TRPML1 is able to affect TRPML3, I would expect that coexpression of TRPML1 will reduce the TRPML3 response upon compound application. Indeed, I confirmed that TRPML3 activation was inhibited by coexpression of TRPML1. Furthermore, the plasma membrane-localized TRPML1 mutant isoform (TRPML1(NC)) restored responsiveness, albeit only partially. It resulted in a smaller reduction of compound responsiveness of TRPML3 than coexpression with wild-type TRPML1. Coexpression of TRPML3 with TRPML2, on the other hand, did not lead to a decreased responsiveness to compounds. Generally, these data support my hypothesis that the interaction with TRPML1 generates TRPML1/TRPML3 heteromers that preferentially localize to intracellular compartments. Wild-type TRPML1 is able to regulate the ratio of TRPML3 in the plasma membrane, which very likely partially accounts for the reduced responsiveness to compound activation in HEK293 cells. Nevertheless, epidermal melanocytes expressing shRNA to TRPML1 did not display increased responses to TRPML3 activators when compared with control cells. This result is indicating that native TRPML1 expression was either too strong for efficient suppression with shRNA or that the lack of TRPML3 responsiveness in melanocytes was due to additional mechanisms independent of TRPML1. As mentioned above, this hypothesis was supported by recent reports arguing the colocalization of TRPML1 and TRPML3 *in vivo* accounts only for a small fraction of the channel

populations and that TRPML3's subcellular localization is not only determined by its interaction with TRPML1 (Kim et al., 2009; Zeevi et al., 2009).

It was discussed that many TRP channels appear to have long turnover times, and effective knockdown can take many days after the introduction of shRNA in cells (Desai and Clapham, 2005). This can often give the cells enough time to adapt and readjust their need for a particular TRP channel by gradually upregulating the activities of redundant machinery. Therefore, the risk of false-negative results and lost opportunities is there. In HEK293 control cells, TRPML1 and shRNA plasmids were introduced at the same time and expressed at the same time, which might make it easier for the shRNA to interfere. Whereas in melanocytes, native TRPML1 protein was already present. To ultimately prove whether TRPML1 expression is indeed reduced in transfected melanocytes, quantitative RT-PCR, immunocytochemistry, and Western blot analyses should be performed. Due to the low transfection efficiency of human melanocytes, RT-PCR and Western blot analyses were however no suitable methods for quantification. Immunocytochemistry with specific antibodies to human TRPML1 would at least have provided some visual evidence for the reduction in expression, but unfortunately no specific antibody to hTRPML1 was available from commercial or academic resources.

TRPML3 as autoregulator of autophagy:

TRPML3 may play an active role in formation of the autophagosomes (Kim et al., 2009). The authors proposed that the cellular localization of TRPML3 is dynamic. TRPML3 recycles between the plasma membrane and intracellular compartments via a dynamin dependent endocytic pathway. The dominant negative isoform K44A of dynamin increases TRPML3 localization in the plasma membrane. Therefore, I hypothesized that coexpression of wild-type dynamin with TRPML3 in HEK293 cells results in a decreased response to TRPML3 activators, whereas coexpression of mutant dynamin K44A with TRPML3 causes increased Ca^{2+} influx after the application of TRPML3 activators. To test this hypothesis *in vitro*, I coexpressed wild-type dynamin or the K44A mutant of dynamin with TRPML3 in HEK293 cells. The expression of wild-type dynamin with TRPML3 resulted in small response increases in HEK293 cells, and on the other hand, the expression of the K44A dynamin mutant reduced responses to TRPML3 activators. These data supported the idea that TRPML3 might recycle between the plasma membrane and intracellular compartments. Thus, autophagy might play an important role as a tight regulator of TRPML3 in the plasma membrane. Unfortunately, overexpression of dynamin

K44A in human epidermal melanocytes had no effect on native TRPML3 activator responsiveness.

The sum of differences observed between the overexpression studies in HEK293 cells and the expression in primary cells highlights the limitations of cell culture experiments to study trafficking and physiology of TRPML3. Nevertheless, in conclusion, the data showed that melanocytes and sensory hair cells do not express activator responsive TRPML3 in their plasma membrane. Nonresponsiveness could be a result of the absence of the channel protein from the surface of the cells, or it could mean that TRPML3 exists primarily as a subunit of heteromeric channels *in vivo*. Electrophysiological recordings could have helped to shed light on the question whether endogenous TRPML3 is localized in the plasma membrane or in intracellular compartments in primary melanocytes. Our group has attempted to record from human primary melanocytes, but was unable to obtain reliable seals of the recording electrode with the melanocyte plasma membranes. The combination of poor transfection efficacy, small cell size, and weak attachment to the substrate made this experiment highly unfeasible. Just recently, expert electrophysiologists have been able to reliably record from primary human melanocytes, an achievement that was one of the main points of a recent publication (Oancea et al., 2009).

Lack of TRPML3 antibodies:

Although previous data have shown that overexpressed TRPML3 can recycle between the plasma membrane and endosomal compartments, the localization of endogenous TRPML3 remains poorly understood. The lack of reliable commercially available antibodies makes it difficult to detect endogenous TRPMLs. For this reason, most of the studies on TRPMLs have been made on epitope-tagged recombinant proteins that might potentially be mistargeted because of overexpression. Surface biotinylation would be a key method to show that endogenous TRPML3 is present in the plasma membrane of cells used in my study. However, surface biotinylation requires unequivocally good antibodies that work in Western blots and immunoprecipiation. I have tested a battery of different polyclonal antibodies to TRPML3 and none of the antibodies turned out to have the necessary specificity and sensitivity.

4.3. Genetic *Trpml3* inactivation does not lead to hearing and vestibular impairment in mice

The discovery of the TRPML3 varitint-waddler mutation A419P with its severe auditory and vestibular phenotype made this protein particularly interesting for inner ear biology. Mutant mice are providing us with invaluable tools to gain access to the molecular basis of hearing and deafness. To elucidate the physiological role of murine TRPML3 in the inner ear, a conditional genetic inactivation of *Trpml3* in mice was successfully generated by using Cre-lox and Flp-FRT technology. It was decided to target exon 11 of *Trpml3*, which encodes the pore-loop domain and the pore lining TM6 of the ion channel. Therefore, it is expected that the deletion of exon 11 leads to an effective inactivation by destroying the core domain of the *Trpml3* channel gene, the pore. With the conditional strategy, gene targeting can be controlled both spatially and temporally; therefore, the function of TRPML3 can be studied in the desired cell types and at specific time points. This dissection allows investigating gene function in many different situations, including development, physiology, and behavior (Utomo et al., 1999).

Despite the strong evidence that TRPML3 is involved in hearing (Di Palma et al., 2002), no overt inner ear phenotype was detectable in mice with ubiquitous *Trpml3* inactivation or when the gene was inactivated from P0 to P3 onwards.

Auditory brainstem response measurements revealed no significant differences in ABR thresholds and interwave latencies. These results suggested that TRPML3 is not essential for hair cell function, synaptic signal transmission, performance of spiral ganglion neurons, and auditory nerve function. As discussed, the inactivation of *Trpml3* using $Hprt^{Cre}$-mediated recombination was introduced very early in development, compensation effects cannot be excluded with this approach. Therefore, to circumvent potential compensatory mechanisms, tamoxifen inducible *Math1-CreER*^{TM} mice (Chow et al., 2006) were used to inactivate TRPML3 in cochlear hair cells between P0-P3. However, the use of *Math1-CreER*^{TM} mice did not reveal potential compensatory mechanisms of *Trpml3* inactivation. But these experiments have two important limitations. First, the tamoxifen inducible recombination in cochlear hair cells is not complete, as revealed by analysis of crosses of *Math1-CreER*^{TM} mice with *Rosa26-lacZ* reporter mice (Chow et al., 2006). Therefore, a number of cochlear hair cells might have been unaffected by Cre-mediated recombination. Second, three weeks of loss of TRPML3 function might be enough for potential compensatory mechanisms to become effective. Nevertheless, as long as there

are no clear candidates or mechanisms known that could provide compensation for inactivation of *Trpml3*, it is difficult to speculate about the timing of compensatory mechanisms. In summary, the use of *Math1-CreER*^{TM} mice did not reveal potential compensatory mechanisms of *Trpml3* inactivation. However, due to the limitations of this experiment, it cannot be excluded that loss of TRPML3 function is being compensated by an unknown mechanism.

An important question is whether the mutant TRPML3 channel is expressed in *Trpml3*$^{\Delta/\Delta}$ mice. RT-PCRs of specific cDNA sequences indicated that mRNA was still expressed in mutated mice, however, splicing occurred between exon 10 and exon 12, resulting in a shorter message encoding a protein lacking the pore loop and TM6. Immunohistochemistry of TRPML3 in both wild-type and mutant animals would have been a useful tool to demonstrate whether the mutant *Trpml3* splice variant encodes a pore-less TRPML3 channel and whether that channel is correctly localized. However, the lack of reliable commercially available antibodies to detect endogenous TRPML3, makes the use of immunohistochemistry not an option. In addition, the heterologous expression of the pore-less mutant TRPML3(Δ exon11) in HEK293 cells showed that the mutant channel of *Trpml3*$^{\Delta/\Delta}$ mice is clearly inactive and mislocalized. Consequently, even if there was a specific antibody available, TRPML3 protein would be very likely detected in immunohistochemistry. Therefore, this experiment would be inconclusive.

The lack of significant differences in ABR thresholds or interwave latencies supports the previous conclusion that the TRPML3(A419P) mutation of varitint-waddler mice is a gain of function mutation, which has been hypothesized to cause Ca^{2+}-loading of cells and subsequently apoptotic cell death (Grimm et al., 2007; Kim et al., 2007; Xu et al., 2007; Nagata et al., 2008; Grimm et al., 2009). Loss of functional *Trpml3*, on the other hand, is not causing a detectable phenotype in the inner ear. Moreover, *Hprt*$^{Cre/+}$; *Trpml3*$^{\Delta/\Delta}$ mice were indistinguishable from their wild-type littermates in size and weight. *Trpml3*$^{\Delta/\Delta}$ mice inherited the mutation stably and homozygous mutant animals displayed normal breeding performance. Several scenarios could explain for the lack of a detectable phenotype in *Trpml3*$^{\Delta/\Delta}$ mice. The first possibility is that the native TRPML3 channel as a homomer is not essential for detectable inner ear function and development *in vivo*. Another possibility is that the used tests were not sufficient to reveal more subtle roles of TRPML3 such as potential modulatory roles in hair cells or other parts of the auditory and vestibular system. Furthermore, it is possible that native TRPML3 proteins are dispensable subunits of heteromeric channels. A different TRP channel, such as the related TRPML1 and

TRPML2 might compensate for the loss of TRPML3. Heteromerization of TRPML channels has been shown and discussed previously (Venkatachalam, 2006; Grimm et al., 2010). This hypothesis is supported by my observation that a dominant negative isoform of TRPML3(D458K), when transfected into primary epidermal melanocytes, is able to inhibit the activation of a presumptively heteromeric channel consisting of TRPML3 and other unknown subunits (Grimm et al., 2010). Such a compensatory mechanism is potentially testable by generation of mice with inactivating mutations in *Trpml3* and one or more additional genes that encode potential heteromeric subunits. This strategy might ultimately reveal the physiological function of TRPML3-containing channels in sensory hair cells and other cell types.

Generation of a dominant negative *Trpml3* mouse model:

The functional significance of TRP heteromers can be addressed using mice where dominant negative variants of TRP channels were knocked-in. This approach is likely to yield phenotypes and lead to hypotheses about regulation and function of distinct TRP heteromers. Previously, I have discussed that the dominant negative TRPML3(D458K) mutant eliminates responses to TRPML3 activators. Therefore, this mutation could be introduced into the mouse *Trpml3* gene. TRPML3(D458K) is heteromerizing with its partners, thereby likely inactivating the pore function. I hypothesize that this malfunction would introduce a stronger phenotype than the knockout if TRPML3 is indeed a subunit of unknown heteromeric channels.

Generation of TRPML double or triple knockouts:

The *Trpml3* inactivation does not lead to an overt phenotype in the inner ear in mice, as many other single TRP channel knockouts (reviewed in Corey, 2006 and Cuajungco et al., 2007). It has been hypothesized that the original function of a lost TRP channel can remain if compensatory genes encoding related channels are upregulated. Generation of double and triple knockouts by crossbreeding mice deficient in related TRP channels is likely to attract a great deal of attention in this regard. The $Trpml1^{\Delta/\Delta}$; $Trpml3^{\Delta/\Delta}$ double knockout mouse could be generated by crossing the existing $Trpml1^{\Delta/\Delta}$ knockout mouse (Micsenyi et al., 2009) with the $Trpml3^{\Delta/\Delta}$ mouse. The question whether or not TRPML1 and TRPML3 are colocalized in different compartments could be answered with this mouse model as well. The generation of the $Trpml2^{\Delta/\Delta}$; $Trpml3^{\Delta/\Delta}$ double knockout mouse model is more difficult. *Trpml2* and *Trpml3* genes are located in tandem on the mouse

chromosome 3, in an approximately 16 kb segment that could be deleted by Cre-mediated recombination. There is no other known gene located on this particular genomic segment, which makes it unlikely that the manipulation would result in an unwanted phenotype. The genomic target could begin upstream of the *Trpml2* exon 1 and targeted introduction of an additional *loxP* site into the existing *Trpml3* embryonic stem cell line (1E5FlpC12), which only contains the two *loxP* sites flanking the exon 11 of *Trpml3*, which would result in a floxed region embracing all of the coding *Trpml2* exons and exons 1-11 of *Trpml3*. After crossing, this double-targeted mouse model with a Cre mouse line, *Trpml2* and most of *Trpml3* will be deleted. This double knockout mouse line could be crossed with the *Trpml1*$^{\Delta/\Delta}$ knockout mouse to generate a triple TRPML knockout mouse model. This strategy, which is currently being pursued in my host laboratory, aims to systematically inactivate first one, then two, and finally three TRPML channel genes.

Novel TRPML3 interaction partners:

It has been previously reported that the introduction of proline substituations into TM5 of TRP channels revealed potential structural relationship between TRPML channels and TRPV5 and TRPV6 (Grimm et al., 2007). When TRPV5 and TRPV6 were mutated at the exactly equivalent position to TRPML3's A419P, the channels displayed high constitutive activity. The proline substitutions did not lead to constitutive activity with a battery of other TRP channels tested (Grimm et al., 2007). In addition to this first link between TRPML and TRPV5 and TRPV6 channels, a conventional sequence alignment revealed a novel subgroup consisting of TRPMLs and TRPV5/6. Conventional sequence alignments of all known TRP channel amino acid sequences using the multi align algorithm Clustal confirmed the existing TRP subunit classification (Fig. 40). However, when the sequence comparison was done with TM5 only, the pore region, and TM6, the principal domains that interact to form the multimeric pore region, the TRPML channels and TRPV5 and TRPV6 form their own new subfamily (Fig. 40). All other TRP channels remained within their respective subfamilies. This observation might be an indication that TRPML channels and TRPV5 and TRPV6 could form a novel TRP subfamily, and that the core regions of these proteins are related based on amino acid sequence homology.

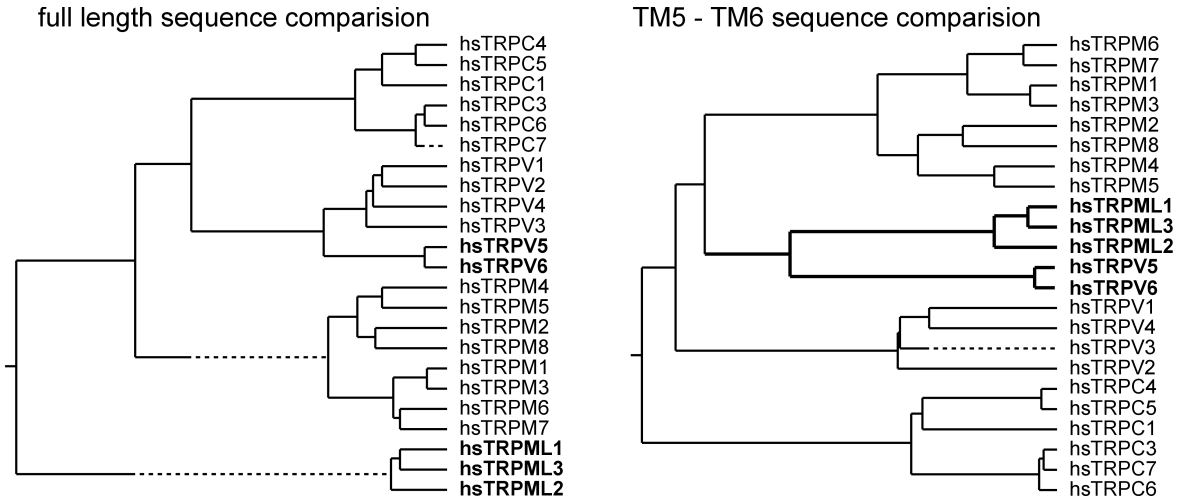

Figure 40: Conventional sequence alignment. Cladograms based on sequence comparison reveal a new TRP subfamily consisting of TRPMLs and TRPV5/6 channels, when the sequences used for comparison were restricted to TM5, the pore region, and TM6 for each TRP channel protein. Several, more distantly related channels (inclusive TRPP, TRPA1) were omitted for clarity.

Using FRET technique with the respective CFP and YFP-tagged fusion proteins of each channel in both directions, we found that TRPML3 heteromerizes with members of TRPV channels (Fig. 41). The average FRET efficiencies were between 13-20% for TRPML homo- and heteromers, and FRET efficiency between 10-20% for TRPML and TRPV5/6 homo- and heterotetramers. FRET effects between TRPC6, TRPV2, TRPM2, or PKD2 and TRPML3 showing average FRET efficiency of 5% and less were regarded as unspecific. In contrast, TRPC5 homomers displayed an average FRET efficiency of 17%, PKD2 homomers displayed an average FRET efficiency of 19%. These data are in accordance with FRET efficiencies previously reported for TRPML channels, TRPV5/6, or TRPC6 (Venkatachalam et al., 2005; Hofmann et al., 2002; Hellwig et al., 2004). This positive FRET-based interaction between TRPML3 and TRPV5 and TRPV6 suggests that these channels are able to form heteromeric novel TRP channel combinations. Therefore, this interaction could account for the compensation of TRPML3 inactivation in the inner ear as well as for the nonresponsiveness of sensory hair cells to TRPML3 compound activators. Based on RT-PCR data, it is known that TRPV5 and TRPV6 are also expressed in the organ of Corti (Asai et al., 2009, and data not shown).

However, these results will subsequently need further verification. The interactions have to be confirmed by an additional method, such as Co-immununoprecipitation assays, and the functionality of heteromeric TRPML/TRPV channels has to be tested using patch clamp recordings.

Such interactions could be important for channel localization, assembly, gating, and conductance properties. It is important to study the possibility of multimeric formation of TRPV members with TRPML channels and of TRPML channels with each other in order to understand the full extent of their functional and pharmacological diversity.

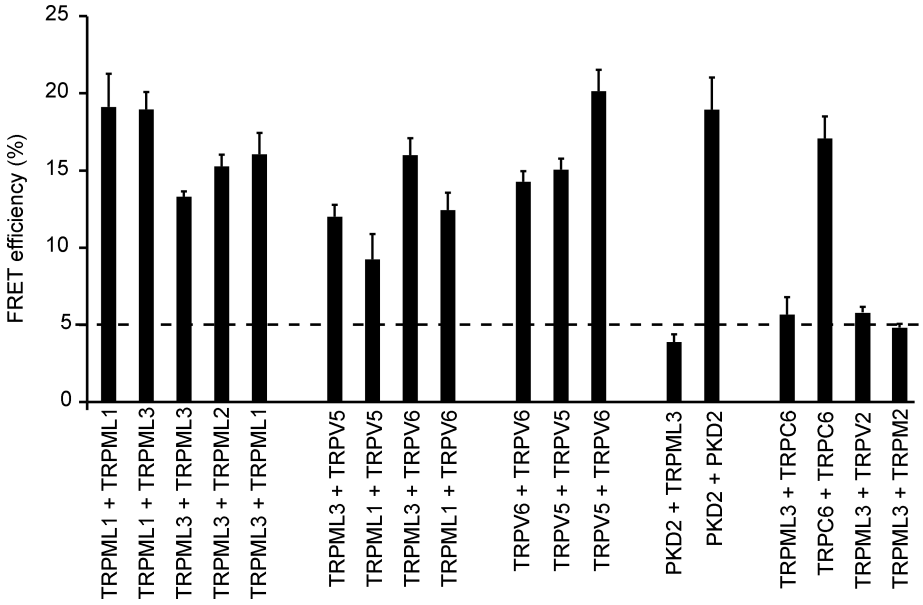

Figure 41: Fluorescence Resonance Energy Transfer (FRET) measurements with different TRP channels overexpressed in HEK293 cells. Shown are average FRET efficiencies between different TRP channel homomers and heteromers. Mean values ±SEM. All FRET experiments were performed using the monochromator-based imaging system. FRET efficiencies were determined by monitoring the increase in the CFP (FRET donor) fluorescence emission during selective YFP (FRET acceptor) photobleaching. The photo-bleaching protocol consists of 15 cycles with 40 msec/cycle exposures at 410 nm for CFP detection and 8 msec/cycle at 515 nm for YFP detection. In each experiment, data of 3-6 single cells were averaged. (Data were kindly provided by Dr. Christian Grimm.)

Is TRPML3 part of the hair cell mechanotransduction apparatus?:

An obvious question that is not easily addressable is whether TRPML3 is part of the hair cell transduction channel. Based on studies with TRPML3 small compound activators and the conditional *Trpml3* inactivation, I proposed that either TRPML3 might be limited in the plasma membrane or that TRPML3 does not exist as a homomeric channel in hair cells and other native cell types. The generated genetic inactivation might reveal whether TRPML3 is an essential component of the transduction apparatus. Although *Trpml3*$^{\Delta/\Delta}$ mice have no hearing impairment, hair cells in the cochlea and utricle have to be examined whether the transduction currents in response to bundle deflection is normal in terms of current amplitude, time course, and the extent of adaptation.

TRPML3 and neuropathic pain:

Recently, it has been shown that TRPML3 is strongly and permanently upregulated in a rodent model of neuropathic pain (Staaf et al., 2009). Neuropathic pain is caused by damage to primary sensory afferent neurons of the peripheral nervous system that relay nociceptive and non-nociceptive peripheral stimuli to the spinal cord and the brain as a result of trauma, diabetes, cancer, or chemotherapy (Brooks and Tracey, 2005; Ji and Strichartz, 2004). Following nerve injury, dorsal root ganglia (DRG) were isolated and quantitative RT-PCRs of all known TRP channels were performed. TRPML3, which was not described before in DRGs, was highly upregulated in animals exhibiting neuropathic pain behavior compared to control animals. Even three month after the incident TRPML3 was still upregulated. The strong and long-lasting upregulation of TRPML3 suggests a potential function in peripheral nerve repair and regeneration. The related TRPML1 and TRPML2 were not differently regulated after nerve injury. The generated *Trpml3*$^{\Delta/\Delta}$ mouse model could be used as a model to investigate the involvement of TRPML3 in neuropathic pain.

In conclusion, my results showed that in native cells, TRPML3 channels might be limited or might not be present in the plasma membrane. If this is the case, the varitint-waddler phenotype would have been caused by mislocalization of the constitutively active TRPML3(A419P) isoform to the plasma membrane. Second, in native cells, TRPML3 channels might not exist as homomeric channels. I propose that they form heteromeric channels either with other members of the TRPML subfamily, or with structurally related channels. Based on interaction studies, TRPML3 is able to heteromerize with other TRPML channels as well as with TRPV5 and TRPV6, which could account for the observed nonresponsiveness towards TRPML3 activating compounds in melanocytes and sensory hair cells and for compensation of *Trpml3* inactivation.

5. Summary

TRPML3 belongs to the mucolipin subfamily of the transient receptor potential (TRP) channels. The mouse *Trpml3* gene was identified in a positional cloning project to identify the gene responsible for the varitint-waddler (*Va*) mouse phenotype, which displays severe auditory, vestibular and pigmentation defects. A single A419P amino acid substitution within the predicted 5th transmembrane domain of TRPML3 was identified to cause this *Va* phenotype. The A419P mutation renders TRPML3 constitutively active, resulting in highly elevated $[Ca^{2+}]_i$ and apoptotic cell death in cells that natively express TRPML3, such as melanocytes and sensory hair cells.

However, it is remarkable that sensory hair cells of *Va* mice survive for several postnatal weeks. Presented here are *in vitro* and *in vivo* data supporting the hypothesis that the survival of *Va* hair cells is linked to their ability to deal with Ca^{2+} loads due to the abundance of plasma membrane calcium ATPases (PMCAs). The rescue effect of PMCA2 is due to the decrease in $[Ca^{2+}]_i$. Ca^{2+}-buffering and Ca^{2+} extrusion abilities of hair cells are powerful enough to prevent cell death for weeks, even in the presence of constitutively active TRPML3(A419P), which is able to induce rapid apoptosis in other cells.

To gain more insight into the function of the wild-type TRPML3 channel, a high-throughput small molecule activator screen was conducted. In this screen 53 compounds were identified that selectively activate TRPML3. Cheminformatics analyses of compounds revealed 9 different chemical scaffolds and 20 singletons. However, testing compounds on sensory hair cells revealed the absence of activator-responsive channels. Melanocytes showed weak or no responses to the compounds, except for SN-2, which when used at a relatively high concentration was able to elicit a significant increase of the intracellular Ca^{2+} concentration. The lack of substantial responses to identified activators suggested that TRPML3 in native cells is either present only in limited numbers in the plasma membrane or that the protein heteromerizes with other proteins, leading to channels that are not or only weakly responsive to the compounds.

To elucidate the physiological role of murine TRPML3, a conditional knockout of *Trpml3* was generated. Despite the strong *Va* phenotype, no overt inner ear phenotype was detectable in mice with ubiquitous *Trpml3* inactivation or when the gene was inactivated from P0-P3 onwards. Both mouse models revealed that TRPML3 as a homomer is not essential for detectable inner ear function and developmet *in vivo*. Although these results do not necessarily exclude TRPML3 from playing a role in mechanotransduction, they do

reveal that if the transduction channel complex utilizes TRPML3, TRPML3 may function as a dispensable subunit.

6. Zusammenfassung

TRPML3 gehört zu der Mukolipin Subfamilie der TRP (*transient receptor potential*) Kanäle. Das *Trpml3* Gen wurde in einem positionalen Klonierungsprojekt identifiziert, um das verantwortliche Gen für den *varitint-waddler* (*Va*) Phänotyp mit schwerwiegenden auditorischen, vestibulären und Pigmentierungsdefekten zu bestimmen. Ein Aminosäureaustausch (A419P) innerhalb des 5. Transmembransegments von TRPML3 ist verantwortlich für den *Va* Phänotyp. Der A419P Austausch macht TRPML3 konstitutiv aktiv, was zu erhöhtem $[Ca^{2+}]_i$ und zu programmierten Zelltod in Zellen mit nativem TRPML3, wie z.B. Melanozyten und sensorische Haarzellen, führt.

Bemerkenswert ist, dass sensorische Haarzellen von *Va* Mäusen für mehrere postnatale Wochen überleben. In der vorliegenden Arbeit wurde *in vivo* und *in vitro* untersucht, inwiefern das Überleben der *Va*-Haarzellen und deren Fähigkeit mit der Ca^{2+}-Belastung umzugehen, gekoppelt ist an die gleichzeitige Präsenz von Plasmamembranständigen Ca^{2+}-ATPasen (PMCAs). Es wurde gezeigt, dass die Fähigkeit der sensorischen Haarzellen Ca^{2+} zu puffern und zu extrudieren ist ausreichend, um den Zelltod für mehrere Wochen hinauszuzögern, auch in Anwesenheit der konstitutiv aktiven TRPML3(A419P)-Variante, welche in anderen Zelltypen fähig ist einen schnellen Zelltod zu induzieren. Der Rettungeffekt ist die Folge der Reduzierung des $[Ca^{2+}]_i$.

Um einen Einblick in die Funktion von Wildtyp-TRPML3 zu erlangen, wurde in einem Hochdurchsatzverfahren nach chemischen Aktivatoren gesucht. Es wurden 53 Verbindungen identifiziert, die TRPML3 selektiv aktivieren. Ein Test dieser Verbindungen auf TRPML3 exprimierende Kochleapräparate zeigte jedoch, dass auditorische Haarzellen nicht auf diese Aktivatoren reagieren. Hautmelanozyten zeigten nur schwache oder ebenfalls keine Antworten auf die Aktivatoren, mit Ausnahme der Substanz SN-2, welche einen signifikanten Anstieg der intrazellulären Ca^{2+}-Konzentration hervorrief. Das Fehlen einer verbesserten Antwort auf die TRPML3 Aktivatoren kann dadurch erklärt werden, dass TRPML3 in nativen Zellen in der Plasmamembran nur in limitierender Menge vorkommt oder dass TRPML3 mit anderen Proteinen heteromerisiert, was zu multimeren Kanalkomplexen führt, die nicht oder nur schwach auf die Verbindungen reagieren.

Um die physiologische Rolle des TRPML3's im inneren Ohr aufzuklären, wurde eine konditionaler *Trpml3* Inaktivierung generiert. Trotz des schwerwiegenden *Va* Phänotyps konnte kein Innenohrphänotyp in Mäusen mit ubiquitärer *Trpml3* Inaktivierung oder wenn das Gen ab P0-P3 inaktiviert wurde, gezeigt werden. Beide Mausmodelle zeigten, dass

TRPML3 als Homomer nicht essenziell für den Hörprozess ist. Die Ergebnisse schliessen TRPML3 nicht unbedingt von einer Rolle im Prozess der auditorischen Mechanotransduktion aus. Sie verraten jedoch, falls TRPML3 zum Mechanotransduktionskomplex gehört, dass das TRPML3-Protein als eine ersetzbare Untereinheit fungieren könnte.

7. References

Asai, Y., Holt, J.R., and Géléoc, G.S.G. (2009). A quantitative analysis of the spatiotemporal pattern of the transient receptor potential gene expression in the developing mouse cochlea. *JARO* **11**, 27-37.

Atiba-Davies, M., and Noben-Trauth, K. (2007). TRPML3 and hearing loss in the varitint-waddler mouse. *Biochem Biophys Acta* **1772**, 1028-1031.

Bach, G. (2001) Minireview Mucolipidosis Type IV. *Mol Genet Metab* **73**, 197-203.

Bargal, R., Avidan, N., Ben-Asher, E., Olender, Z., Zeigler, M., Frumkin, A., Raas-Rothschild, A., Glusman, G., Lancet, D., and Bach, G. (2000). Identification of the gene causing mucolipidosis type IV. *Nat Genet* **26**, 118-123

Basic-Kes, V., Zavoreo, I., Bosnar-Puretic, M., Ivankovic., M., Bitujac, M., Govori, V., and Demarin, V. (2009). Neuropathic pain. *Acta Clin Croat.* **48** (3), 359-365.

Bautista, D.M., Jordt, S.-E., Nikai, T., Tsuruda, P.R., Read, A.J., Poblete, J., Yamoah, E.N., Basbaum, A.I., and Julius, D. (2006). TRPA1 mediates the inflammatory action of environmental irritants and proalgesic agents. *Cell* **124**, 1269-1282.

Ben-Arie, N., Bellen, H.J., Armstrong, D.L., McCall, A.E., Gordadze, P.R., Guo, Q., Matzuk, M.M., and Zoghbi, H.Y. (1997). Math1 is essential for genesis of cerebellar granule neurons. *Nature* **390**, 169-172.

Bermingham, N.A., Hassan, B.A., Price, S.D., Vollrath, M.A., Ben-Arie, N., Eatock, R.A., Bellen, H.J., Lysakowski, A., and Zoghbi, H.Y. (1999). Math1: an essential gene for the generation of inner ear hair cells. *Science* **284**, 1837-1841.

Beurg M., Fettiplace R., Nam J.H., Ricci A.J. (2009). Localization of inner hair cell mechanotransducer channels using high-speed calcium imaging. *Nat Neurosci* **12**, 553-558.

Boekhoff-Falk, G. (2005). Hearing in Drosophila: development of Johnston's organ and emerging parallels in vertebrate ear development. *Dev Dyn* **232**, 550-558.

Bouhassira, D., Lantéri-Minet, M., Attal, N., Laurent, B., and Touboul, C. (2008). Prevalence of chronic pain with neuropathic characteristics in the general population. *J Pain* **136** (3), 380-387.

Brendan, J., McCullough, B.J., and Tempel, B.L. (2004). Haplo-insufficiency revealed in deafwaddler mice when tested for hearing loss and ataxia. *Hear Res* **195**, 90-102.

Brooks, J. and Tracey, I. (2005). From nociception to pain perception: imaging the spinal and supraspinal pathways. *J Pain* **7**, 281-289.

Cable, J. and Steel, K.P. (1998). Combined cochleo-saccular and neuroepithelial abnormalities in the Varitint-waddler-J (Va^J) mouse. *Hear Res* **123**, 125-136.

Chen, X., Shen, D., Samie, M., and Xu, H. (2010). Mucolipins: Intracellular TRPML1-3 channels. *FEBS Letters* **584**(10), 2013-2021.

Chow, L.M.L., Tian, Y., Weber, T., Corbett, M., Zuo, J., and Baker, S.J. (2006). Inducible Cre recombinase activity in mouse cerebellar granule cell precursors and inner ear hair cells. *Dev Dyn* **235**, 2991-2998.

Clapham, D.E. (2007). SnapShot: Mammalian TRP channels. *Cell* **129**, 220-220.e1.

Corey, D.P., Garcia-Anoveros, J., Holt, J.R., Kwan, K.Y., Lin, S.Y., Vollrath, M.A., Amalfitano, A., Cheung, E.L., Derfler, B.H., Duggan, A., Geleoc, G.S., Gray, P.A., Hoffman, M.P., Rehm, H.L., Tamasauskas, D., and Zhang, D.S. (2004). TRPA1 is a candidate for the mechanosensitive transduction channel of vertebrate hair cells. *Nature* **432**, 723-730.

Corey, D.P. (2006). What is the hair cell transduction channel? *J Physiol* **576**, 23-28.

Cuajungco, M.P., Grimm, C., and Heller, S. (2007). TRP channels as candidates for hearing and balance abnormalities in vertebrates. *Biochem Biophys Acta* **1772**, 1022-1027.

Curcio-Morelli, C., Zhang, P., Venugopal, B., Charles, F.A., Browning, M.F., Cantiello, H.F., and Slaugenhaupt, S.A. (2009). Functional multimerization of mucolipin channel proteins. *J Cell Physiol* **222**, 328-335.

Danielian, P.S., White, R., Hoare, S.A., Fawell, S.E., and Parker, M.G. (1993). Identification of residues in the estrogen receptor that confer differential sensivity to estrogen and hydroxytamoxifen. *Mol Endocrinol* **7**, 232-240.

Desai, B.N. and Clapham, D.E. (2005). TRP channels and mice deficient in TRP channels. *Eur J Physiol* **451**, 11-18.

Di Palma, F., Belyantseva, I.A., Kim, H.J., Vogt, T.F., Kachar, B., and Noben-Trauth, K. (2002). Mutations in Mcoln3 associated with deafness and pigmentation defects in varitint-waddler (Va) mice. *Proc Natl Acad Sci U S A* ***99***, 14994-14999.

Dumont, R.A., Lins, U., Filoteo, A.G., Penniston, J.T., Kachar, B., and Gillespie, P.G. (2001). Plasma Membrane Ca^{2+}-ATPase isoform 2a is the PMCA of hair bundles. *J Neurosci* **21**, 5066-5078.

Duncan, R.K. and Saunders, J.C. (2000). Stereocilium injury mediates hair bundle stiffness loss and recovery following intense water-jet stimulation. *J Comp Physiol* **186**, 1095-1106.

Dymecki, S.M. (2000). Site-specific recombination in cells and mice. In: Joyner A.L., Gene Targeting a practical approach. *OXFORD* **2nd ed**: pp 37-99.

Eberl, D.F. and Boekhoff-Falk, G. (2007). Development of Johnston's organ in Drosophila. *Int J Dev Biol* **51**, 679-687.

Edge, R.M., Evans, B.N., Pearce, M., Richter, C.-P., Hu, X., and Dallos, P. (1998). Morphology of the unfixed cochlea. *Hear Res* **124**, 1-16.

Edmonds, B., Reyes, R., Schwaller, B., and Roberts, W.A. (2000). Calretinin modifies presynaptic calcium signaling in frog saccular hair cells. *Nat Neurosci* **8**, 786-790.

Erler, I., Hirnet, D., Wissenbach, U., Flockerzi, V., & Niemeyer, B.A. (2004). Ca^{2+}-selective transient receptor potential V channel architecture and function require a specific ankyrin repeat. *J Biol Chem* **279**, 34456–63.

Fettiplace, R. and Hackney, C.M. (2006). The sensory and motor roles of auditory hair cells. *Nature Reviews Neurosci* **7**, 19-29.

Forge, A. and Wright, T. (2002). The molecular architecture of the inner ear. *British Medical Bulletin* **63**, 5-24.

Fridberger, A., Flock, A., Ulfendahl, M., and Flock, B. (1998). Acoustic overstimulation increases outer hair cell Ca^{2+} concentration and causes dynamic contractions of the hearing organ. *Proc Natl Acad Sci U S A* **95**, 7127-7132.

Gao, X., Wu, L., and O'Neil, R.G. (2003). Temperature-modulated diversity of TRPV4 channel gating: activation by physical stresses and phorbol ester derivatives through protein kinase C-dependent and - independent pathways. *J Biol Chem* **278**, 27129-27137.

Geleoc, G.S., and Holt, J.R. (2003). Developmental acquisition of sensory transduction in hair cells of the mouse inner ear. *Nat Neurosci* **6**, 1019-1020.

Gillespie, P.G. and Müller, U. (2009). Mechanotransduction by hair cells: models, molecules, and mechanisms. *Cell* **139**, 33-44.

Gong, Z., Son, W., Chung, Y.D., Kim, J., Shin, D.W., McClung, C.A., Lee, Y., Lee, H.W., Chang, D.-J., Kaang, B.-K., Cho, H., Oh, U., Hirsh, J., Kernan, M.J., and Kim C. (2004). Two independent TRPV channel subunits, Inactive and Nanchung, mediate hearing in Drosophila. *J Neurosci* **24**, 9059-9066.

Göpfert, M.C. and Robert, D. (2002). The mechanical basis of Drosophila audition. *JEB* **205**, 1199-1208.

Grimm, C., Cuajungco, M.P., van Aken, A.F., Schnee, M., Jörs, S., Kros, C.J., Ricci, A.J., and Heller, S. (2007). A helix-breaking mutation in TRPML3 leads to constitutive activity underlying deafness in the varitint-waddler mouse. *Proc Natl Acad Sci U S A* **104**, 19583-19588.

Grimm, C., Jörs, S., and Heller, S. (2009). Life and death of sensory hair cells expressing constitutively active TRPML3. *J Biol Chem* **284**, 13823-13831.

Grimm, C., Jörs, S., Saldanha, S.A., Obukhov, A.G., Pan, B., Oshima, K., Cuajungco, M.P., Chase, P., Hodder, P., and Heller, S. (2010). Small molecule activators of TRPML3. *Chemistry & Biology* **17**, 135-148.

Grynkiewicz, G, Poenie, M., and Tsien, R.Y. (1985). A new generation of Ca^{2+} indicators with greatly improved fluorescence properties. *J Biol Chem* **260**, 3440-3450.

Güler, A.D, Lee, H., Iida, T., Shimizu, I., Tominaga, M., and Caterina, M. (2002). Heat-evoked activation of the ion channel, TRPV4. *J Neurosci* **22**, 6408-6414.

Hanaoka, K., Qian, F., Boletta, A., Bhunia, A.K., Piontek, K., Tsiokas, L., Sukhatme, V.P., Guggino, W.B., and Germino, G.G. (2000). Co-assembly of polycystin-1 and -2 produces unique cation-permeable currents. *Nature* **408**, 990-994.

Hébert, J.M and McConnell, S.K. (2000). Targeting of cre to the Foxg1 (BF-1) locus mediates loxP recombination in the telencephalon and other developing head structures. *Dev Bio* **222**, 296-306.

Heller, S., Bell, A.M., Denis, C.S., Choe, Y., and Hudspeth, A.J. (2002). Parvalbumin 3 is an abundant Ca^{2+} buffer in hair cells. *J Assoc Res Otolaryngol* **03**, 488-498.

Hellwig, N., Albrecht, N., Harteneck, C., Schultz, G., and Schaefer, M. (2005). Homo- and heteromeric assembly of TRPV channel subunits. *J Cell Sci* **118**, 917-928.

Hilding, D.A. and Ginzberg, R.D. (1977). Pigmentation of the stria vascularis. The contribution of neural crest melanocytes. *Acta Otolaryngol* **84**, 24-37.

Hodder, P., Cassaday, J., Peltier, R., Berry, K., Inglese, J., Feuston, B., Culberson, C., Bleicher, L., Cosford, N.D.P., Bayly, C., Suto, C., Varney, M., and Strulovici, B. (2003). Identification of metabotropic glutamate receptor antagonists using an automated high-throughput screening system. *Anal Biochem* **313**, 246-254.

Hofmann, T., Schaefer, M., Schultz, G., and Gudermann, T. (2002). Subunit composition of mammalian transient receptor potential channels in living cells. *Proc Natl Acad Sci U S A* **99**, 7461-7466.

Hudspeth, A.J. (2002). How the ear's works work: mechanoelectrical transduction and amplification by hair cells. *Cell* **108**, 371-381.

Liberman M.C. and Gao W.Y. (1995). Chronic chochlear de-efferentation and susceptibility to permanent acoustic injury. *Hear Res* **90**, 158-168.

Jero, J., Coling, D.E., Lalwani, A.K. (2001). The use of Preyer's reflex in evaluation of hearing in mice. *Acta Oto Laryngologica* **121**, 585-589.

Ji, R.R. and Strichartz, G. (2004). Cell signaling and the genesis of neuropathic pain. *Sci STKE* **252**, E14.

Jones, B.J. and Roberts, D.J. (1968). The quantitative measurement of motor inco-ordination in native mice using an accelerating rotarod. *J Pharm Pharmac* **20**, 302-304.

Jörs S., Grimm C., Becker L., and Heller S. (2010). Genetic inactivation of *Trpml3* does not lead to hearing and vestibular impairment in mice. *PLoS ONE* **5**(12), e14317.

Kim, H.J., Jackson, T., and Noben-Trauth, K. (2002). Genetic analyses of mouse deafness mutation Varitint-waddler (Va) and Jerker ($Espn^{je}$). *J Assoc Res Otolaryngol* **4**, 83-90.

Kim, H.J., Li, Q., Tjon-Kon-Sang, S., So, I., Kiselyov, K., and Muallem, S. (2007). Gain-of-function mutation in TRPML3 causes the mouse Varitint-Waddler phenotype. *J Biol Chem* **282**, 36138-36142.

Kim, H.J., Li, Q., Tjon-Kon-Sang, S., So, I., Kiselyov, K., Soyombo, A.A., and Muallem, S. (2008). A novel mode of TRPML3 regulation by extracytosolic pH absent in the varitint-waddler phenotype. *EMBO J* **27**, 1197-1205.

Kim, H.J., Soyombo, A.A., Tjon-Kon-Sang, S., So, I., and Muallem, S. (2009). The Ca^{2+} channel TRPML3 regulates membrane trafficking and autophagy. *Traffic* **10**, 1157-1167.

Kim, J., Chung, Y.D., Park, D.-Y., Choi, S., Shin, D.W., Soh, H.S., Lee, H.W., Son, W., Yim, J., Park, C.-S., Kernan, M.J., and Kim, C. (2003). A TRPV family ion channel required for hearing in Drosophila. *Nature* **424**, 81-84.

Kozlov, A.S., Risler, T., and Hudspeth, A.J. (2007). Coherent motion of stereocilia assures the concerted gating of heir-cell transduction channels. *Nat Neurosci* **10**, 87-92.

Kwan, K.Y., Allchorne, A.J., Vollrath M.A., Christensen, A.P., Zhang, D.-S., Woolf, C.J., and Corey, D.P. (2006). TRPA1 contributes to cold, mechanical and chemical nociception but is not essential for hair-cell transduction. *Neuron* **50**, 277-289.

Lamberts, M.S. (2007). Breeding strategies for maintaining colonies of laboratory mice. *Jackson Laboratory Resource Manual*.

Lang, F., Vallon, V., Knipper, M., and Wangemann, P. (2007). Functional significance of channels and transporters expressed in the inner ear and kidney. *Am J Physiol Cell Physiol* **293**, C1187-1208.

Langerak, P., Nygren, A.O.H., Schouten, J.P., and Jacobs, H. (2005). Rapid and quantitative detection of homologous and non-homologous recombination events using three oligonucleotide MLPA. *Nucleic Acids Res* **33**(22), e188.

Li, A., Xue, J., and Peterson, E.H. (2008). Architecture of the mouse utricle: macular organization and hair bundle heights. *J Neurophysiol* **99**, 718-733.

Li, H.S. and Borg, E. (1991). Age-related loss of auditory sensitivity in two mouse genotypes. *Acta Otolaryngol* **111** (5), 827-834.

Li, M., Tian, Y., Fritzsch, B., Gao, J., Wu, X., and Zuo, J. (2004). Inner hair cell Cre-expressing transgenic mouse. *Genetics* **39**, 173-177.

Liedtke, W., Choe, Y., Martí-Renom, M.A., Bell, A.M., Denis, C.S., Šali, A., Hudspeth, A.J., Friedman, J.M., and Heller, S. (2000). Vanilloid receptor-related osmotically activated channel (VR-OAC), a candidate vertebrate osmoreceptor. *Cell* **103**, 525-535.

Liedtke, W., Tobin, D.M., Bargmann, C.I., and Friedman, J.M. (2003). Mammalian TRPV4 (VR-OAC) directs behavioral responses to osmotic and mechanical stimuli in caenorhabditis elegans. *Proc Natl Acad Sci U S A* **100**, 14531-14536.

Lumpkin, E.A. and Hudspeth, A.J. (1998). Regulation of free Ca^{2+} concentration in hair cell stereocilia. *J Neurosci* **18**, 6300-6318.

Meers, P. and Mealy, T. (1993). Calcium-dependent Annexin V binding to phospholipids: Stoichiometry, specifity, and the role of negative charge. *Biochemistry* **32**, 11711-11721.

Micsenyi, M.C., Dobrenis, K., Stephney, G., Pickel, J., Vanier, M.T., Slaugenhaupt, S.A, and Walkley, S.U. (2009). Neuropathology of the $Mcoln1^{-/-}$ knockout mouse model of mucolipidosis type IV. *J Neuropathol Exp Neurol* **68**, 125-135.

Miedel, M.T., Rbaibi, Y., Guerriero, C.J., Colletti, G., Weixel, K.M., Weisz, O.A., and Kiselyov, K. (2008). Membrane traffic and turnover in TRP-ML1-deficient cells: a revised model for mucolipidosis type IV pathogenesis. *J Exp Med* **205**, 1477-1490.

Mohler, P. J., Gramolini, A. O., and Bennett, V. (2002). Ankyrins. *J. Cell Sci.*, **115**, 1565-1566.

Moller, A. (2007) Neural generators for auditory brainstem evoked potential. In: Burkard, R., Don, M., and Eggermont, J.J. Auditory evoked potentials. Basic principles and clinical application. Philadelphia: Lippincott Williams & Wilkins. 336-354.

Moqrich, A., Wook Hwang, S., Earley, T.J., Petrus, M.J., Murray, A.N., Spencer, K.S.R., Andahazy, M., Story, G.M., and Patapoutian, A. (2005). Impaired thermosensation in mice lacking TRPV3, a heat and camphor sensor in the skin. *Science* **307**, 1468-1472.

Moser, T., Brandt, A., and Lysakowski, A. (2006). Hair cell ribbon synapses. *Cell Tissue res* **326**, 347-359.

Nagata, K., Zheng, L., Madathany, T., Castiglioni, A.J., Bartles, J.R., and Garcia-Anoveros, J. (2008). The varitint-waddler (Va) deafness mutation in TRPML3 generates constitutive, inward rectifying currents and causes cell degeneration. *Proc Natl Acad Sci U S A* **105**, 353-358.

Nilius, B., Owsianik, G., Voets, T., and Peters J. A. (2007). Transient receptor potential cation channels in disease. *Physiol Rev* **87**, 165-217.

Oancea, E., Vriens, J., Brauchi, S., Jun, J., Splawski, I., and Clapham, D.E. (2009). TRPM1 forms ion channels associated with melanin content in melanocytes. *Sci Signal.* **2**, ra21.

Owsianik, G., D'hoedt, D., Voets, T., and Nilius, B. (2006). Structure-function relationship of the TRP channel superfamily. *Rev Physiol Biochem Pharmacol* **156**, 61-90.

Papaioannou, V. and Johnson, R. (2000). Production of chimeras by blastocyst and morula injection of targeted ES cells. In: Joyner A.L., Gene Targeting a practical approach. *OXFORD* **2nd ed**: pp 133-175.

Patapoutian, A., Tate, S., and Woolf, C.J. (2009). Transient receptor potential channels: targeting pain at the source. *Nat Rev Drug Discov* **8**, 55-68.

Pedersen, S.F., Owsianik, G., and Nilius, B. (2005). TRP channels: an overview. *Cell Calcium* **38**, 233-252.

Penheiter, A.R., Filoteo, A.G., Croy, C.L., and Penniston, J.T. (2001). Characterization of the deafwaddler mutant of the rat plasma membrane calcium-ATPase 2. *Hear Res* **162**, 19-28.

Puertollano, R. and Kiselyov, K. (2009). TRPMLs: in sickness and in health. *Am J Physiol Renal Physiol* **296**, 1245-1254.

Ramsey I.S., Delling M., and Clapham D.E. (2006). An introduction to TRP channels. *Annu Rev Physiol* **68**, 619-647.

Raphael, Y. (2002). Cochlear pathology, sensory cell death and regeneration. *British Medical Bulletin* **63**, 25-38.

Raphael, Y. and Altschuler, R.A. (1991). Reorganization of cytoskeletal and junctional proteins during cochlear hair cell degeneration. *Cell Motil Cytoskel* **18**, 215-227.

Rohacs, T., Lopes, C.M., Michailidis, I., and Logothetis, D.E. (2005). PI(4,5)P2 regulates the activation and desensitization of TRPM8 channels through the TRP domain. *Nat Neurosci* **8**, 626-634.

Sauer, B. and Henderson, N. (1988). Site-specific DNA recombination in mammalian cells by the Cre recombinase of bacteriophage P1. *Proc Natl Acad Sci U S A* **85**, 5166-5170

Scacheri, P.C., Crabtree, J.S., Novotny, E.A., Garrett-Beal, L., Chen, A., Edgemon, K.A., Marx, S.J., Spiegel, A.M., Chandrasekharappa, S.C., and Collins F. S. (2001). Bidirectional transcriptional activity of PGK-neomycin and unexpected embryonic lethality in heterozygote chimeric knockout mice. *Genesis* **30**, 259-263

Scadding, J. (2003). Neuropathic pain. *ACNR* **3**, 8-14.

Schaefer, M. (2005). Homo- and heteromeric assembly of TRP channel subunits. *Pflugers Arch – Eur J Physiol* **451**, 35-42.

Shen, J., Harada, N., Kubo, N., Liu, B., Mizuno, A., Suzuki, M., and Yamashita, T. (2006). Functional expression of transient receptor potential vanilloid 4 in the mouse cochlea. *Neuroreport* **17** (2), 135-139.

Shin, J.B., Adams, D., Paukert, M., Siba, M., Sidi, S., Levin, M., Gillespie, P.G., and Gründer, S. (2005). Xenopus TRPN1 (NOMPC) localizes to microtubule-based cilia in epithelial cells, including inner-ear hair cells. *Proc Natl Acad Sci U S A* **102**, 12572-12577.

Sidi, S., Friedrich, R.W., and Nicolson, T. (2003). NompC TRP channel required for vertebrate sensory hair cell mechanotransduction. *SCIENCE* **301**, 96-99.

Silver, L.M. (1995). Mouse genetics: concepts and applications. *Oxford University Press*, www.informatics.jax.org/silver/.

Staaf, S., Oerther, S., Lucas, G., Mattsson, J.P., and Ernfors, P. (2009). Differential regulation of TRP channel in a rat model of neuropathic pain. *J Pain* **114**, 187-199.
Stanley, A.G. (2009). Essential of Audiology – Auditory evoked potentials. *Thieme* **3rd Edition**, 333-345.

Steel K.P. and Barkway, C. (1989). Another role for melanocytes: their importance for normal stria vascularis development in the mammalian inner ear. *Development* **107**, 453-463.

Street, V.A, McKee-Johnson, J.W., Fonseca, R.C., Tempel, B.L., and Noben-Trauth, K. (1998). Mutations in a plasma membrane Ca^{2+}-ATPase gene cause deafness in deafwaddler mice. *Nat Genet* **19**, 390-394.

Strotmann, R., Harteneck, C., Nunnenmacher, K., Schultz, G., and Plant, T. D., (2000). OTRPC4, a non-selective cation channel that confers sensitivity to extracellular osmolarity. *Nat Cell Biol* **2**, 695-702.

Sun, M., Goldin, E., Stahl, S., Falardeau, J.L., Kennedy, J.C., Acierno, J.S. Jr, Bove, C., Kaneski, C.R., Nagle, J., Bromley, M.C., Colman, M., Schiffmann, R., and Slaugenhaupt, S.A. (2000). Mucolipidosis type IV is caused by mutations in a gene encoding a novel transient receptor potential channel. *Hum Mol Genet* **9**, 2471-2478.

Sutters, M. and Germino, G.G. (2003). Autosomal dominant polycystic kidney disease: molecular genetics and pathophysiology. *J Lab Clin Med* **141**, 91-101.

Tabuchi, K., Suzuki, M., Mizuno, A., and Hara A. (2005). Hearing impairment in TRPV4 knockout mice. *Neuroscience letters* **382**, 304-308.

Tait, J.F. and Gibson, D. (1992). Phospholipid binding of Annexin V: Effects of calcium and membrane phosphatidylserine content. *Arch Biochem Biophys* **298**, 187-191.

Takahashi, A., Camacho, P., Lechleiter, J.D., and Herman, B. (1999). Measurement of intracellular calcium. *Physiological reviews* **79**, 1089-1125.

Tang, S.H.E., Silva, F.J., Tsark, W.M.K., Mann, J.R. (2002). A Cre/loxP-deleter transgenic line in mouse strain 129S1/SvlmJ. *Genesis* **32**: 199-202.

Tascioglu, A.B. (2005).Brief review of vestibular system anatomy and its higher order projections. *Neuroanatomy* **4**: 24-27.

Tian, Y., Li, M., Fritzsch, B., and Zuo, J., (2004). Creation of a transgenic mouse for hair-cell gene targeting by using a modified bacterial artificial chromosome containing prestin. *Dev Dyn* **231**, 199-203.

Torrance, N., Smith, B.H., Bennett, M.I., and Lee, A.J. (2006). The epidemiology of chronic pain of predominantly neuropathic origin. Results from a general population survey. *J Pain* **7** (4), 281-289.

Treusch, S., Knuth, S., Slaugenhaupt, S.A., Goldin, E., Grant, B.D., and Fares, H. (2004). Caenorhabditis elegans functional orthologue of human protein h-mucolipin-1 is required for lysosome biogenesis. *Proc Natl Acad Sci U S A* **101**, 4483-4488.

Utomo, A.R., Nikitin, A.Y., and Lee, W.H. (1999). Temporal, spatial, and cell-type-specific control of Cre-mediated DNA recombination in transgenic mice. *Nat Biotechnol* **17**, 1091-1096.

van Aken, A.F., Atiba-Davies, M., Marcotti, W., Goodyear, R.J., Bryant, J.E., Richardson, G.P., Noben-Trauth, K., and Kros, C.J. (2008). TRPML3 mutations cause impaired mechano-electrical transduction and depolarization by an inward-rectifier cation current in auditory hair cells of varitint-waddler mice. *J Physiol* **586**, 5403-5418.

Venkatachalam, K., Hofmann, T., and Montell, C. (2006). Lysosomal localization of TRPML3 depends on TRPML2 and the mucolipidosis-associated protein TRPML1. *J Biol Chem* **281**, 17517-17527.

Venkatachalam, K. and Montell, C. (2007). TRP channels. *Annu. Rev. Biochem.* **76**, 387-417.

Vennekens, R., Hoenderop, J.G.J., Prenen, M.S., Willems, P.H.G.M., Droogmans, G., Nilius, B., and Bindels, R.J.M. (2000). Permeation and gating properties of the novel epithelial Ca^{2+} channel. *J Biol Chem* **275**, 3963-3969.

Vergarajauregui, S. and Puertollano, R. (2006). Two di-leucine motifs regulate trafficking of mucolipin-1 to lysosomes. *Traffic* **7**, 337-353.

Voets, T., Talavera, K., Owsianik, G., and Nilius, B. (2005). Sensing with TRP channels. *Nature chemical biology* **1**, 1-8.

Walker, R.G., Willingham, A.T., Zuker, C.S. (2000). A Drosophila mechanosensory transduction channel. *SCIENCE* **287**, 2229-2234.

Wangemann, P. (2002). K^+ cycling and the endocochlear potential. *Hear Res*. **165**, 1-9.

Watanabe, H., Vriens, J., Suh, S.H., Benham, C.D., Droogmans, G., and Nilius, B. (2002). Heat-evoked activation of TRPV4 channels in a HEK293 cell expression system and in native mouse aorta endothelial cells. *J Biol Chem* **277**, 47044-47051.

Watanabe, H., Vrience, J., Prenen, J., Droogmans, G., Voets, T., and Nilius, B. (2003). Anandamide and arachidonic acid use epoxyeicosatrienoic acids to activate TRPV4 channels. *Nature* **424**, 434-438.

Wu, L.-J., Sweet, T.-B., and Clapham, D.E. (2010). International union of basic and clinical pharmacology. LXXVI. Current progress in the mammalian TRP ion channel family. *Pharmacol Rev* **62**, 381-404.

Xu, H., Delling, M., Li, L., Dong, X., and Clapham, D.E. (2007). Activating mutation in a mucolipin transient receptor potential channel leads to melanocyte loss in varitint-waddler mice. *Proc Natl Acad Sci U S A* **104**, 18321-18326.

Yamasaki, M., Komune, S., Shimozono, M., Matsuda, K., and Haruta, A. (2000). Development of monovalent ions in the endolymph in mouse cochlea. *ORL J Otorhinolaryngol Relat Spec* **62**, 241-246.

Yamoah, E.N., Lumpkin, E.A., Dumont, R.A., Smith, P.J.S., Hudspeth, A.J., and Gillespie, P.G. (1998). Plasma membrane Ca^{2+}-ATPase extrudes Ca^{2+} from hair cell stereocilia. *J Neurosci* **18**, 610-624.

Zanazzi, G. and Matthews, G. (2009). The Molecular Architecture of Ribbon Presynaptic Terminals. *Mol Neurobiol* **39**, 130-148.

Zelarayan, L.C., Vendrell, V., Alvarez, Y., Domínguez-Frutos, E., Theil, T., Alonso, M.T., Maconochie, M., and Schimmang, T. (2007). Diffenrential requirements for FGF3, FGF8 and FGF10 during inner ear development. *Dev Bio* **308**, 379-391.

Zheng, Q.Y., Johnson, K.R., and Erway, L.C. (1999). Assessment of hearing in 80 inbred strains of mice by ABR threshold analyses. *Hear Res* **130**, 94-107.

Zhou, X., Jen, P.H.-S., Seburn, K.L., Frankel, W.N., and Zheng, Q.Y. (2006). Auditory brainstem responses in 10 inbred strains of mice. *Brain Res* **1091**, 16-26.

8. Publications

Monk, K.R., Oshima, K., **Jörs, S.**, Heller, S., and Talbot, W.S. (2011) Gpr126 is essential for peripheral nerve development and myelination in mammals. *Development* 138, 2673-2680.

Jörs, S.*, Grimm, C.*, Becker, L., and Heller, S. (2010). Genetic inactivation of *Trpml3* does not lead to hearing and vestibular impairment in mice. *PLoS ONE* 5(12), e14317.

Grimm, C.*, **Jörs, S.***, Saldanha, S.A.*, Obukhov, A.G., Pan, B., Oshima, K., Cuajungco, M.P., Chase, P., Hodder, P.S., and Heller, S. (2010). Small molecule activators of TRPML3. *Chemistry & Biology* 17, 135-148.

Grimm, C.*, **Jörs, S.***, and Heller, S. (2009) Life and death of sensory hair cells expressing constitutively active TRPML3. *J Biol Chem* 284, 13823-31.

Grimm, C., Cuajungco, M.P., van Aken, A.F.J., Schnee, M., **Jörs, S.**, Kros, C.J., Ricci, A.J., and Heller, S. (2007). A helix-breaking mutation in TRPML3 leads to constitutive activity underlying deafness in the varitint-waddler mouse. *Proc Natl Acad Sci U S A* 104, 19583-19588.

Jörs, S., Kazanski, V., Foik, A., Krautwurst, D., and Harteneck, C. (2006). Receptor-induced activation of Drosophila TRPγ by polyunsaturated fatty acids. *J Biol Chem* 281(40), 29693-702.

*Contributed equally

Conferences

2007 37th annual meeting of Society for Neuroscience (SfN), San Diego, USA:

Grimm, C., Korne, C.J., Cuajungco, M.P., Schnee, M., Atiba-Davies, M., **Jörs, S.**, van Aken, A.F.J., Marcotti, W., Goodyear, R., Bryant, J.E., Richardson, G., Ricci, A., Noben-Trauth, K., and Heller, S., Impaired hair cell mechanotransduction and a constitutively active cation channel resulting from a TRPML3 helix-breaking mutation in varitint-waddler mice.

2009 7th Molecular Biology of Hearing and Deafness Conference, Boston, USA

Jörs, S., Grimm, C., and Heller, S., The activity of wild-type TRPML3 is inhibited by high extracellular sodium: endolymph-like solution (ELS) activates TRPML3.

Grimm, C., **Jörs, S.**, Saldanha, S. A., Oshima, K., Hodder, P. S., and Heller, S., High-throughput screen for agonists of TRPML3.

9. Curriculum Vitae

Curriculum vitae is not part of the online version due to data protection guidelines.